Fabrication and characterization of optical microcavities functionalized by rare-earth oxide nanocrystals : realization of a single-mode ultra low threshold laser

Guoping Lin

Guoping Lin. Fabrication and characterization of optical microcavities functionalized by rare-earth oxide nanocrystals : realization of a single-mode ultra low threshold laser. Atomic Physics [physics.atom-ph]. Ecole Normale Supérieure de Paris - ENS Paris; Xiamen University, 2010. English. NNT : . tel-00517544v1

HAL Id: tel-00517544
https://theses.hal.science/tel-00517544v1

Submitted on 14 Sep 2010 (v1), last revised 10 Sep 2014 (v2)

THESE DE DOCTORAT

Spécialité : Physique

École doctorale : Physique de la région parisienne

réalisée en cotutelle entre

le Laboratoire Kastler Brossel, ENS

et Department of Physics, Xiamen University

présentée par

Guoping LIN

pour obtenir le grade de :

DOCTEUR DE L'ÉCOLE NORMALE SUPÉRIEURE

et

PhD OF XIAMEN UNIVERSITY

Sujet de la thèse :

Fabrication and characterization of optical microcavities functionalized by rare-earth oxide nanocrystals: realization of a single-mode ultra-low threshold laser

soutenue le 08 septembre 2010

devant le jury composé de :

M.	Hervé RIGNEAULT	Rapporteur
M.	Chenchun YE	Rapporteur
M.	Claude DELALANDE	Président du jury
M$^{\mathrm{me}}$	Huiying XU	Examinatrice
M.	Jean HARE	Directeur de thèse
M.	Zhiping CAI	Directeur de thèse
M$^{\mathrm{me}}$	Valérie LEFÈVRE-SEGUIN	Invitée

Contents

Acknowledgements

This work has been performed in the Optics of Nanoobjects team at Laboratoire Kastler Brossel, Physics department of École Normale Supérieure during my joint PhD period (2008-2010) under supervision of Jean Hare.

First, and most of all, I would like to send my sincere thanks to my supervisor, Jean HARE, who accepted me and provided me this subject. I also appreciate a lot for his help, kind suggestions and supervision during my work. His enthusiasm for physics and his kindness, patience inspired me very much. It is the first time I feel my interest and thirst in the knowledge ocean of physics. Under his patient and smart guidance, I am able to build my the theoretical frame and the hand-on skill on this project. I really enjoy every moment I spent in this work under his supervision.

I would like to thank Valérie lefèvre-seguin for her help on my work. In every group meeting, she has always provided nice suggestions. I also thank Michel Gross for his kind suggestions.

I want to thank the director of Laboratoire Kastler Brossel, Paul Indelicato and the director of Ecole Doctorale de Physique de la Région Parisienne, Roland Combescot for their receptions.

I thank my other supervisor Zhiping Cai for accepting me as a PhD student in Xiamen University in 2006 and for his agreement on this joint PhD project in 2008.

I appreciate very much for the defense committee members for taking the time to read the thesis and for their useful comments. I would like to express my special thanks to Claude Delalande for his acceptance to be the president of the jury. I thank a lot the rapporteurs Hervé Rigneault and Chenchun Ye for carefully reading my thesis and giving helpful comments. I also thank Huiying Xu for accepting to be a committee member for my defense.

I strongly acknowledge Olivier Tillement and his coworkers Pascal Perriat, Matteo Martini and François Lux for their general supply of nanoemitters and the

discussion with them. I also thank a lot Jean-Baptiste JAGER for his supply of silica microdisks for the microtoroid experiments and his kind help on carrying out SEM measurements.

I appreciate my college Yves CANDELA for discussions and help on this work, and Fadwa JOUD and Frédéric VERPILLAT for their help during this period. I also want to thank Yong CHEN, Damien BAIGL and Jie HU for their help on a SEM graph.

I also want to thank everyone who helps me during my work in LKB.

Finally, I want to express my thanks to my family for their support.

Introduction

It has been 50 years since the first laser was built by Theodore Maiman [1]. The invention of laser has revolutionized the whole world not only in research and industry but also in medicine and everyday life. The two key components of a laser, cavity and gain medium, have known countless metamorphosis since these early days, and this thesis will emphasize the interest of a new combination: silica microcavities and rare-earth nanocrystals.

While most laser cavities are still rather bulky, they have been brought into millimeter scale with the invention of the first laser diode [2] and were rapidly extended to the micrometer scale. On a practical point of view the compact size of a microcavity has benefited miniature devices, such as CD/DVD/BD storage devices in our daily life and integrated optics for telecommunications. Because the present work is aimed at low-threshold laser effect, let us recall that the probability of spontaneous and stimulated emission in a given mode of the microcavity is inversely proportional to the mode volume, and the decay time of the field is inversely proportional to the Q-factor [3]. Because the threshold is characterized by a balance between these two effects in the rate equations, the threshold is expected to scale as V/Q, that should be minimized. Furthermore, for a single-mode laser experiment, according to the Shawlow-Townes model, a higher Q-factor is favourable to achieve the narrowest spectral linewidth [4].

According to the light confinement method, there are three main kinds of microcavities: Fabry-Perot[1], photonics crystals and whispering gallery mode microcavities. Among them, the whispering gallery mode microcavities feature the highest Q-factors, and have attracted a lot of interest in the past two decades. My work in the present thesis is based on this kind of microcavities and more precisely on conventional microspheres and microtoroids. The term "whispering gallery" comes

---

[1] This first kind includes various F-P-like cavities using two reflecting mirrors, such as planar cavities, conventional laser diodes, micropillars or VCSELs

from an unusual acoustic property of the dome of Cathedral of Saint Paul in London, where a whisper at one side can be clearly heard at any place along the gallery. Lord Rayleigh, almost a century ago [5, 6], was the first to provide an interpretation of this phenomenon, based on the guiding properties of the gallery walls, thanks to successive lossless reflections of the sound.

In analogy with sound, electromagnetic waves can also travel along a spherical (or more generally cylindrically symmetric) interface by successive total internal reflections. When light comes back with the same phase after one round trip, a resonance is formed, giving rise to a stationary light distribution that is named as a whispering gallery mode (WGM). The theoretical studies on WGMs were carried out on spherical particles, independently by several physicists including Ludvig Lorenz [7], Gustav Mie [8] and Debye [9] in the late 19th century and early 20th century. The name of Mie remains attached to this resonances because Gustav Mie applied his calculation to explain the colors of colloidal suspension, and also because of micron sized spheres, the departure of isotropic Rayleigh scattering gives rise to a size dependant preferential forward scattering which is characteristic of the Mie regime of scattering, associated with low Q-resonances. In these mathematical solutions the angular momentum ℓ of the field in the sphere appears as an interference order, related to the number of wavelength fitting in the sphere circumference.

Whispering-gallery-mode lasers have been demonstrated from the early days of lasers by Garrett *et al* [10] using a Sm:CaF_2 sphere with a diameter in the millimeter range. However most of the later studies on lasing or non-linear optical effects in WGM were performed on liquid microdroplets, like the work on laser levitated droplets by A. Ashkin and J. M. Dziedzic in 1981 [11], or the Rhodamine doped ethanol droplets for which laser operation was achieved in 1984 [12]. The liquid droplets are easy to produce and to dope, and very small size can be obtained, allowing to achieve strong nonlinear effects. However they suffer from moderate quality factors (up to 10^5) and very short life time, limited by both evaporation and time of flight, making them not suitable for practical applications.

The surface tension induced solid WGM silica microspheres were first introduced by V. B. Braginsky and coworkers [13] and have given rise to an intense activity since this time. The ultra smooth surface, good spherical geometry and very low loss of pure silica lead to ultra-high Q-factor, which was measured to be as high as 10^{10} in the infrared for a silica microsphere [13, 14]. The resulting long light storage time gives very high circulating power in the cavity. Thus these cavities can be used to strongly reduce the threshold values of laser and nonlinear optics effects. In 1996, a threshold value as low as 200 nW was recorded in our group from a neodymium doped silica microsphere laser [15]. In 2003, on-chip toroidal WGM microcavities were first introduced by Armani *et al.* [16]. These toroidal microcavities combine the ever more accurate and reproducible silicon microfabrication technology and surface tension induced geometry and smoothness. In comparison with microspheres, they possess similar Q-factors (10^8) but smaller mode volumes, and permit a better control of their size. For some applications, they have superseded the microspheres, in spite of a more elaborate fabrication process.

The question of light coupling into or out from the WGM is critical, because, except for very small droplets, direct excitation by a free propagating beam is not possible. This is a necessary consequence of the high quality factor : very low losses require very low coupling to the outside. This is related to the evanescent wave surrounding the sphere (or the toroid), which is a corollary of total internal reflection. More precisely, in a geometrical optics point of view, Snell-Descartes laws prevent the possibility to launch a ray from the outside that fulfil the condition of total internal reflection in the cavity. The solution of this dilemma lies in "optical tunneling" or, in classical words, evanescent coupling. The most straightforward way to achieve this is known as the "prism coupling technique", that is a natural extension of the technique used to launch light in the guided modes of a planar waveguide [17]. This approach has been widely used in the early studies on WGM [13, 18, 19]. When it is carefully optimized, this technique can achieve rather good coupling efficiency up to 80% [20], but this requires difficult beam shaping, and it has a bulky size. Alternative techniques are based on optical waveguide structures, such as silica or polymer planar waveguides [21, 22], side-polished fiber blocks [23, 24, 25], angle polished fibers [26] which all have significant drawbacks. Presently the most popular technique is the fiber taper method that was first demonstrated by J.C. Knight and coworkers [27] and more accurately analyzed by K.J. Vahala and coworkers [28, 29]. This technique allows to engineer the mode matching and the phase matching of the two coupled evanescent fields, ensuring a good efficiency, which can reach a value as high as 99.99% [29]. Compared with prism couplers, fiber taper couplers have several advantages: their high coupling efficiency, extremely low losses and their flexibility for light excitation. On the extraction side, for active microcavities, they suffer from the phase matching condition which in general cannot be simultaneously achieved for the pump and the emitted signal. Notice that this problem does not affect prism coupling where output phase matching is automatically ensured by a slight angle change.

In recent years an increasing interest has been focused on nanoparticles, often called “nanocrystals” or quantum dots, which behave as very good solid state nanoemitters. The semiconductor quantum dots take advantage of the 3D confinement and of the quantization energy of electron and holes to exhibit discrete levels, like “artificial atoms”. Their nanometer size combined with a high fluorescence quantum yield make them very attractive for biolabelling, which drives most of their development. However their good optical properties make them really attractive to functionalize our microcavities, provided we can attach or integrate them in the microtoroids or microspheres, a task which is not necessarily easy [30, 19]. As compared to the last cited work, carried out in our group ten years ago, where the high quality factor was dramatically spoiled by a bulky sample, nanoparticles that can be embedded in the cavity have an obvious advantage. Moreover, since the scattering induced losses are proportional to the 6th power of their size, it should be possible to keep a good Q-factor up to a quite high concentration. Up to now, three techniques have been used to functionalize the microcavities: in early experiments, the whole microspheres were filled with active media like neodymium doped silica [15], erbium doped ZBLAN glass [31] and erbium:ytterbium-codoped phosphate glass [28]; more recently, for microtoroids, ion implantation has been used, permitting a better control of the ions position and thickness [32, 33, 34]; in 2003, Yang *et al.* functionalized a silica microsphere by dip-coating erbium-doped sol-gel to its surface [35]. With such a technique, one functionalizes the microcavity with a gain layer coating, which allows to maximize the coupling with the most confined WGMs, travelling within 1 μm to the surface.

Recently, gadolinium oxide nanocrystals have been successfully produced by Bazzi *et al.* [36]. The lanthanide oxide permits to substitute a significant part of the gadolinium by another, optically active, rare-earth, like neodymium, erbium, ytterbium, *etc.* As a host matrix, the gadolinium oxide is known to possess lower phonon energy, and thus is supposed to have lower non-radiative losses than silica [37], and possibly a smaller homogeneous broadening. Furthermore, if the crystalline order of the nanoparticles is preserved in spite of their very small size (a few nanometers), one can hope a significant reduction of the inhomogeneous broadening which in amorphous silica is mostly due to the randomness of the Stark-shift. Finally, since gadolinium oxide has a melting point as high as 2420°C, much higher than that of silica which is about 1600°C, one expects that they can be buried just below the surface of silica microspheres by high temperature annealing around the silica melting point. This process can also help to remove unwanted components during the dip-coating process and to reshape the cavity geometry, resulting in the preservation of ultra-high-Q factors. stable colloidal suspensions of

In the present work, we study silica microspheres functionalized by using a colloidal supension of neodymium-doped gadolinium oxide nanocrystals, which has been kindly provided by Olivier Tillement and coworkers in LPCML, Univ. Claude Bernard, Lyon. These nanocrystals are embedded close to the surface by dip-coating and gentle remelting of the cavities.

I have developed a new method to locate small mode volume WGMs, which is used to optimize the pumping conditions of the embedded nanocrystals. I have also developed another method to make a real time measurement and optimization of the microlaser characteristics. I have improved the microsphere preparation technique to reproducibly obtain very good microspheres with a diameter smaller than the usual technical limit of $40 - 50$ μm. Combining these original approaches, multimode lasing with a threshold of only 40 nW absorbed power has been obtained. Next, I have obtained single-mode lasing with a threshold as low as 65 nW for a microsphere diameter of 41 μm. These sub-microwatt threshold microlasers can be easily reproduced and their Q-factor at lasing wavelength is above 100 million. Some of these results have been extended to microtoroids, that I fabricated from a microdisk sample provided by Jean-Baptiste Jager from the SINAPS group in SP2M at CEA-Grenoble. In addition, a Yb^{3+}:$\mathrm{Gd_2O_3}$ NCs based microsphere laser and a neodymium implanted on-chip microtoroid laser are also demonstrated.

To organize this thesis, I have chosen to combine in each chapter the needed theory, followed by the experimental realization. It is divided into five chapters, the content of which is outlined in the following.

In Chapter 1, I give an overview on the analytical solutions to whispering gallery modes in spherical cavities. Then I briefly discuss the important parameters (Q factor, mode volume, resonance position, FSR). The optical properties of microtoroids are also investigated by employing finite element method numerical simulations. Finally, I present the experimental techniques used to fabricate silica microspheres and on-chip microtoroids.

In Chapter 2, I first describe the experimental method used to fabricate subwavelength fiber tapers. Then I present a model of evanescent excitation, based on a modified Fabry-Perot theory, that helps to understand the coupling mechanism of fiber-microcavity system. In the next section, I use it to explain the gap effect observed on the fiber taper coupled microsphere experiment. After this, I present the new mapping method using fiber taper. This presentation relies on the investigation of the WGM field distributions of a microsphere in polar direction, leading to location of small mode volume WGMs. I finally show how this method is extended to on-chip microtoroids.

The beginning of chapter 3 summarizes the main features of thermal bistability. This analysis allows me to investigate in detail the thermal bistability of a fiber coupled microsphere system. Then, I describe my experimental setup for microlaser measurement, and I explain the new method of real time laser characterization, that uses the thermal effect.

Chapter 4 starts with a brief description of the nanocrystal production, followed by the presentation of my coating procedure. Some results, provided by our colleagues of LPCML, on the microstructural properties of the functionalized microspheres, are then presented. Then I show the WGM photoluminescence properties of a functionalized silica microsphere. Finally, the sub-microwatt threshold laser performance of the active microspheres is demonstrated, in both multimode and single-mode conditions.

In Chapter 5, I present the laser performance of a Yb^{3+}:Gd_2O_3 NCs functionalized silica microsphere pumped around 800 nm. In addition, I explain the fabrication of a “rolled-down” neodymium ion implanted microtoroid, and I also investigate its laser performance.

Chapter 1

Whispering gallery mode microcavities

The so called whispering gallery can be traced back to the late 19th century. It was qualitatively introduced by Lord Rayleigh, who studied propagation of sound waves in Saint Paul's Cathedral in London [5, 6]. The smooth surface of the wall enables sound to travel a long time, so that one person can hear another person whispering at the opposite side of the cathedral dome which is about 30 m far. The same phenomenon also occurs in electromagnetic field, where the theory on whispering gallery modes (WGMs) was provided by Gustav Mie and Ludvig Lorenz, also called Lorenz-Mie theory. It is therefore widely used in the study of spherical microcavities.

In this chapter, an overview of WGM theories in both spherical microcavities and toroidal microcavities is first given, including the quality factors, free spectral range, mode volumes and resonance positions. Then the detail information on the fabrication of ultra-high Q silica microspheres and on-chip silica microtoroids in our studies is also given.

1.1 General properties of WGMs

1.1.1 A simple approach for WGMs

First of all, we will introduce a simple approach to the WGMs. For an perfect microsphere, the problem can be explored by employing geometric optics on its cross section because the incident plane is conserved. Considering a sphere with a radius a and refractive index N surrounded by air as shown in figure 1.1 (a), when light is incident at the interface with an angle i larger than i_c, where $i_c = \arcsin(1/N)$ is the critical angle, the ray is then totally reflected. Due to the circular symmetric, it therefore keeps the same incident angle for the following reflections. As a result, the light ray is trapped inside the cavity by successive total internal reflections.

If the travel distance in one round trip is integral multiple of the wavelength, the WGM resonance mode will be formed. For large circle where $a \gg \lambda$ and incident angle $i \approx \pi/2$, the ray travels very close to the circle interface. Thus an approximate condition for a WGM resonance can be expressed as:

$$2\pi a = \frac{\lambda}{N}\ell. \tag{1.1}$$

where ℓ is a interference order and λ is the wavelength in vacuum. The resonance condition for frequency is:

$$\nu = \frac{\ell c}{2\pi N a}. \tag{1.2}$$

where c is the speed of light in vacuum. The free spectral range(FSR) can then be written as:

$$\Delta\nu_{\mathrm{FSR}} = \frac{\Delta\nu}{\Delta\ell} \simeq \frac{d\nu}{d\ell} = \frac{c}{2\pi N a}. \tag{1.3}$$

$$\Delta\lambda_{\mathrm{FSR}} = \frac{\Delta\lambda}{\Delta\ell} \simeq \frac{d\lambda}{d\ell} = \frac{\lambda^2}{2\pi N a}. \tag{1.4}$$

For the cavity with $N = 1.45$ (fused silica refractive index) and radius $a = 20$ µm, its FSR is $\Delta\nu_{\mathrm{FSR}} \sim 1.6$ THz in frequency or $\Delta\lambda_{\mathrm{FSR}} \sim 3.5$ nm at $\lambda = 800$ nm. It should be mentioned that this approach works for the case where the cavity is much larger than the operation wavelength (ℓ is large).

On the other hand, we also introduce the angular momentum $\mathbf{L}$ as shown in figure 1.1 (b), which is defined as follows:

$$\mathbf{L} = \mathbf{r} \times \mathbf{k} \tag{1.5}$$

In the case of the WGM resonance shown in figure 1.1 (a), its angular momentum can be easily derived:

$$L = r_1 k = r_1 N k_0 \tag{1.6}$$

where k_0 is the wave number in vacuum and $r_1 = a \sin i$. In the condition where $\sin i \simeq 1$, $L \simeq N k_0 a = \ell$. So the interference order ℓ is often called angular order. It is well known that the total internal reflection produces a fraction of energy in the form of an evanescent wave across the boundary surface. Therefore, one gets:

$$L = r_2 k_0 = r_1 N k_0 \tag{1.7}$$

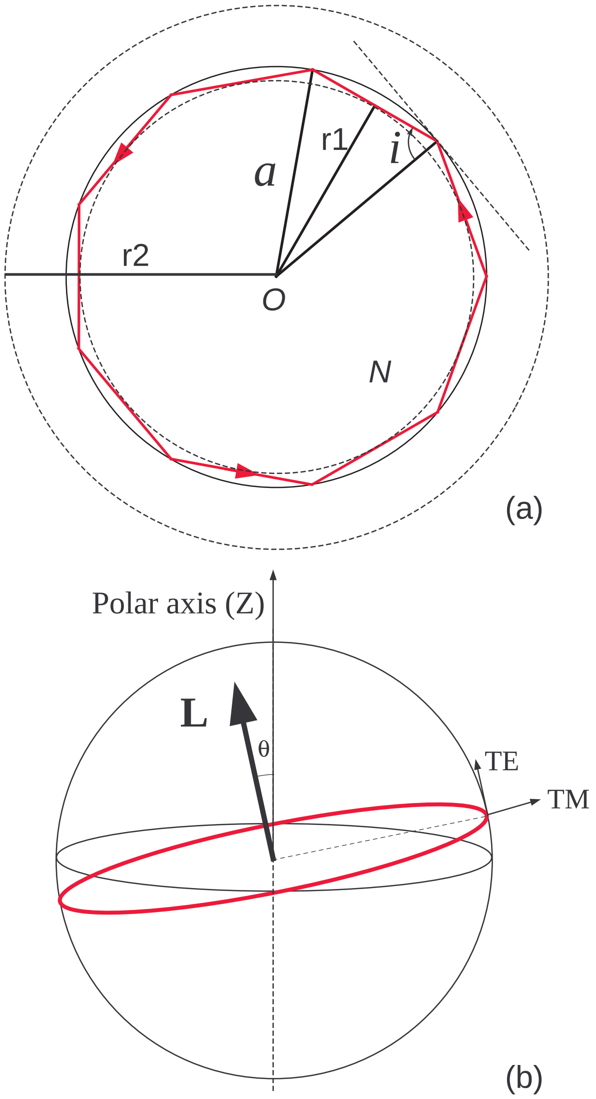

Figure 1.1: (a) Sketch of the cross section plane of a sphere where light ray is traveling by total internal reflections. The a, O, N and i represent the radius, center, refractive index of the cavity and incident angle of the light ray respectively. (b) Sketch of a WGM in a perfect microsphere. TE, TM denote its polarizations and **L** its angular momentum.

which demonstrates the confinement of a WGM in the range of r_1 and r_2. It should be noted that total internal reflection in a WGM can not be really total due to the curvature of the interface between the cavity and its surrounding. In comparison with the light path inside the sphere, the portion of evanescent field outside has a longer light path length, which means that it needs to "go faster" than the speed of light inside the cavity to stay with the main field. As a result, in the case of $r > r_2$ it radiates out and causes losses. This will also be presented in section 1.1.2.4.

1.1.2 WGMs theory in microspheres

1.1.2.1 Solution of electromagnetic field

To gain a better understanding of WGMs in a microsphere, the solution of electromagnetic field in a single homogeneous sphere is presented. A WGM can be characterized by its polarization (TE or TM) and three integer orders (n,ℓ,m), where n denotes the radial order, ℓ the angular mode number and m the azimuthal mode number. The mode number n is the number of maxima in the radial distribution of the internal electric field, the mode number ℓ corresponds to the number of wavelengths around the circumference, and the mode number m (in the range of $-\ell \leq m \leq \ell$) gives $(\ell - m + 1)$ maxima in the polar distribution of internal electric field. In order to explore the optical properties in a homogenous microsphere, the solution of Maxwell equations is given. Consider a dielectric microsphere in the air, the refractive index can be described as:

$$N(r) = \begin{cases} N & \text{if} \quad r < a \\ 1 & \text{if} \quad r > a. \end{cases} \tag{1.8}$$

So the Maxwell equations for electric field[1] can be written as:

$$\begin{cases} \boldsymbol{\nabla} \times (\boldsymbol{\nabla} \times \mathbf{E}) - N^2(r)\, k_0^2\, \mathbf{E} = 0 \\ \boldsymbol{\nabla} . \, \mathbf{E} = 0, \end{cases} \tag{1.9}$$

where $k_0 = \dfrac{2\pi}{\lambda_0}$, then the corresponding vector Helmholtz's equation is given:

$$\boldsymbol{\Delta} \mathbf{E} + N^2(r)\, k_0^2\, \mathbf{E} = 0. \tag{1.10}$$

---

[1] The same equations for magnetic field

The exact solution of this function can thus be derived:

$$
\begin{aligned}
&\textbf{M}\text{odes TE}\begin{cases} \mathbf{E}^{TE}_{\ell m}(\mathbf{r}) = E_0\dfrac{f_\ell(r)}{k_0 r}\mathbf{X}^m_\ell(\Omega) \\ \mathbf{B}^{TE}_{\ell m}(\mathbf{r}) = -\dfrac{iE_0}{c}\left(\dfrac{f'_\ell(r)}{{k_0}^2 r}\mathbf{Y}^m_\ell(\Omega) + \sqrt{\ell(\ell+1)}\dfrac{f_\ell(r)}{{k_0}^2 r^2}\mathbf{Z}^m_\ell(\Omega)\right) \end{cases} \\
&\textbf{M}\text{odes TM}\begin{cases} \mathbf{E}^{TM}_{\ell m}(\mathbf{r}) = \dfrac{E_0}{N^2}\left(\dfrac{f'_\ell(r)}{{k_0}^2 r}\mathbf{Y}^m_\ell(\Omega) + \sqrt{\ell(\ell+1)}\dfrac{f_\ell(r)}{{k_0}^2 r^2}\mathbf{Z}^m_\ell(\Omega)\right) \\ \mathbf{B}^{TM}_{\ell m}(\mathbf{r}) = -\dfrac{iE_0}{c}\dfrac{f_\ell(r)}{k_0 r}\mathbf{X}^m_\ell(\Omega) \end{cases}
\end{aligned}
\tag{1.11}
$$

with three vector spherical harmonics:

$$
\begin{cases} \mathbf{X}^m_\ell = \dfrac{1}{\sqrt{\ell(\ell+1)}}\boldsymbol{\nabla} Y^m_\ell \times \mathbf{r} \\ \mathbf{Y}^m_\ell = \dfrac{1}{\sqrt{\ell(\ell+1)}}\, r\,\boldsymbol{\nabla} Y^m_\ell \\ \mathbf{Z}^m_\ell = Y^m_\ell\,\hat{\mathbf{r}}. \end{cases}
\tag{1.12}
$$

From equation (1.11) and (1.12), the direction of electric field in both TE and TM polarization can be illustrated as shown in Figure 1.1. In equation (1.11), $f(r)$ is the radial distribution for the electric field, which can be determined from the following equation:

$$
f''(r) - (\ell(\ell+1)/r^2)f(r) + N^2(r)k_0^2(r)f(r) = 0.
\tag{1.13}
$$

The solution to this differential equation can be determined by:

$$
\begin{cases} \psi_\ell(Nk_0 r) & \text{for} \quad r < a \\ \alpha\psi_\ell(k_0 r) + \beta\chi_\ell(k_0 r) & \text{for} \quad r > a, \end{cases}
\tag{1.14}
$$

where α and β are constants determined by the conditions at $r = a$ and $r \to \infty$, and ψ_ℓ, χ_ℓ are Riccati-Bessel function of the first kind and second kind respectively, defined by:

$$
\begin{cases} \psi_\ell(\rho) = \rho\, j_\ell(\rho) \\ \chi_\ell(\rho) = \rho\, n_\ell(\rho), \end{cases}
\tag{1.15}
$$

with j_ℓ and n_ℓ Bessel function of the first kind and second kind (Neumann function). The complete solution is rather complicated. In the case of the interesting modes, where $\ell \gg 1$, the solution can be simplified by proper approximation [38]:

$$\begin{aligned}
&\mathbf{M}\text{odes TE}\left\{\begin{array}{l}
\mathbf{E}_{\ell m}^{TE}(\mathbf{r}) \approx \dfrac{f(r)}{k_0 r} Y_\ell^m(\theta,\phi)\,\mathbf{u}_\theta, \\
\mathbf{B}_{\ell m}^{TE}(\mathbf{r}) \approx \dfrac{f(r)}{k_0^2 r^2} Y_\ell^m(\theta,\phi)\,\mathbf{u}_r
\end{array}\right. \\
&\mathbf{M}\text{odes TM}\left\{\begin{array}{l}
\mathbf{E}_{\ell m}^{TM}(\mathbf{r}) \approx \dfrac{f(r)}{k_0^2 r^2} Y_\ell^m(\theta,\phi)\,\mathbf{u}_r. \\
\mathbf{B}_{\ell m}^{TM}(\mathbf{r}) \approx \dfrac{f(r)}{k_0 r} Y_\ell^m(\theta,\phi)\,\mathbf{u}_\theta.
\end{array}\right.
\end{aligned} \tag{1.16}$$

where $\mathbf{u}_r$ and $\mathbf{u}_\theta$ are the unit vectors in spherical coordinate system.

1.1.2.2 Resonance positions and spacing

Here a brief review on the analytic approximation of resonance positions equation is given. In equation (1.14), the function $f(r)$ and its derivative $f'(r)$ must be continuous across the microsphere and air interface ($a = 0$):

$$\begin{aligned}
&\text{Modes TE}\left\{\begin{array}{c}
\psi_\ell(Nk_0a) = \alpha\psi_\ell(k_0a) + \beta\chi_\ell(k_0a) \\
N\psi'_\ell(Nk_0a) = \alpha\psi'_\ell(k_0a) + \beta\chi'_\ell(k_0a)
\end{array}\right. \\
&\text{Modes TM}\left\{\begin{array}{c}
N^{-1}\psi'_\ell(Nk_0a) = \alpha\psi'_\ell(k_0a) + \beta\chi'_\ell(k_0a) \\
\psi_\ell(Nk_0a) = \alpha\psi_\ell(k_0a) + \beta\chi_\ell(k_0a).
\end{array}\right.
\end{aligned} \tag{1.17}$$

using the Wronskian function of ψ_ℓ and χ_ℓ, equation (1.17) can be written as:

$$\begin{aligned}
\alpha &= \psi_\ell(Nx)\chi'_\ell(x) - P\psi'_\ell(Nx)\chi_\ell(x) \\
\beta &= -\left(\psi_\ell(Nx)\psi'_\ell(x) - P\psi'_\ell(Nx)\psi_\ell(x_0)\right).
\end{aligned} \tag{1.18}$$

where the size parameter x is defined as $x = k_0a$, and P represent the polarization modes (N for TE, 1/N for TM respectively). On the other hand, because the function ψ_ℓ increases exponentially with r, given $r \to \infty$ the constant α should thus be determined to be 0. Therefore, by considering $\alpha = 0$ in the continuity equation (1.18) the resonant condition is derived:

$$P\frac{\psi'_\ell(Nx)}{\psi_\ell(Nx)} = \frac{\chi'_\ell(x)}{\chi_\ell(x)} \quad \text{where} \quad P = \left\{\begin{array}{ll} N & \text{for TE mode} \\ 1/N & \text{for TM mode.}\end{array}\right. \tag{1.19}$$

The resonance position can be given by solving equation (1.19). When considering a large sphere where the angular mode number $\ell \gg 1$, there are mainly two analytic approximations based on $(\ell + 1/2)^{1/3}$. One of the most explicit expression using the first term of expansion results in [39]:

$$Nx_{n\ell} = \ell + \frac{1}{2} + \left(\frac{\ell + \frac{1}{2}}{2}\right)^{1/3}(-z_n) - \frac{P}{\sqrt{N^2 - 1}} + \ldots \tag{1.20}$$

where z_n is the n_{th} zero of the Airy function. It should be noted that this equation gives inaccurate resonant positions for large n values that also depend on ℓ. From equation (1.20), it's clear that the resonance position depends on the radial mode number n, angular number ℓ and polarization condition. However, this equation is independent on the azimuthal mode number m, which means that the polar modes in a perfect sphere cavity are degenerate. Another way to get the resonance position by using eikonal approximation, which was developed in 1997 [38] is as follows:

$$Nx_{n\ell} \simeq \ell + \frac{1}{2} + \left(\frac{\ell+\frac{1}{2}}{2}\right)^{1/3} \left[\frac{3\pi}{2}(n-\frac{1}{4})\right]^{2/3} - \frac{P}{\sqrt{N^2-1}} + ... \tag{1.21}$$

The only difference between two equations is zero of the Airy function and $(\frac{3\pi}{2}(n-\frac{1}{4}))^{2/3}$:

From Table 1.1, one can see very good agreement between these two coefficients. As previously mentioned, the two approximations are inaccurate for large radial mode numbers. However this is not the problem, since that the most interesting WGMs are the fundamental radial modes ($n = 1$) which obviously possess smallest mode volumes.

n	1	2	3	4	5	6	7
$-z_n$	2.338	4.088	5.521	6.787	7.944	9.023	10.040
$(\frac{3\pi}{2}(n-\frac{1}{4}))^{2/3}$	2.320	4.082	5.517	6.784	7.942	9.021	10.039

Table 1.1: Comparison of the zero of Airy function and with an approximation based on eikonal approach

Spacing:

- **FSR**: For a traditional Fabry-Perot cavity, the free spectral range (FSR) is defined as the frequency or wavelength separation between longitudinal modes. However, the resonance modes in a microsphere are much more complicated. In order to simplify the problem, one can treat the angular mode spacing in a microsphere cavity as the FSR. For large l, $\Delta x/\Delta\ell \simeq 1/N$. The FSR can be written as:

  $$\text{FSR} = \frac{\Delta\nu}{\Delta\ell} = \frac{c}{2\pi Na} \tag{1.22}$$

  It can also be derived by considering that the circumference of a microsphere corresponds to the round trip length of a ring FP.

- **Polarization** $\Delta\nu^{\text{TE-TM}}$: From the solution of optical fields in a microsphere, one can see that WGMs also depend on the mode polarization denoted as P in equation (1.21). The spacing between the polarization (TE and TM) modes with the same n, ℓ and m is given as follows:

  $$\Delta\nu^{\text{TE-TM}} = \Delta(Nx)\frac{c}{2\pi Na} \approx \frac{\sqrt{N^2-1}}{N}\frac{c}{2\pi Na} \tag{1.23}$$

  For a silica microsphere with $N = 1.45$, $\Delta\nu^{\text{TE-TM}} \approx 0.7 \times \text{FSR}$.

- **Radial order** $\Delta\nu^{\text{TE-TM}}$: The spacing for different radial order mode n can be obtained:

  $$\nu_{n+1,\ell} - \nu_{n\ell} \simeq \frac{c}{2\pi Na}\frac{\partial\nu_{n\ell}}{\partial n} \simeq \frac{c}{2\pi Na}(\ell+\frac{1}{2})^{1/3} \times \left(\frac{\pi^2}{3n}\right)^{1/3}. \tag{1.24}$$

  For $n = 1$ and $\ell = 500$, $\nu_{n+1,\ell} - \nu_{n\ell} \approx 10 \times \text{FSR}$.

1.1.2.3 Mode splitting due to small ellipticity

It is well known that the WGMs of different azimuthal orders m in a perfect microsphere are degenerate, as discussed in the former section. However, the silica microspheres fabricated in the experiment are never perfectly spherical symmetric but ellipses[2]. In order to characterize the distortion, the ellipticity is defined : $e = (a_p - a_e)/a$, where a_p and a_e are polar and equatorial respectively, as can be seen in Fig 1.2.

Obviously the presence of ellipticity breaks the degeneracy of polar modes, and leads to a frequency shift for the modes of same n, ℓ and different m order [40]. Considering the small ellipticity in present work (ranging from 0.1% to 2%) and small values of polar order $q = \ell - |m|$, the frequency shift can be written as follows:

$$\frac{\delta\nu_{\ell,m}}{\nu_{\ell,m}} = -\frac{e}{6}\left(1 - \frac{3\,m^2}{\ell(\ell+1)}\right) \approx e(\frac{1}{3} - \frac{q}{\ell})\ . \tag{1.25}$$

This gives a multiplet of nearly equally spaced modes for $|m| \approx \ell$ with an interval:

$$\Delta\nu = e\ \nu_{\ell,m}/\ell \approx e\,\text{FSR} \tag{1.26}$$

It moreover indicates that the fundamental polar mode $q = 0$ has the largest frequency of the multiplet for a prolate microsphere ($e > 0$) and smallest frequency

---

[2] In the following, the spherical microcavities are directly called "microspheres" for brevity

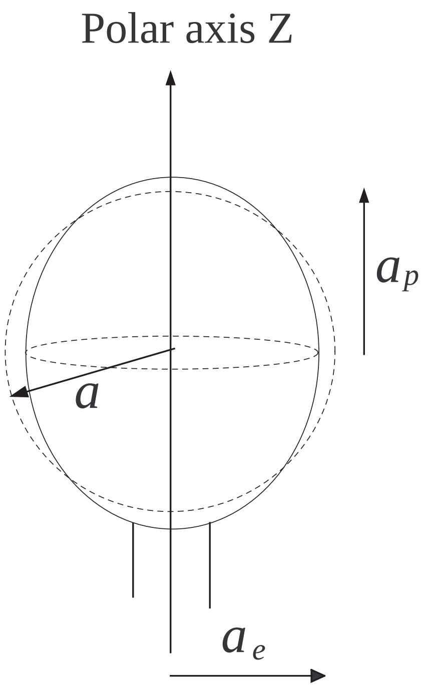

Figure 1.2: Illustration of the distortion of a perfect microsphere to an ellipse. The polar radius a_p and equatorial radius a_e are shown.

for a oblate microsphere ($e < 0$). For example, a prolate silica microsphere with ellipticity about 0.1% and diameter of 40 μm will have the fundamental polar mode in larger frequency. Figure 1.3 is an illustration of this splitting effect, without considering the polarization and radial order. Only few high order polar modes are shown. The detailed experimental investigation on it will be provided in the next chapter.

1.1.2.4 Optical field distribution

For better understanding the WGMs in a microsphere, angular and radial distributions of the intensity are presented.

Polar angle distribution

The angular field amplitude distribution is expressed by the spherical harmonic function $|Y_\ell^m(\theta, \phi)|^2$. For large ℓ value and moderate $q = \ell - |m|$, the intensity can

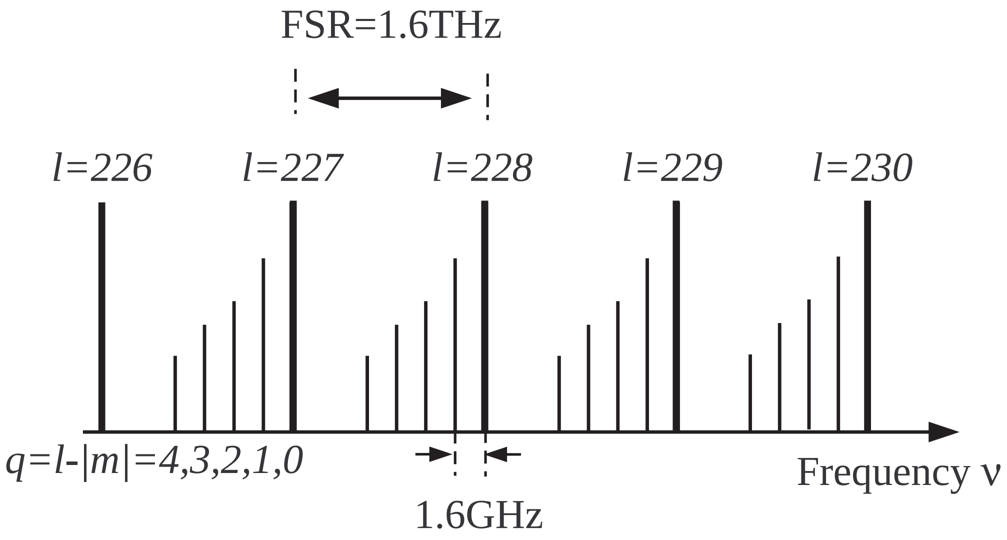

Figure 1.3: Illustration of resonance spectrum around 800 nm for $n = 1$ and $\ell - |m| = 0, 1, 2, 3, 4$ modes in a silica microsphere with diameter of 40 μm and 0.1% ellipticity.

be approximated as follows:

$$I_{\ell,q}(\theta,\phi) \propto \left|H_q(\sqrt{\ell}\cos\theta)\ \sin^{\ell-q}\theta\ \exp(i(\ell-q)\phi)\right|^2 \tag{1.27}$$

where $H_q(\sqrt{\ell}\cos\theta)$ represents a Hermite polynomial. θ is the polar angle. ϕ is the angular angle in equatorial plane. For given $\phi = 0$ and $\ell = 100$, the intensity distributions in polar angle direction for different q values are given in figure 1.4. It can be clearly observed that the q value denotes the $q + 1$ maxima or antinodes.

Radial distribution

In order to better understand the radial distribution of WGMs, we rewrite equation (1.13) as:

$$-f''(r) + \frac{\ell(\ell+1)}{r^2}f(r) + k_0^2(1 - N^2(r))f(r) = k_0^2 f(r). \tag{1.28}$$

which is similar to the Schrödinger equation for a single particle [41]. Thus, defining the "energy" $E = \hbar^2 k_0^2/2m$, the effective potential is given as follows:

$$V_{\text{eff}}(r) = \frac{\hbar^2}{2m}\left[k_0^2(1 - N^2(r)) + \frac{\ell(\ell+1)}{r^2}\right], \tag{1.29}$$

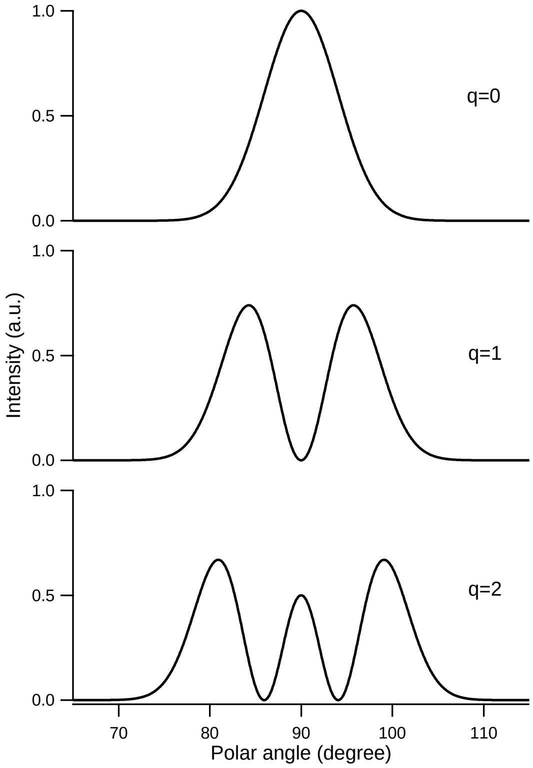

Figure 1.4: Intensity distribution in polar angle direction for $\ell = 100$ and $q = 0, 1, 2$.

where $N(r)$ is defined by equation (1.8). Actually, the effective potential is the sum of a square potential well due to index step and centrifugal potential [41]. For a given wave number k, the effective potential V_{eff} is illustrated in figure 1.5.

The r_1 and r_2 are the solution of equation $V_{\mathrm{eff}} = E$, and can be easily obtained:

$$\begin{cases} r_1 = \dfrac{\sqrt{\ell(\ell+1)}}{Nk_0} = \dfrac{a\sqrt{\ell(\ell+1)}}{Nx} \\ r_2 = Nr_1 \end{cases} \tag{1.30}$$

In figure 1.6, the radial field amplitude distributions of WGMs with $n = 1, 5, 7$ and $\ell = 100$ in a silica microsphere (N= 1.45) and the corresponding effective potentials are plotted together. The maxima of the internal field is determined by the radial order n. It can be seen that the WGMs are well confined inside the cavity in the range of $r_1 < r < a$, with a small fraction outside the cavity in the evanescent form. In this figure, the propagation behavior of the field for $r > r_2$ leads to radiation losses. The most confined modes of $n = 1$ and $q = 0$ are so called

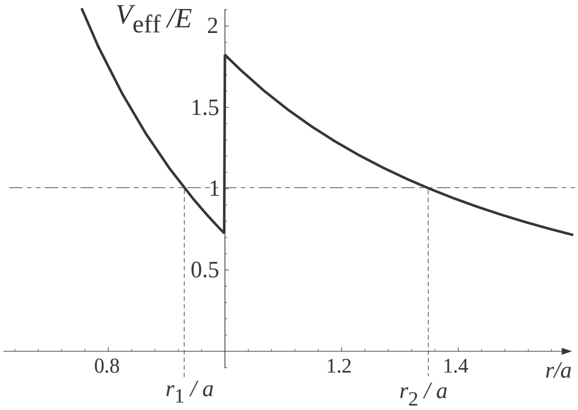

Figure 1.5: Effective potential for a given k in a microsphere, the corresponding WGM is mostly confined between r_1 and r_2

fundamental modes, which are thus most interesting.

1.1.2.5 Quality factor

For any resonator, quality factor(Q factor) is one of the basic parameters that describes the ability of energy storing. Generally speaking, it is defined by the ratio of the energy stored in the cavity to the energy lost in one cycle:

$$Q = 2\pi \times \frac{\text{Energy stored in the cavity}}{\text{Energy loss per cycle}} \tag{1.31}$$

In practice, for optical cavities, the Q factor of a mode with resonant wavelength λ_0 or frequency ν_0 characterizes the linewidth $\delta\lambda$ of the resonance, or equivalently the cavity photon lifetime τ_{cav}:

$$Q = \frac{\nu_0}{\delta\nu} = \frac{\lambda_0}{\delta\lambda} = \omega_0\tau_{\text{cav}} = 2\pi\nu_0\tau_{cav} \tag{1.32}$$

Thus, the highest quality factor corresponds to the longest photon storage time and to the narrowest resonance linewidth. As compared with the other microcavity designs such as photonics crystal, Fabry-Perot, or micropilar microcavities, the important advantage of WGM microcavities is that they possess extremely high Q factors. This significant parameter allows the investigation of strong interaction between the photons and the medium in which it propagates. Besides, as the resonance linewidth is very narrow, a minute shift can be detected and mechanical [42], chemical [43] and biologic sensors [44, 45], taking advantage of this sensitivity have been proposed.

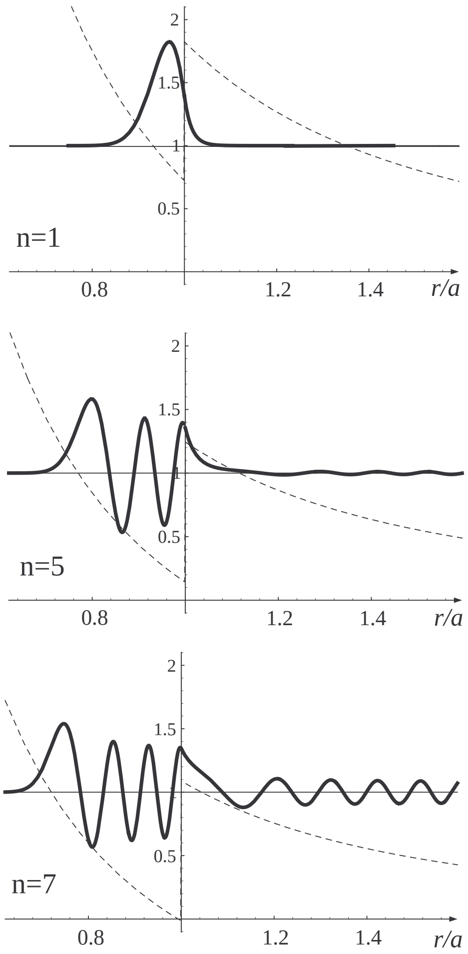

Figure 1.6: Field amplitude distributions for three n values and the corresponding effective potentials. The horizontal axis corresponds to r/a.

In the case of a bulk optical medium without nonlinear optical processes, the light absorption is given by the Lambert-Beer law $I(L) = I_0 e^{-\alpha L}$. Replacing the distance L by ct/N, this law is converted in a temporal relaxation with a characteristic time $\tau_{\text{cav}} = N/\alpha c$, so that the optical Q factor is given by

$$Q = 2\pi\nu_0\tau_{\text{cav}} = \frac{2\pi N}{\lambda_0 \alpha} \ . \tag{1.33}$$

When attenuation is only due to absorption, one can introduce the complex refractive index $N = N' + N''$,one has $\alpha = 2N'/N''k$ and $Q = N'/2N''$. More generally attenuation results from different kinds of losses, and the coefficient α writes:

$$\alpha = \underbrace{\alpha_{\text{mat}} + \alpha_{\text{rad}} + \alpha_{\text{surf}}}_{\alpha_{\text{mod}}} + \alpha_{coup} \tag{1.34}$$

where α_{mod} denotes homogeneously distributed loss coefficient of a given mode. The contribution α_{coup} resulting from external coupler is in fact localized in the coupling region, but, as long as it remains small, it can also be treated as distributed loss. It will be discussed in more details in Chapter 2, section 2.2.1. We focus here on the different parts of α_{mod}:

(i) α_{mat} denotes the absorption loss in cavity material, including internal scattering;

(ii) α_{rad} denotes the diffraction loss due to the curvature of the boundary, also know as radiation loss or diffraction loss;

(iii) α_{surf} denotes the scattering loss due to surface roughness.

Hence the total Q factor can be written as:

$$Q^{-1} = Q^{-1}_{\text{mod}} + Q^{-1}_{\text{coup}} = (Q^{-1}_{\text{rad}} + Q^{-1}_{\text{mat}} + Q^{-1}_{\text{surf}}) + Q^{-1}_{\text{coup}} \tag{1.35}$$

Diffraction loss

As previously described, the WGM relies on the total internal reflection mechanism. However, internal reflection can not be really total due to the presence of curved interface between cavity material and its surrounding. As mentioned in section 1.1.2.4, the evanescent field is established in the region where $a < r < r_2$. But in the case of $r > r_2$, the dispersion relation restores propagative behavior, that results in radiation losses. This gives a minimum radius for a sphere cavity to achieve ultra-high Q factor.

To investigate this phenomenon in more detail, the quality factor related to diffraction loss can be estimated using the Wentzel-Kramers-Brillouin approximation (WKB) [38]:

$$Q_{\text{rad}} \approx x \exp\left[2(\ell + \tfrac{1}{2})\; g\left(\frac{x}{\ell + \frac{1}{2}}\right)\right], \tag{1.36}$$

where $g(u) = -\sqrt{1-u^2} + \operatorname{argcosh}(1/u)$, is a decreasing positive function, and $x = 2\pi a/\lambda$ the size parameter (a is the sphere radius). The main result is that the Q factor drops down exponentially when decreasing the sphere diameter. In figure 1.7, the maximum Q factor as a function of the silica microsphere diameter is presented in Log-linear, when considering only diffraction loss, for the wavelengths around 800 nm. It can also be seen that WGMs of TE polarization possesses higher Q factor than those of TM polarization. This is due to the fact that TE polarization is more confined inside the cavity compared to TM polarization, as will be shown in section 1.1.2.6.

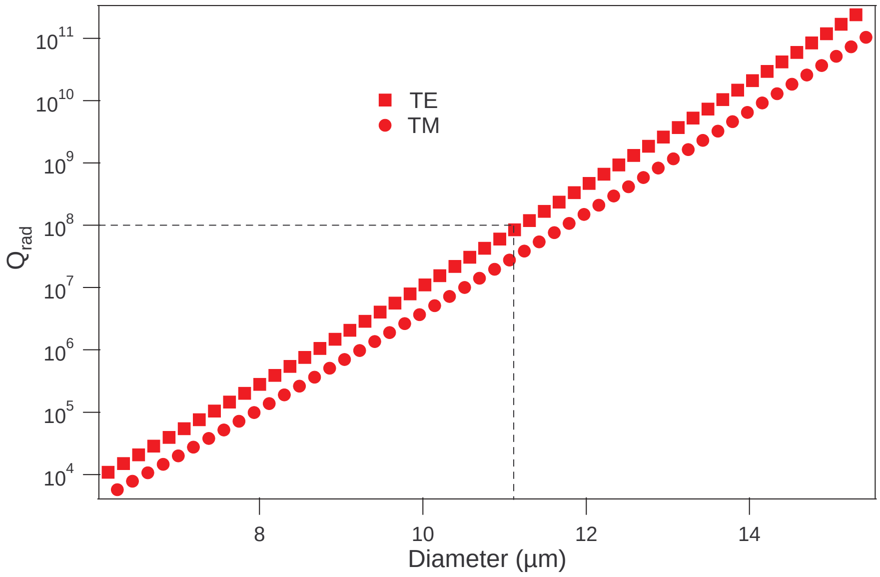

Figure 1.7: Log-linear plot of the Q factor of the fundamental mode, when it is limited by radiation loss only, as a function of sphere diameter at the wavelength of $\lambda \sim 800$ nm.

Considering only TE polarization, the minimum diameter of the sphere cavity to achieve 10^8 quality factor is about 11 µm for the wavelength of 800 nm (as shown by dotted line in figure 1.7). While for the wavelength of 1550 nm, this value would be 22 μm. Above this diameter, the Q factor is mainly limited by the other loss mechanisms, which will be discussed in the following part. In our laboratory, we observed 100 million Q factor for a silica microsphere with diameter as small as 17 μm.

As can be seen in equation (1.35), because $x/(\ell+\frac{1}{2})$ ranges from $\sim 1/N$ for the radial fundamental modes, to ~ 1 for the less bound modes, the Q factor is also strongly dependent on the radial order of the modes. For example, consider a silica microsphere with diameter of 50 μm, the calculated quality factor is $Q_{\text{diff}} \approx 10^{40}$ for mode $\ell = 280$ and $n = 1$, but $Q_{\text{diff}} \approx 10^8$ for $\ell = 215$ and $n = 10$. Clearly, the radiation loss is usually negligible, excepted for very small microspheres.

Material loss

The cavity material loss is another important effect restricting the value of intrinsic Q factor. Historically, fused microsphere cavities have been made of various low loss glass, such as fluoride glass (like ZBLAN) [31, 46], phosphate glass (P_2O_5) [28], tellurite glass (TeO_2) [47] and silica glass (SiO_2) [15]. Among all these materials, the silica glass has been the most widely studied, and used in fiber optics, due to its low intrinsic absorption loss for a wide range of wavelengths. In this work, silica single mode fibers are chosen for the fabrication of microsphere cavities. Generally speaking, the material losses in a silica fiber result mainly from the following contributions:

Absorption loss The presence of missing oxygen defects in the atomic structure can induce absorption, but the main cause of the material losses is the trace metal impurities, such as iron, nickel and chromium, that can be introduced during the fabrication and induce absorption in the blue part of the spectrum. In synthetic silica (obtained by oxidization of pure silicon) the amount of water and more generally of O–H bonds is a critical parameter because of its vibration band in the near infrared. Finally, the vibration of silicon-oxygen (Si-O) bonds on the long wavelength (above 2000 nm) and the tail of ultraviolet absorption due to electronic transitions result in the intrinsic absorption of silica.

Rayleigh scattering The Rayleigh scattering loss is due to the presence of small density fluctuation or defects that can not be avoided. However, not all the Rayleigh scattering inside a microsphere cavity will contribute to the loss. Indeed, Rayleigh scatter will also induce internal mode coupling and result in the splitting of $\pm m$ WGM modes [48]. Only the portion that irradiates out of the cavity contribute to the loss[49].

The material loss in a fiber is typically determined by measuring the attenuation. This parameter is expressed as $\alpha = 10\log(P_{\text{out}}/P_{\text{in}})/L$ dB/km, where P_{in} is the optical input power, P_{out} the optical output power and L the length of the fiber. As a result, the corresponding cavity lifetime in a microsphere can be derived as $\tau_{\text{mat}} = 10\,000/\alpha\ \log(e)/(c/N)$, and the Q factor limited by material loss writes:

$$Q_{\text{mat}} = 2\pi\nu_0\tau_{\text{mat}} \approx \frac{2\pi N}{\lambda}\frac{4.3\times10^3}{\alpha}\ . \tag{1.37}$$

In this work, the attenuation of a single mode fiber for the operation wavelength ($\lambda \sim 800$ nm) is about 2 dB $\cdot$ km^{-1}. For the wavelength of $\lambda = 800$ nm, the quality factor limited by material loss is thus $Q_{\text{mat}} = 2.5\times10^{10}$.

Surface losses

In order to estimate the loss due to scattering on the sphere surface, one uses the Rayleigh scattering approach for a dipole $d \approx (N\sigma\zeta^2)\,E$, where σ is characteristic surface roughness and ζ its correlation length. The maximum Q factor limited by surface scattering loss can then be expressed approximately using the following formula [50]:

$$Q_{\text{surf}} = \frac{3}{8\pi^2}\frac{\lambda^4}{\sigma^2\zeta^2}\ell^{1/3} \tag{1.38}$$

For example, considering a silica microsphere with diameter of 40 µm and an operation wavelength $\lambda \sim 800$ nm, the fundamental mode has $\ell \approx 2\pi Na/\lambda \approx 228$. If the roughness is such that $\sigma = 0.2$ nm and $\zeta = 5$ nm, then the corresponding quality factor limited by surface roughness is 1.6×10^{10}. Recent investigation of fused silica surface has shown that σ is rather small, typically less than 0.2 nm.

In fact, there is an another important surface loss mechanism: the optical losses induced by dust and water deposition. If the microsphere is put in a clean box under a normal working condition, the Q factor drops down to 10^7 in several hours, likely due to water adsorption [51]. It would be better in clean room condition. Certainly, the best condition is in vacuum or pure rare-gaz atmosphere, where the Q factor in a silica microsphere can be kept above 100 million for at least several months [38].

1.1.2.6 Mode volume

Mode volume is another critical parameter, which plays an important role in many application including Cavity quantum electrodynamics (CQED) in both weak and strong coupling region. Generally speaking in CQED, the mode volume of a WGM is defined as:

$$\mathcal{V} = \frac{\int w(\mathbf{r})\, d^3\mathbf{r}}{w_{\max}}, \tag{1.39}$$

where $w(\mathbf{r})$ is electromagnetic energy density:

$$w(\mathbf{r}) = \frac{1}{2}\left(\frac{\epsilon(\mathbf{r})}{2}\mathbf{E}(\mathbf{r}).\mathbf{E}^*(\mathbf{r}) + \frac{1}{2\mu_0}\mathbf{B}(\mathbf{r}).\mathbf{B}^*(\mathbf{r})\right). \tag{1.40}$$

Consider the fundamental WGMs in a microsphere ($n = 1, \ell = |m|$), the mode volume of a TE mode can be approximately derived [38]:

$$\mathcal{V} \simeq 2\pi^2\, (\frac{\lambda}{2\pi N})^3\, 0.809 \times \ell^{11/6}. \tag{1.41}$$

Consider a silica microsphere with diameter of 40 μm and operation wavelength $\lambda \sim 800$ nm, the corresponding fundamental mode volume is about 210 μm^3 or equivalently 1250 $(\lambda/N)^3$.

1.1.3 FEM simulations of silica microtoroids

Microtoroids are another interesting microcavities [16], since WGMs in these cavities have the advantage to achieve smaller mode volumes, compared to spherical microcavities of the same outer diameter. However, unlike microsphere cavity, the Helmholtz's equations in this cavity is not separable, thus there is still no analytical theory for its WGMs structure and positions. In general, the WGMs of toroids can be characterized by their polarizations and three integer orders (n, m, q), where the azimuthal mode number m and q (the latter being defined as the number of polar antinodes minus one), are similar to the spherical ones, while the order n denotes a radial-like mode number.

Recently, several methods have been developed to numerically solve Maxwell's equations based on techniques like Finite Difference Time Domain (FDTD) [52] or Finite element method (FEM) [53]. Among these techniques, the FEM method has been applied for the simulations in WGM toroidal microcavities [54, 55]. In fact, the three dimensional problem in axis symmetric WGMs cavities is reduced to a two dimension problem and can be easily simulated using a commercial software (Comsol Multiphysics)[3]. Here, this software is used to study the WGMs in toroidal microcavities.

---

[3] Comsol Multiphysics, http://www.comsol.com/

According to the definition of mode volumes in equation (1.40), Table 1.2 gives the comparison of numerical results and approximated values from analytical solution using equation (1.20) and equation (1.41), for a silica microsphere with radius $a = 15$ μm and refractive index $N = 1.453$. The good agreement shows that the FEM method is convenient, especially for the following studies on toroidal microcavities, which presently do not have analytical solutions. One can also note that TE mode has smaller mode volume compared to TM mode, which means that TE mode is better confined and leads to larger diffraction limited Q factor as shown in figure 1.7.

a=15 μm $n = 1, \ell = \lvert m \rvert = 160$	λ_{TE} (nm)	λ_{TM} (nm)	Mode volume (μm^3)
Calculation using equation (1.20) and equation (1.41)	808.91	805.46	123.0(TE)
FEM solutions	809.24	805.87	123.7(TE) 128.4(TM)

Table 1.2: Comparison of FEM solutions and approximated values from analytical solution on a silica microsphere.

1.1.3.1 Mode volume

Since the physical volume of a microtoroid is reduced compared to a microsphere of the same outer diameter, it is of great interest to investigate the mode volumes of their WGMs using FEM modeling. Figures 1.8(a) and (b) show the distribution of electromagnetic energy density for the fundamental WGMs $\text{TE}_{n=1,q=0}$ of a microsphere and a microtoroid. The outer diameter of microtoroid is set to be the same as the diameter of microsphere $D = 30$ μm and the minor diameter is $d = 3$ μm as sketched in the inset. By setting the azimuthal mode order as 160, the resonance position is found to be at 798.4 nm for microtoroid and 809.2 nm for microsphere. This demonstrates that the strong curvature associated to the minor diameter pushes the mode toward the center, resulting in a smaller internal caustic, and therefore a shorter round trip path. The estimated mode volume in the microtoroid is about 66 μm^3, much smaller than the value of 124 μm^3 for the microsphere, demonstrating that an important reduction of the mode volume can be obtained by using microtoroids.

In fact, a microsphere can be treated as a microtoroid whose minor diameter

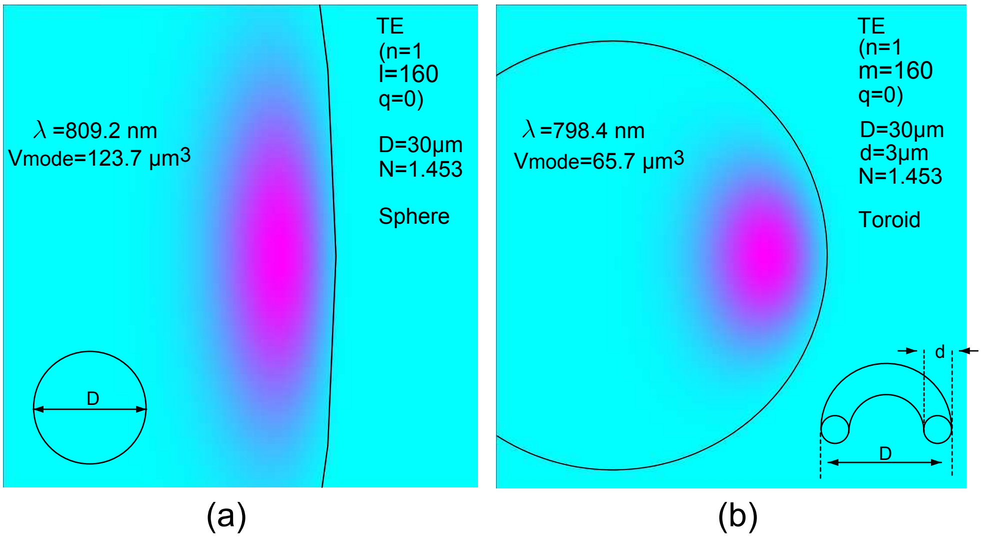

Figure 1.8: FEM calculated electric energy density distributions of two fundamental WGMs for different silica microcavities ($N = 1.453$). (a): $\mathrm{TE}_{n=1,\ell=|m|=160}$ WGM of a silica microsphere with a diameter $D = 2a = 30$ μm. For this mode, the resonance position is $\lambda \sim 809.2$ nm and the mode volume is $V_{mode} = 123.7$ $\mu\mathrm{m}^3$; (b): $\mathrm{TE}_{n=1,m=160,q=0}$ WGM of a silica microtoroid with an outer diameter $D = 30$ μm and minor diameter $d = 3$ μm. For this mode, the resonance position is $\lambda \sim 798.4$ nm and the mode volume is $V_{mode} = 65.7$ $\mu\mathrm{m}^3$.

is equal to its outer diameter. As previously discussed, the microtoroid ($d < D$) has shorter resonance wavelength and smaller mode volume than the microsphere ($D = d$). To further characterize the effect of minor diameter d on the resonance position and mode volume, FEM modeling for toroids with a fixed outer diameter $D = 30$ μm and different minor diameters is carried out. Figure 1.9 shows the mode volumes and resonance positions for $\mathrm{TE}_{n=1,m=160,q=0}$ WGMs as a function of minor diameter d. In this figure, the decrease of minor diameter pushes the mode field slightly toward the center, leading to the reduced light path and thus shorter resonance wavelength. Moreover, it also decreases its mode volume. The decrease of its mode volume becomes obvious when the minor diameter becomes smaller.

1.1.3.2 Higher order modes

For a better understanding of the WGMs of a silica microtoroid, the higher order modes are also studied using FEM simulations. Figure 1.10 gives the electric energy density distributions of different WGMs with TE polarization and $m = 160$. The

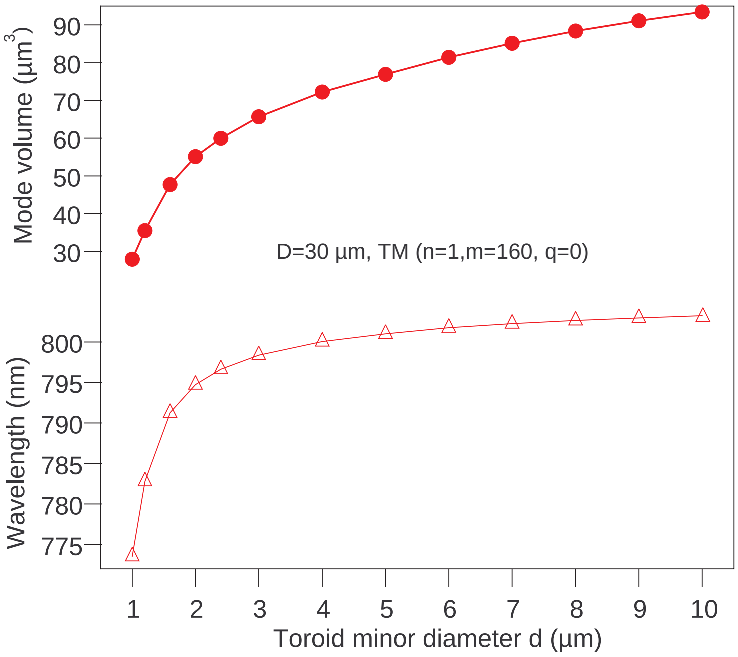

Figure 1.9: FEM calculated mode volumes and resonance positions of $\mathrm{TE}_{n=1,m=160,q=0}$ WGMs for toroids with the same outer diameter $D = 30\ \mu$m and different minor diameter values.

silica toroid is set to possess an outer diameter $D = 30$ µm and a minor diameter $d = 6\ \mu$m, in order to match the parameters of the toroids experimentally studied in Chapter 2. In this figure, one clearly observe that a WGM labeled with integers q and n possesses $q + 1$ antinodes in the polar direction and n antinodes in the radial direction. In the figure, the corresponding resonance positions are also provided. Table 1.3 provides the comparison of mode spacings for this toroid (FEM) and a silica microsphere (approximation from its analytical solution). From this table, one observes large spacing of different q order modes for microtoroid compared to microsphere. This is because the large curvature of a toroid induced by small d value has strong effect on the q order modes. It should be mentioned that all these spacing values are dependent on both D and d values.

1.2 Fabrication of silica microspheres

Over the past decades, several techniques have been devoted to fabricate ultra-high Q dielectric microspheres. Features like an extremely smooth surface and axi-

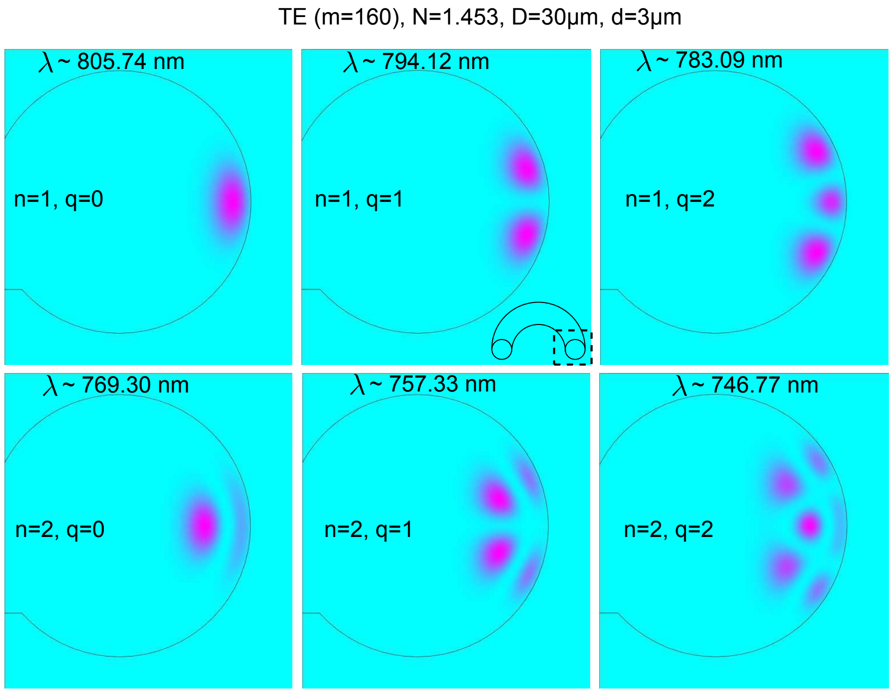

Figure 1.10: FEM calculated electric energy distributions of $\mathrm{TE}_{m=160}$ modes with different n and q values for a silica microtoroid ($D = 30\ \mu$m and $d =\ 6\mu$m).

$m = 160$	$\nu^{\mathrm{TM}} - \nu^{\mathrm{TE}}$ $n = 1, q = 0$	$\nu_{n=2} - \nu_{n=1}$ $q = 0$,TE	$\nu_{q=1} - \nu_{q=0}$ $n = 1$,TE
Microtoroid (FEM solutions)	0.65·FSR	7.9·FSR	2.4·FSR
Microsphere (Analytical solutions)	0.7·FSR	10·FSR	0.01·FSR

Table 1.3: Comparison of mode spacing for the toroid ($D = 30\ \mu$m and $d = 6$ μm) and a silica microsphere with an ellipticity $e = 1\%$.

symmetric shape are basic requirements for the desired high-Q factor, as already discussed. To achieve this purpose, melting is the favorite technique, because it can easily produce dielectric microspheres of both good sphericity and surface smoothness thanks to surface tension. Generally speaking, silica glass has melt point above 800°C. For example, it is about 1650°C for pure silica. To achieve the melting point for glass materials, several heating methods have been successfully applied:

- **Gas flame** Using a microtorch with propane or hydrogen is the most ancient and still rather common technique to melt glass and the early work on solid optical microspheres was based on it [13].

- **Carbon dioxide laser** First introduced in our group[14], it has become the most common technique, because Carbon dioxide (CO_2) laser can be well controlled to fabricate several kinds of WGMs microcavities.
- **Electric arc** Electric arc is another way to achieve the melting process of glass. This technique is generally used with fiber splicing equipment[56].
- **Plasma torch** A microwave plasma torch can also be used to fabricate various active microspheres from the corresponding powders, and produces extremely good sphericity[31].

It's well known that CO_2 laser has a working wavelength in mid-infrared region (typically 10.6 μm), which is efficiently absorbed and transformed to heat glass. Moreover, it is clean and can be precisely controlled. In this work, CO_2 laser is chosen to fabricate both silica microspheres and microtoroids. In our setup, we are able to fabricate ultra-high-Q microspheres of diameter down to 20 μm. In this section, I will introduce the fabrication method of silica microspheres in the present work. This is a simple and efficient method, which uses the same CO_2 laser setup to draw microfibers and melt microspheres successively. First, a single mode fiber without coating is tapered and cut off using CO_2 laser melting. Then, a silica microdroplet at the end of the taper is melted again, resulting in an ultra-high Q factor optical microsphere hold on its mother-fiber, used as a stem to conveniently manipulate it. Before doing this, the main features of our CO_2 laser source will be first described.

1.2.1 CO_2 laser source

High power CO_2 laser has been well developed for industry applications, in both cutting, melting and resurfacing. In the present work, the model 48-1-10 fabricated by SYNRAD company is used. Its maximum power is 10 W. This model requires an optimal water cooling temperature in the range from 18°C to 20°C. Actually, it is cooled down by tap water directly to the range from 17°C to 21°C, which has been verified to be working properly. Some important laser specifications are given in table 1.4:

To achieve the melting point of silica, enough absorption of CO_2 laser power in silica is required. Actually the absorption is dependent on the radiation distribution.

Laser Mode		TEM_{00}
Mode Purity		$> 95\%$
Polarization		Linear(Vertical)
Mode Quality	M^2	< 1.2
Beam Divergence (full angle)	2Θ	4 mrad
Wavelength	λ	$10.2 - 10.8$ μm
Beam Diameter	$2w_0$	3.5 mm
Power Stability		$\pm 10\%$

Table 1.4: Specifications of CO_2 laser model 48-1-10.

It means that the laser beam needs to be focused on a small region. The fundamental properties of Gaussian beams are therefore needed for beam alignment and focusing. Here, a brief review on the formulas is given assuming for simplicity that the quality factor M^2 can be set to 1.

The intensity distribution of the single mode TEM_{00} laser can be expressed as follows:

$$I(r) = \frac{P}{\pi w^2} e^{-2r^2/w^2} \tag{1.42}$$

where r is the distance to the propagation axis, P is the total power, and $w = w(z)$ is the beam radius, conventionally defined as the radius of the contour where the intensity is $1/e^2$ of the maximum. There is a minimum beam size at one position along the z axis, named as the "beam waist" w_0. For a beam propagating at a distance z of the beam waist location, the beam size $w(z)$ is given by:

$$w(z) = w_0 \sqrt{1 + \left(\frac{z}{z_R}\right) 2} \tag{1.43}$$

where z_R is the so-called "Rayleigh range":

$$z_R = \frac{\pi w_0^2}{\lambda} \tag{1.44}$$

For example, consider the parameters given in table 1.4, after the CO_2 laser beam has propagated a distance of 0.5 m, the calculated beam radius is about 2 mm. However for fabrication of silica microspheres with diameter in the range from 20 μm to 100 μm, this laser spot is much too large. For this purpose, the lens formula for a Gaussian beam is introduced [57]:

$$\frac{1}{s + \dfrac{z_R^2}{s - f}} + \frac{1}{s'} = \frac{1}{f} \tag{1.45}$$

where f is the focal length of the lens, s is the distance from beam waist position to the lens and s' is the distance from the image waist position to the lens. Next, the beam waist after the lens (w_0') is given by

$$w_0' = \frac{w_0}{\sqrt{(1-\dfrac{s}{f})^2 + (\dfrac{z_R}{f})^2}} \tag{1.46}$$

Finally the equation (1.46) provides an easy way to estimate the beam size and to design the corresponding setup. In the present work, the distance from CO_2 laser beam waist to the focusing lens is about 1.30 m, thus the corresponding beam waist after the lens is about 90 μm, which is a suitable configuration.

1.2.2 Experimental setup

To better control the melting process, a double beam system is designed. The schematic of the experimental setup is illustrated in figure 1.11(a). All the optical components are chosen for operation wavelength at 10.6 μm: metal-coated silicon mirrors and ZnSe lenses and beam splitters. A beam combiner (BM) with high transmission of about 99% at 10.6 μm and reflection larger than 75% in the visible range is used to combine an Helium-neon red laser (HeNe) with the CO_2 laser beam. The beam splitter (BS) is used to split the CO_2 laser beam into two beams with the same power. These two beams are then focused at slightly separate positions on the propagation axis using identical ZnSe lenses, with a focal length of 63.5 mm. The mirrors M5 to M8 are used to raise the beams. Figure 1.11(b) is a photo of central part of this setup. It shows on the left the long working distance binocular microscope used to monitor the fabrication process.

The setup is used to fabricate silica microspheres of diameter down to 20 μm from commercial single mode fibers (SM980 and SM800). The choice of these silica single-mode fibers is due to their ultra-low losses at low price. However, the direct melting of such a fiber having a diameter of 125 μm would result in rather big microspheres. Therefore, we have developed a simple method to reduce the fiber size in order to produce smaller spheres.

1.2.3 Results

The fabrication process consists of two steps. In the first step, the fiber coating is removed using stripping tool, and the bare fiber is carefully cleaned using lint-free wipes soaked in pure alcohol. Subsequently, it is fixed on an aluminium stick, which

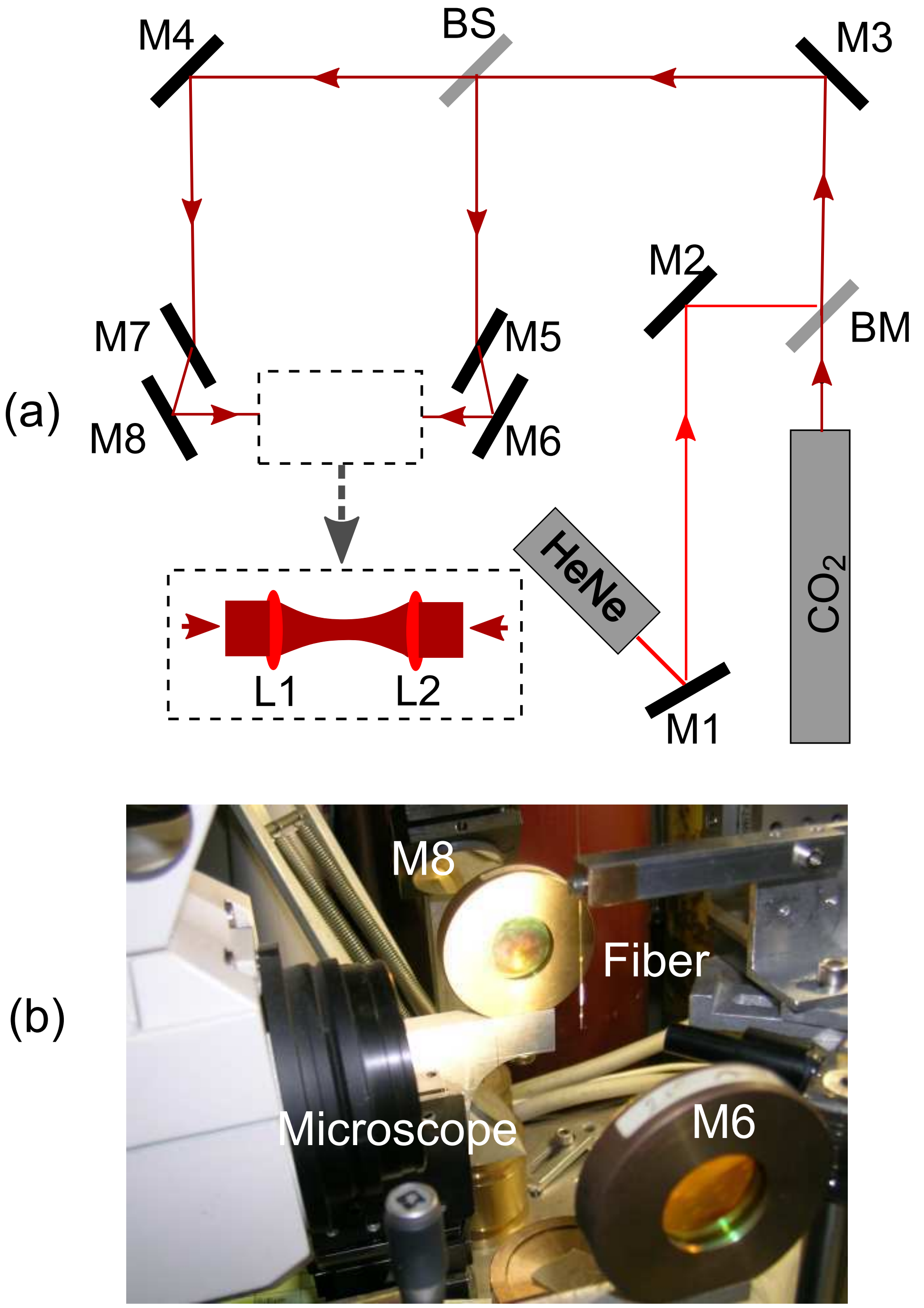

Figure 1.11: (a): Sketch of experimental setup. HeNe and CO_2 are the corresponding lasers. M1–M8 are reflection mirrors; BM is a beam combiner to transmit infrared light and reflect visible light; BS is a 50:50 beam splitter for CO_2 laser. L1 and L2 are ZnSe lenses. (b): Picture of the setup.

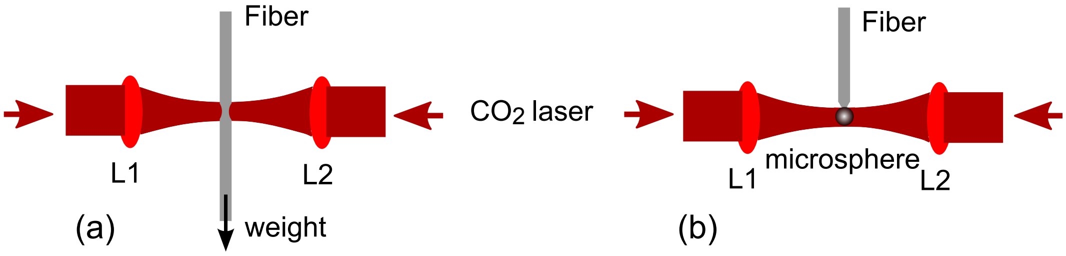

Figure 1.12: (a). Schematic of tapering process. (b). Schematic of microsphere melting.

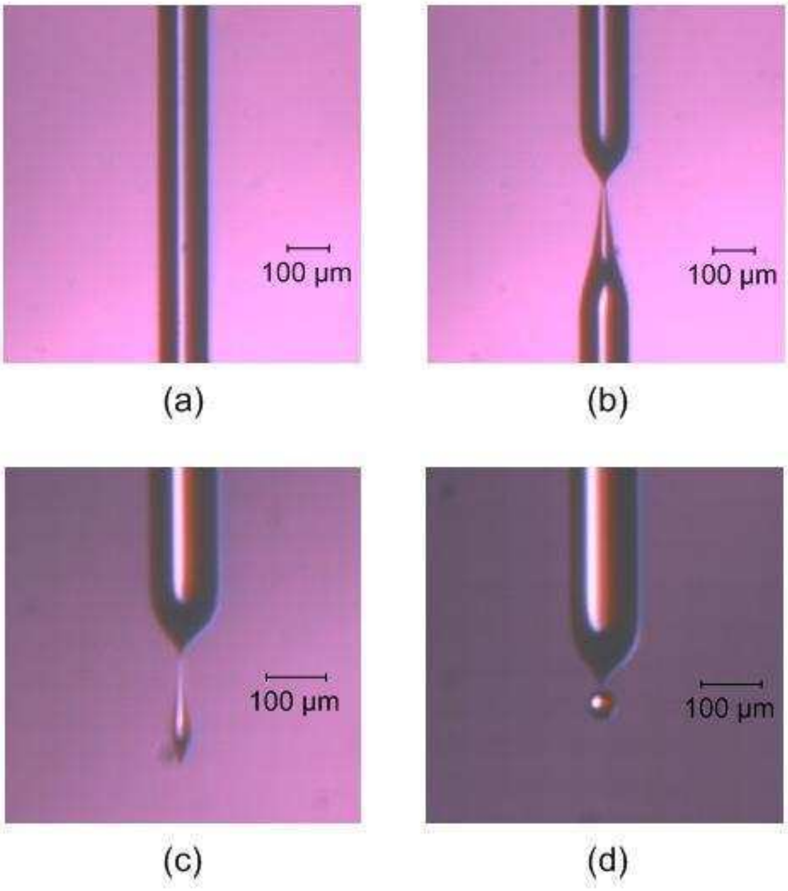

Figure 1.13: (a): The single mode fiber, 125 μm in diameter. (b): the fiber after tapering with a drawing force. (c): the microdroplet formed by cutting the taper. (d): the microsphere with its stem formed from the microdroplet.

is mounted on a three dimensional translator. After aligning it to the overlapping focal zone of the two CO_2 laser beams, it's heated with an estimated power about 0.4 W for each beam. During the heating process, a weight connected to the fiber tip produces forces to draw the fiber, leading to a several micrometer taper waist, as illustrated in figure 1.12 (a). Next, the taper is selectively cut by melting its bottom part, leading to an elongated silica "microdroplet".

In the second step, the silica microdroplet is heated using the same CO_2 laser as illustrated in figure 1.12 (b). When the silica temperature reaches the melting point, surface tension immediately shapes the microdrop into a spherical form. After the laser is turned off, a solid microsphere is produced. All these happen in less than 1 s. The resulting microsphere remains attached to its stem. By changing the mother fiber size, we can easily control the size and ellipticity of the microsphere[50]. Special care should be taken during the last step to avoid unbalance of the two beams, which would result in a strongly asymmetric microsphere. These successive steps and the resulting microsphere are shown as photograph in Fig. 1.13.

1.3 Fabrication of on-chip microtoroids

In recent years, the development of silicon microfabrication techniques has permitted the invention of novel ultra-high Q factor microcavities of toroidal shape and directly integrated on a silicon chip [16]. These microtoroids also own the advantage of precisely controllable size. Toroidal microcavities, as we already mentioned in section 1.1.3, feature at the same time a smaller number of WGM (due to a reduced size in the polar direction) and smaller mode volumes (thanks to a better confinement).

In this section, the fabrication procedure of on-chip toroidal microcavities is described. It is separated into two parts. First, silicon technology is used to produce silica microdisks sitting on a silicon pedestal. This step is performed in Sinaps laboratory (Service de Physique des Matéiaux et Microstructures (SP2M) at CEA-Grenoble) with which we collaborate. Subsequently, the microdisks are melted using a CO_2 laser. This melting step, also termed as "laser reflow", leads to microtoroids having a reduced outer diameter. By this way, the typical Q factor of about 10^4 for microdisks is upgraded to be in excess of 100 million for microtoroids.

1.3.1 Fabrication of microdisks

The procedure of fabrication in SP2M of these undercut silica microdisks, consists of the following steps: Silica layer preparation, photolithography, silica etching

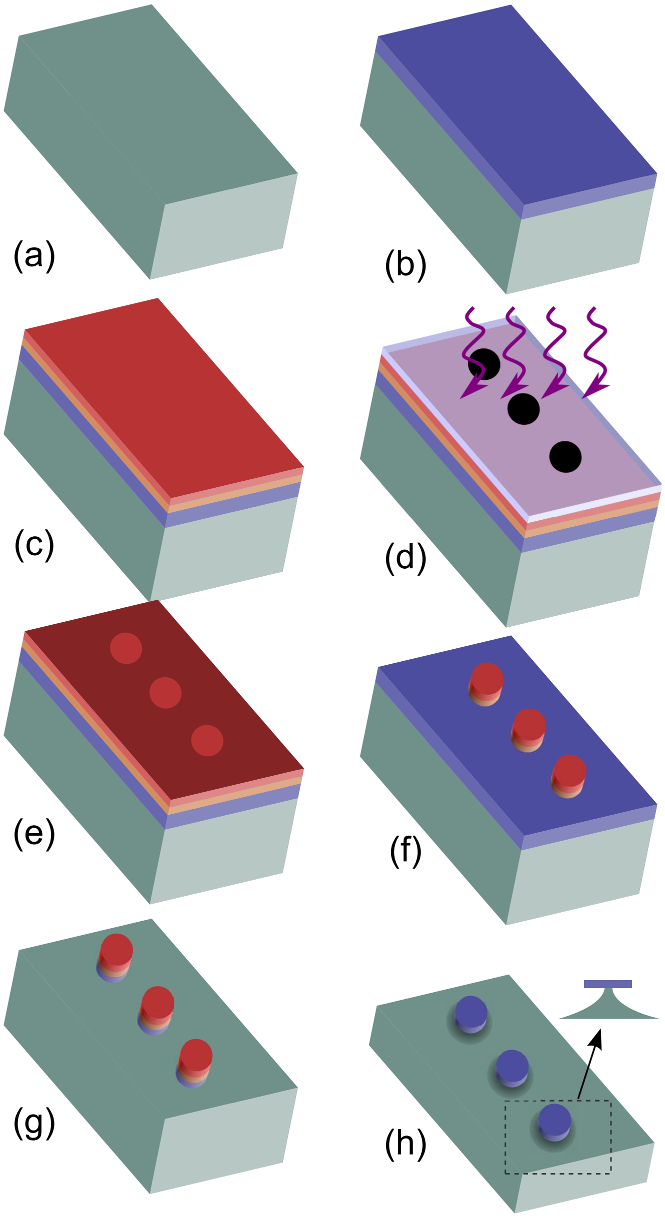

Figure 1.14: Illustration of the microdisks fabrication process flow: (a): Silicon substrate; (b): Thermal oxidization growth of silica layer on silicon wafer; (c): Spin-coating of HNDS bonding layer and positive photoresist; (d): UV light irradiation through the chrome mask; (e), Images of the mask on the photoresist; (f): Microdisks after photoresist development; (g): Wet etching of silica layer using HF solution; (h) Silicon undercutting by reactive ion etching.

and silicon undercut etching.

Silica layer preparation

Figure 1.14(a)(b) illustrates the first step of silica microdisks fabrication. By thermally oxidizing the silicon wafer, a good quality thin layer of silica was grown on the silicon surface. These silica/silicon (SiO_2/Si) substrates were provided by LETI (Laboratoire d'Électronique et de Technologies de l'Information). Thus the detailed fabrication is not given here. The silica layer thickness used in present work is 2.7 μm. The substrate is first cleaved into rectangular parts, so the final dimensions of these samples are typically 20 mm × 10 mm or 20 mm × 5 mm. In fact, some of them need to be cleaved again after the lithography, as will be described below.

Photolithography

The patterning of a microdisk is done through photolithography. This process is carried out in the clean room at PTA (Plateforme Technologique Amont de Grenoble). First of all, a cleaning step is performed. The Si/SiO_2 substrate prepared in the former step is first cleaned using the acetone and isopropanol in a spinner, so that the impurities can be chemically removed. After the cleaning process, the sample is heated on a hotplate at 135 °C for 1 to 2 minutes in order to evaporate any moisture on the silica surface. This cleaning step is strongly required to ensure adhesion of photoresist on the wafer surface.

The positive photoresist used is AZ 1512HS. Typically, a wafer bonding technique can be used for attaching the photoresist on the silica wafer. Here, an intermediate layer of Hexamethyldisilazane (HMDS) is chosen for adhesion bonding between silica and photoresist layer. The HMDS is first evenly deposited on the substrate surface using a spinner. In order to avoid the oxidization of HMDS, the photoresist is immediately spin-coated with a rotation speed at 4000 rpm for 50 s, as shown in Figure 1.14(c). These parameters are selected for fabrication of a 1.2 μm thick photoresist layer. After the deposition of photoresist, one can clearly see an iridescence close to the border of the substrate, which is about 1 mm wide. In these regions, the coating of photoresist is not uniform , because it is affected by the presence of the border. Therefore, the lithography region should not include this part. This is also why some of the substrates should be cleaved again after the lithography process. Subsequently, the samples are quickly placed on a hotplate, so that the solvents can evaporate. They are heated at around 100 °C for 90 seconds. This step is also called “prebaking”.

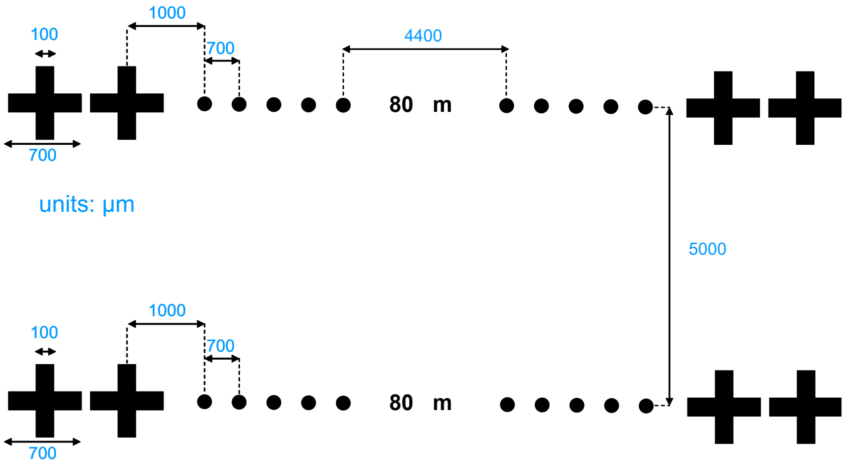

Figure 1.15: Illustration of the chrome mask pattern. The black pattern is deposited with chrome to absorb UV light.

As shown in Figures 1.14(d) and (e), the following step is to transfer the designed pattern to the substrate by exposing it under the corresponding pattern of intense ultraviolet (UV) light. The design of the mask is dependent on the type of photoresist used. Here a positive photoresist is chosen as mentioned above. Thus a typical chrome mask is designed, as illustrated on figure 1.15. The crosses are used to define the microdisk region. The dark pattern is defined with a chrome metal absorbing film covering on a transparent silica blank. So that the positive photoresist which receives the UV irradiation becomes soluble to the photoresist developer, while the other parts remain insoluble. In the present work , the exposure process is typically done with UV-irradiation of about 16 $\mathrm{mW \cdot cm^{-2}}$ and a duration of 7 s.

After irradiation, the photoresist is developed using AZ351 developer in a 1:1 ratio in deionized water for 30 seconds. Then, it is blow-dried using a compressed nitrogen gun, followed by baking at 95 °C for one minute. The resulting patterned photoresist layer on top of silica then acts as a post mask.

Wet etching of silica layer

In this step, the sample after photolithography is immersed into aa aqueous buffered HF/NH_4F solution. The corresponding reaction follows the chemical equation:

$$SiO_2 + 6HF \longrightarrow H_2SiF_6 + 2H_2O \tag{1.47}$$

The bare silica layer (ie without the imaged photoresist mask) is etched, resulting in the transfer of photoresist pattern on the silica layer, as can be seen in figure 1.14(g).

Reactive ion etching

The last step is the isotropic etching process providing microdisk undercut. It is carried out using inductively coupled plasma reactive ion etching (ICP-RIE) on a Surface Technology System (STS). Fist of all, the reactor should be prepared. Before placing the sample in it, an oxygen plasma cleaning is performed in order to remove any contaminations induced by polymer that maybe present in the chamber, since the machine is not only used for the etching of silicon. Next, a second plasma that is used for etching is prepared in the chamber before the actual etching. Between these two plasmas, different cycles of purging gas lines and reactor are performed. The plasma used for etching is a mixture of SF_6 (100 sccm) and argon (50 sccm)[4]. The argon actually plays a role of dilution. The pressure in the chamber is regularly set as 15 mTorr and the RF power is 450 W.

In fact, the photoresist is also removed during the reactive plasma etching. The resulting microdisks with undercuts are shown in figure 1.14(h). The figure 1.16 shows the scanning electronic micrograph of a typical silica microdisk of 66 μm diameter on silicon wafer.

1.3.2 Fabrication of microtoroids

The mechanism of microtoroid fabrication from a silica microdisk on a silicon wafer relies on its undercut. Indeed, silicon is known to be a good thermal conductor, with a conductivity of about 150 $W \cdot K^{-1} \cdot m^{-1}$ at 300 K, which is more than 100 times larger than that of silica (about 1.1 $W \cdot K^{-1} \cdot m^{-1}$). In fact, a planar silica microdisk on the silicon wafer without undercut would be very difficult to melt, because the heat received from CO_2 absorption in the silica layer immediately diffuses to the silicon substrate. In contrast, with a proper undercut, the border of the silica microdisk is thermally isolated from the substrate. It can thus be heated, and its absorption length decreases with temperature [58], while the silicon pedestal transfers the heat to the silicon substrate. When the silica microdisk absorbs enough CO_2

---

[4] SCCM refers to standard cubic centimeters per minute

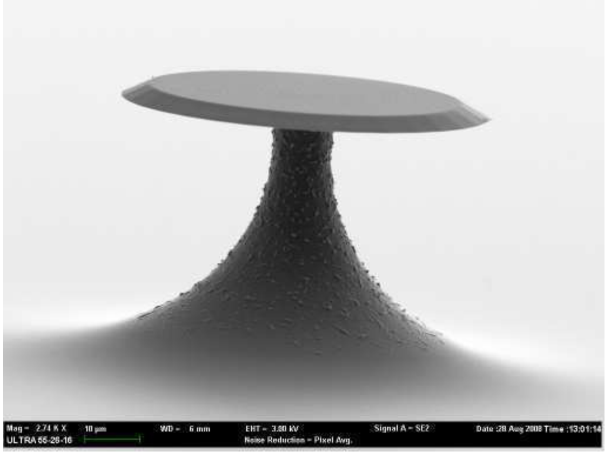

Figure 1.16: SEM image of a silica microdisk with diameter of 66 μm on the silicon wafer.

laser irradiation to reach the melting point in the border, it is then transformed into a toroidal geometry due to surface tension. This process stops by itself when the microtoroid edge reaches a region where melting temperature can not be achieved. All these processes can occur in less than 0.2 s.

In the following part, we introduce the CO_2 optical setup used in this experiment, as shown in figure 1.17. As we already mentioned in figure 1.11, the beam combiner (BM) is used to align a visible laser beam to the same travel axis as CO_2 laser beam, which is a traditional method used in most of CO_2 laser optical system for beam alignment. The M4$'$ mirror is held on a flip optical mount in order to quickly switch the CO_2 beam path for microsphere or microtoroid fabrication. M5$'$ to M7$'$ mirrors are used to lift the laser beam. Compared with microsphere fabrication setup, the setup for microtoroid fabrication is slightly different. Considering the geometry of an on chip silica microdisk, the design of single focused CO_2 beam is enough. However, in order to conveniently align and monitor the melting process, a direct view is needed. It is obtained thanks to a dichroic beam splitter (separating visible and infrared light) inserted between the lens L1 and the sample, and a microscope with 10× apochromatic objective lens and long working distance.

To make a microtoroid, the laser beam is focused on a small region about 100 μm in waist where the microdisk will be placed. In order to precisely control the irradiation time, the laser controller is trigged by pulse signals, which are generated from a National Instruments PCI-6025 card controlled by a computer program. The irradiation time is therefore decided by the pulse width. It should be mentioned

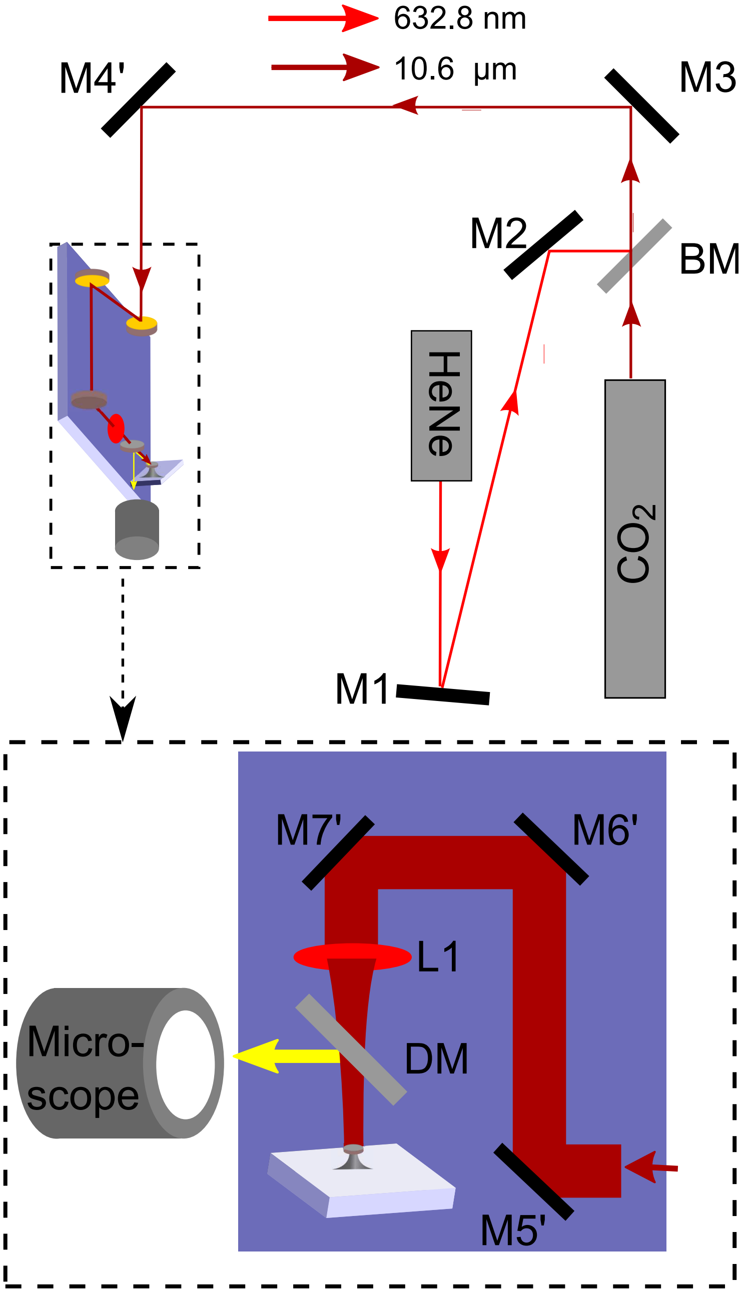

Figure 1.17: Schematic of CO_2 optical setup for microtoroid fabrication. M1-M3 and M4′-M7′ are high reflection silicon mirrors; BM denotes beam combiner and DM dichroic mirror. Mirror L1 is a ZnSe lens. Inset shows a zoom view of the dashed line zone.

that the values of the power and exposure time for best microtoroid fabrication are not constant, because they are strongly dependent on the diameter of microdisk, the undercut size and its position under the irradiation. Here, the pulse width is set to 200 ms. In the case of a 59 μm diameter microdisk with a 22 μm diameter silicon pedestal, the laser power used to melt it is 2 W, when the sample is placed at the focus of the laser beam.

Figure 1.18 shows the optical micrographs of three microcavities, which are taken using a Olympus microscope with 50X objective lens. Figure 1.18 (a) is the image of a silica microdisk. As can be clearly seen, the bright part at the center corresponds to its silica pedestal of diameter about 22 μm. However there seems to be two edges for the disk, this is because of the unperfect RIE etching, results in a slight slope of the edge (as mentioned above in figure 1.16). Figure 1.18 (b) and (c) show two microtoroid images. The first one is asymmetric, because it was not placed at the center of CO_2 laser beam, and has been exposured to the asymmetric laser irradiation. The different minor diameters are related to the distance between the edge and the pedestal, since the entire silica volume is fixed[5]. The second is a nearly perfect microtoroid, with outer diameter of about 44 μm and minor diameter of 6.3 μm. Figure 1.19(c) shows a SEM image of the microtoroid in figure 1.18(c). It should be noted that the dust on its top surface is brought due to an operation accident after fabrication.

---

[5] It is valid only when the CO_2 laser irradiation is not strong to evaporate silica.

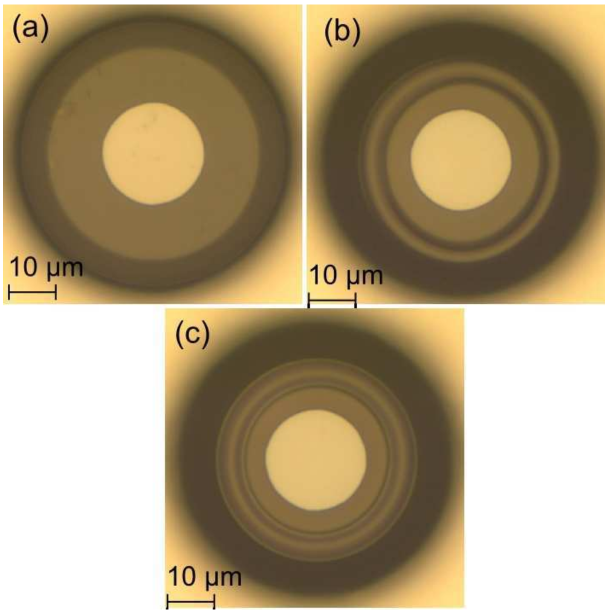

Figure 1.18: Images of the samples. (a) is a silica microdisk. (b) and (c) are two microtoroids.

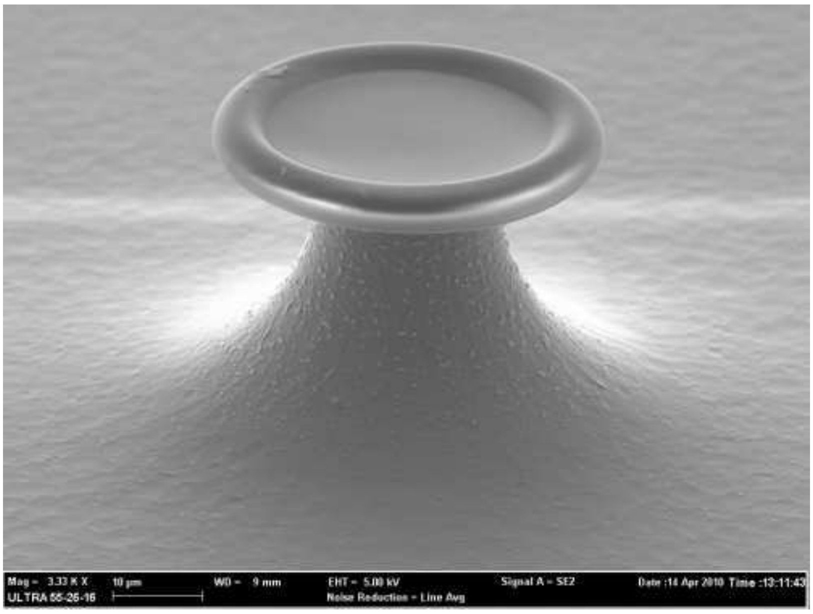

Figure 1.19: SEM image of the microtoroid in figure 1.18(c).

Chapter 2

Excitation of WGMs using a tapered fiber coupler

As previously mentioned, ultra-high Q factor whispering gallery mode microcavities have demonstrated great potential for considerable photonics applications. However, unlike Fabry-Perot cavity, laser beams propagating in free space can not produce efficient excitation of WGMs defined by these microcavities. In the geometric optics point of view, the WGMs being confined by successive total internal reflections, no incoming ray can directly excite them. Therefore, the proper approach for high-Q WGMs excitation is the use of evanescent wave coupling, which utilizes the WGM evanescent field outside the geometrical boundaries of the microcavity.

In last two decades, several evanescent coupling techniques have been developed for this purpose. The approach used in early studies was based on prism couplers [13, 18]. The incident light strikes the inner prism interface with a specified angle to undergo total internal reflection, and the resulting evanescent field is used to excite the WGMs by placing the microcavity in this field. When it is carefully optimized, this technique can achieve rather good coupling efficiency up to 80 percent [20], but this requires difficult beam shaping, and it has a bulky size.

Alternative techniques are based on optical waveguide structures, such as planar waveguides [21, 22], side-polished fiber blocks [23, 24, 25], angle polished fibers [26] and biconical fiber tapers [27, 29]. Up to now, the planar waveguide coupler with a high refractive index has the problem of accessing the efficient coupling to the WGMs in a silica microcavities, because of its difficulty to fulfil both phase matching and evanescent field overlap conditions. In such case, the silica fiber coupler can exhibit good properties for efficient coupling. To the best of our knowledge, a biconical fiber taper has achieved the best coupling efficiency as high as 99.99 % [29]. Compared with prism couplers, fiber taper couplers have several advantages: their high coupling efficiency, extremely low losses and their flexibility for light excitation. On the extraction side, when fiber taper couplers are used for active microcavities, the phase matching conditions generally can not be simultaneously achieved for the pump and the emitted signal. Notice that this problem does not affect prism coupling where output phase matching is automatically ensured by a slight angle change. The technique using angle polished fiber tip [26], interestingly combines fiber technology and prism coupling, but its coupling efficiency with a WGM cavity is still limited.

In this chapter, fiber taper couplers are used to experimentally study the WGMs in silica microspheres and microtoroids. The theory and fabrication of fiber taper couplers will be first introduced. The fiber tapers fabricated in this work can be down to sub-micrometer size to have single mode behavior in the operation wavelength (about 780 nm and 1083 nm). The best transmission of such a fiber taper is as high as 99.5 percent. The optimized coupling efficiency achieved in this work with a taper-microtoroid coupled system is above 99 percent.

To study the optical properties of a single taper coupled microcavity system, an "Evanescent F-P model" is described [38]. The taper-microcavity coupling gap effects on the WGM resonance position, linewidth and coupling efficiency are experimental studied, and then analyzed using the F-P model. Finally, a novel method was developed to directly observe the electromagnetic-field distribution of WGMs in silica microcavities. This distribution is revealed by the excitation efficiency with a tapered fiber coupler swept along the meridian. This method allows one to selectively excite the small mode volume WGM modes, which is of great importance for ultra-low threshold lasing experiments.

2.1 Tapered fiber couplers

2.1.1 Introduction

Tapered optical fibers have been attracting great interest in the past decades, due to their large evanescent fields and strong light confinement. Their use as optical couplers is not only limited to silica microspheres or mirotoroids, but is also working for microdisks [59] and photonics crystal cavities [60]. Moreover, there are more and more potential uses of these fiber tapers, such as sensors [61], supercontinuum light source generation [62], particle manipulation [63] and atom trapping and probing [64].

In general, the evanescent field in a commercial step index single mode fiber locates in its cladding part. To be able to utilize this field, one can either remove the cladding part by chemical etching or by tapering. Tapering is an easy and efficient way to produce an adiabatic coupler with low losses. In this case, the fiber is typically tapered down to micrometer scale or even nanometer scale. The tapering process utilizes a fixed heater or a moving heater to melt the fiber. The heater can be a gas flame [27, 65], a CO_2 laser [66] or a ceramic heater [67, 68]. Actually, a silica fiber is already soften when it is heated to $1100-1200°C$. Hence a butane/air flame is sufficient for this purpose. In my experiment, such a flame is setup for the fabrication of low loss subwavelength fiber tapers, as will be described in the following.

2.1.2 Taper fabrication

The fiber tapers used for the characterization of the passive microcavities were fabricated from single mode fiber SMF-42-A-125-1, whose attenuation at operating wavelength $\lambda = 775$ nm is less than 5 dB/km. Later, for the studies on the active microcavities the emission wavelength of which is around 1080 nm, another single mode fiber was chosen, the Thorlabs 980-HP, with an attenuation less than 3.5 dB/km at operating wavelength $980-1600$ nm. In order to monitor the transmission of the fiber during its tapering process, a single mode laser source is launched into the fiber.

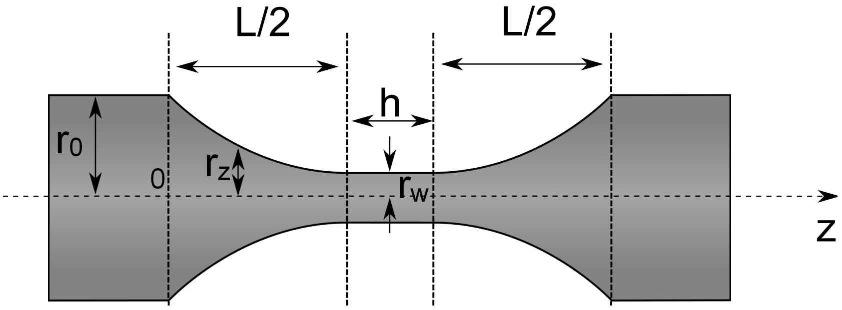

Figure 2.1: The shape of a tapered fiber. r_w is the radius of the waist; h is the hot zone length; L is the pulling length; r_0 is the initial radius; the $z=0$ position is also defined.

As shown in figure 2.2(a), a simple silicon photodiode detector (PD) was used to detect the transmitted laser signal, and the responses of PD were transfered to an oscilloscope and a computer with National Instrument PCI-6025E data acquisition card (DAC). The oscilloscope enables direct monitoring on the signal. The DAC card, working at its maximum sampling rate of 200k samples per second, allowed to record and plot the tapered fiber transmission as a function of the tapering time, or equivalently the elongation length.

We used a specially designed microtorch, in order to produce a short and wide flame. It consists of ten cylindrical stainless steel tubes of 0.8 mm inner diameter. The butane gas flow speed is controlled to have a small and blue flame, which can thus produce temperature above 1200°C. Since the fiber position in the flame is a critical parameter which determines the hot zone length, the microtorch is mounted on a three axis translation stage.

To easily hold the fiber(250 μm with coating), post mountable fiber clamps (Thorlabs) are used. Figure 2.2.(b) gives the photo of this fabrication setup, where a plastic cover is designed to protect the tapering process from the disturbance of unwanted air flow.

Here, the process of tapering is briefly described. First, the fiber coating is striped off over 2 cm, followed by careful cleaning using lint-free wipes soaked in nearly pure alcohol. Subsequently, it is held by the fiber clamps. Then the butane flame is placed under the stripped fiber part with an air gap less than 1 mm. Afterward, the plastic cover is placed over the setup. Finally, the fiber clamps are symmetrically moved apart along two stainless steel rods (R) at the velocity $v = 40\ \mu\mathrm{m}\cdot\mathrm{s}^{-1}$ by two motorized translation stages. These two rods are used to transfer the whole taper without the risk of breaking it after taper fabrication, which is done by fixing the fiber clamps on the rods and moving the two rods and clamps together.

The mathematical shape of a tapered fiber fabricated by heating and pulling was predicted based on mass conservation [69], considering a constant hot zone length and the resulting exponential shape taper. It was successfully applied to fit the taper shape fabricated using this method [65]. According to this model, the taper shape in cylindrical coordinates is described by:

$$r(z) = \begin{cases} r_0 \exp((|z| - h/2 - L/2)/h) & \text{for} \quad h/2 < |z| < (L+h)/2 \\ r_w \equiv r_0 \exp(-L/2h) & \text{for} \quad 0 < |z| < h/2 \end{cases} \tag{2.1}$$

In this equation, $r(z)$ represents the radius of the fiber as a function of the position z, its origin being defined in figure 2.1. The parameter h is the so called “hot zone” length, that is to say the length of softened part where the lengthening and size reduction take place. r_0 and r_w designate the radius of initial fiber and the waist of the taper, respectively. L corresponds to the pulling length.

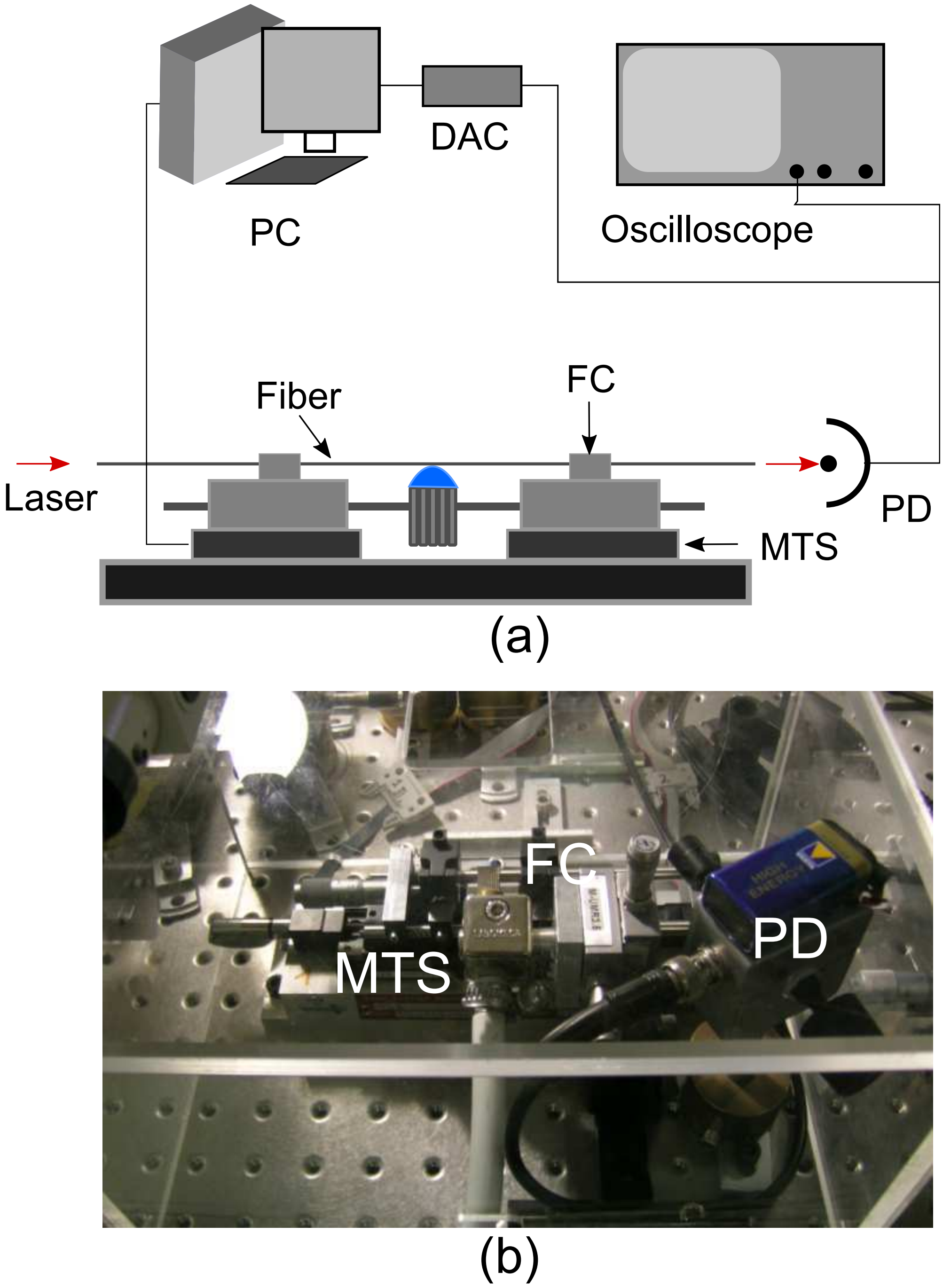

Figure 2.2: (a) Sketch of the taper fabrication setup. DAC: NIDAC 6025; FC: Fiber clamps; R: Stainless steel rods; PD: Silicon photodiode; MTS: Motorized translation stage. (b) The photo of the fabrication setup inside a plastic chamber.

During the tapering process, we observe weak oscillations on the detected transmitted signal, as shown in figure 2.3. These oscillations result from the interference between different modes supported by the tapered fiber.

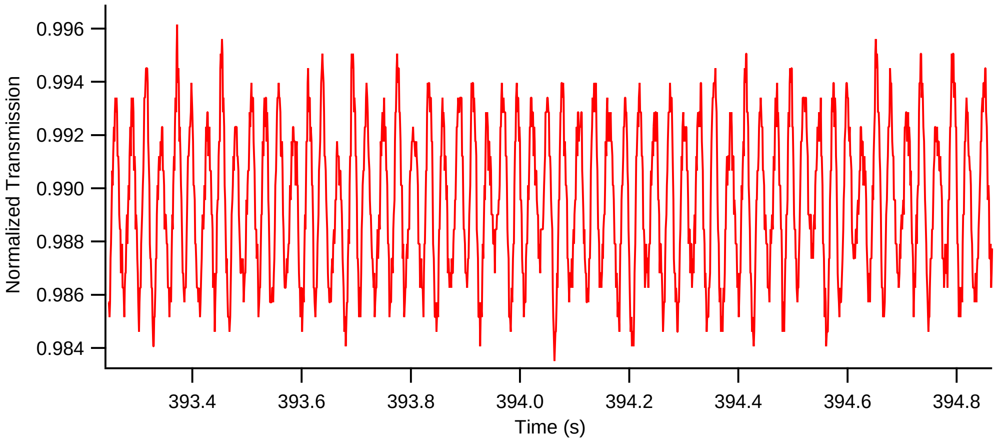

Figure 2.3: A zoom on the detected transmission curve during the tapering process, showing the interference effect between the fiber modes.

2.1.3 Results and discussion

For a thin fiber taper, the light is no longer confined in the core, but travels into a cladding-air based waveguide structure. A more or less adiabatic transition occurs from the core-guided LP_{nm} modes to the cladding-guided modes. One expects that the fundamental LP_{01} will be transferred as adiabatically as possible to the fundamental taper mode which is the HE_{11} mode. The higher order modes are excited from the fundamental mode due to a small defect of adiabaticity. They propagate along the taper with different propagation constant β, and hence recombine at the output with a length- and thickness-dependant relative phase. The observed oscillations therefore result come from the beating of these modes.

Figure 2.4 shows the effective index $N_{\text{eff}} = \beta/k_0$ of taper modes as a function of its radius for the wavelength of $\lambda_1 = 775$ nm. One observes that the last higher order mode cutoff, ensuring single mode operation, occurs at a taper radius of 0.6 μm. For a thick taper, the light is mostly confined inside the silica, leading to an effective index close to $N_{cl} = 1.45$. When the taper size goes down to sub-wavelength scale, the portion of evanescent field outside the taper increases, thus the effective index of the taper goes from 1.45 towards 1.

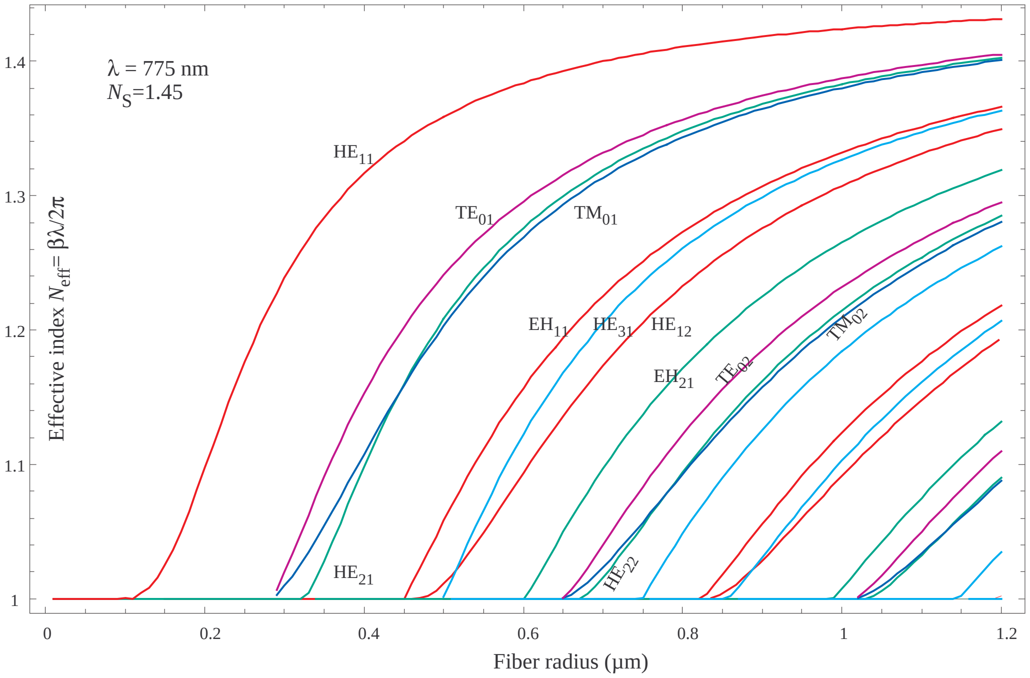

Figure 2.4: Calculated effective index of the low order hybrid modes as a function of the taper radius for wavelength $\lambda = 775$ nm.

Here, we consider the beating of two given local modes, designated by indices $i = 1$ or 2. Because taper radius changes along the propagation axis z, $\beta_i(r)$ is z-dependent. Hence the accumulated relative phase can be written as:

$$\Phi_{12}(L) = 2\{\int \Delta\beta_{12}(r(z))\,dz + \Delta\beta_{12}(r_w)\frac{h}{2}\} \tag{2.2}$$

where r_w is the radius of taper waist, h is the hot zone length, L is the elongation length. When considering the relation of r_w vs. L, as shown in equation 2.1, a simple derivation leads to the spatial angular frequency:

$$K_{12} = \frac{d\Phi_{12}}{dL} = \Delta\beta_{12}(r_w) - \frac{r_w}{2}\frac{d}{dr}(\Delta\beta_{12}) \tag{2.3}$$

During the tapering process, this frequency can be derived by performing in real time a “short time Fourier transform” of the oscillations, resulting in a frequency-time image which is named a spectrogram or a sonogram in acoustics [70]. Figure 2.5 shows the beating signal and the sonogram for a single-mode fiber taper fabricated for operating wavelength $\lambda = 1064$ nm. The tapering process takes about 8 minutes with an elongation length $L \approx 36.9$ mm. The upper red curve is the transmission curve,plotted as a function of time t (top axis) or the elongation length $L = 2vt$ (bottom axis), which shows a final transmission as high as 99%. The general amplitude of the oscillations results from the different efficiency of higher order modes excitation and recombination. However, its variation during the tapering process is due to the beating of different frequency components. All of these components involve the fundamental mode, because the higher order mode amplitudes are too small to make their interference visible.

The bottom black image corresponds to the spectrogram derived from these oscillations. It should be mentioned that the center straight curve (50 Hz) is due to the power line noise, which has no physical meaning here.

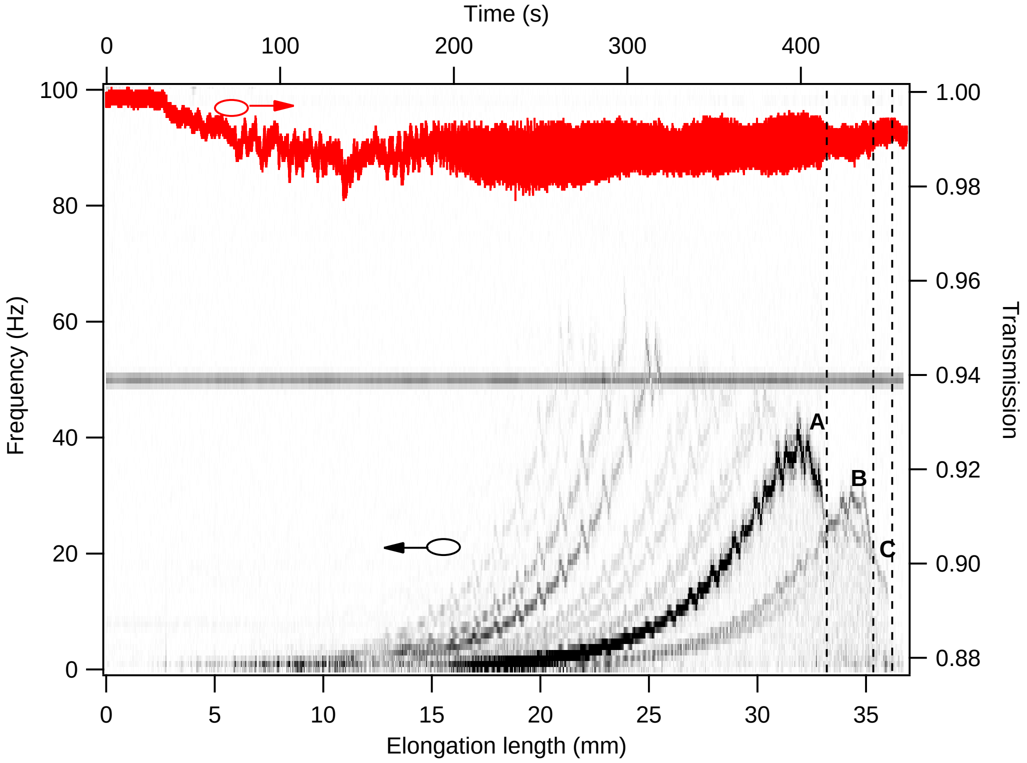

Figure 2.5: Fiber transmission during the tapering process and the corresponding spectrogram. The vertical curves denote the higher order modes cutoff.

The cutoff of different modes have also been observed from its spectrogram, which actually reveals the cutoff of different higher order modes. “A”, “B” and “C” denote the beating of the fundamental mode HE_{11} with the higher order modes HE_{12}, HE_{21} and TE_{01}, respectively. This has been verified by a previous work in our group [65]. Significantly, the spectrogram analysis method allows one to control the modes of a fiber taper and its final size, which is very useful for the manufacturing of single-mode subwavelength microfibers.

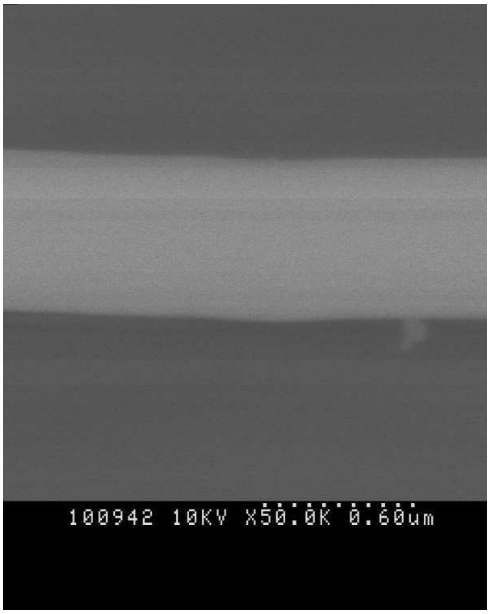

Figure 2.6: SEM image of the taper waist.

To measure the size of this fiber taper, it was transferred to a thin U-shaped metal plate, where the waist was kept in the air. The waist diameter measurement was performed using scanning electron microscope (SEM) as shown in Figure 2.6. This gives a diameter of about 690 nm.

The produced fiber tapers typically have an average transmission of 90% and the best ones can exceed 99%. The spectrogram method provides a convenient way to estimate the size of a taper during its fabrication process.

After fabrication, the fiber clamp holders are fixed on the rod, so that the whole taper stage can be transferred for further experiments on WGM microcavities, without the risk of breaking the fragile taper.

2.2 Modeling the Coupling

The theory described in chapter 1 gives the insight view on the WGMs in a microcavity, and the theory provided in the previous section describes the modes and the effective index in a fiber taper. We want now to describe the coupling mechanism occurring when the evanescent field of a fiber taper and a WGM microcavity are brought together . This problem could be solved using coupled mode theory [71, 20] but a better physical insight is obtained by another approach. This model of the excitation of the WGMs was first introduced in the thesis of François Treussart [38]in our group, in the context of prism coupling, and can be named the model of "Evanescently coupled Fabry-Perot model". It is in some sense similar to the approach developed in Ref. [72], except that in this paper the coupling gap is handled as a whole, while we will here look at the physics of evanescent waves inside it.

2.2.1 Description of the model

Figure 2.7(a) shows the schematic of a fiber taper coupled WGM microcavity system, where E_{in} denotes the amplitude of the input optical field, and E_{out} is the amplitude of transmitted or output field. g represents the coupling gap between the taper coupler and a cavity. E_{cav} is the amplitude of internal field just after the input. The schematic of "Evanescent F-P model" is presented in figure 2.7(b). In this model, an input mirror with transmission $T(g)$ as a function of g represents the evanescent field coupling between a fiber and a WGMs cavity. The other mirror can describe the radiation losses or other coupling components, like a second fiber taper [73] or InAs/GaAs quantum dots [19]. Also shown is the round trip internal absorption loss coefficient $P/2$. The optical field in the cavity after one round trip is noted E'_{cav}.

2.2.1.1 Equations of the fields

In this model, the input mirror is characterized by the reflection coefficient $-r$ (outside), r (inside) and the transmission coefficient t (for both outside and inside). For the second mirror, the corresponding coefficients are given as r' and t'. First, we consider only the case of perfect mode matching, where the whole incoming field can enter into the cavity and excite the mode under study. In this case, the amplitudes of the optical field can be written as:

$$\left\{ \begin{array}{ll} E_{\mathrm{cav}} = t\ E_{\mathrm{in}} + r\ E'_{cav} & E'_{\mathrm{cav}} = r'\ e^{-P/2} e^{i\phi}\ E_{\mathrm{cav}} \\ E_{\mathrm{out}} = -r\ E_{\mathrm{in}} + t\ E'_{cav} & E'_{\mathrm{out}} = t'\ E_{\mathrm{cav}} \end{array} \right. \tag{2.4}$$

where E'_{cav} is the amplitude of internal field after one round trip, expressed with $e^{-P/2}$ which represents the internal absorption loss in one round trip, r' which contains the radiation losses, and $e^{i\phi}$ which represents the round trip phase. In the following, the E'_{out} will be ignored, since it's not significant here.

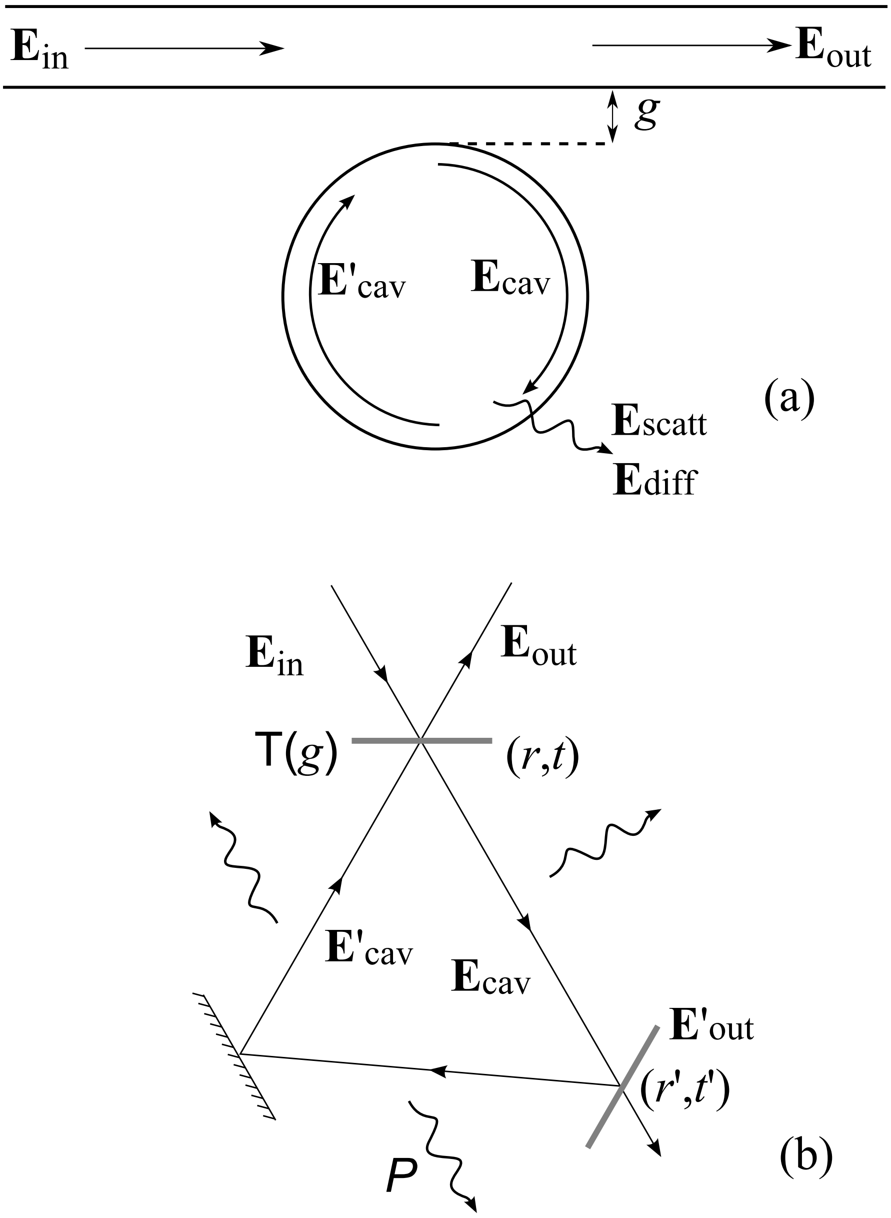

Figure 2.7: (a) Schematic of the fiber taper coupled WGM microcavity system. The gap g is the air distance between the fiber and the cavity. (b) Schematic of a Fabry Perot cavity as a model for the coupling of WGMs in a mirocavity. The transmission of the input mirror is $T(g)$, which in the case of evanescent coupling is dependent on the gap g. P designates internal optical loss, and T' describes the other radiation losses.

From equations (2.4) we obtain

$$\left\{\begin{aligned} E_{\text{cav}} &= \frac{t}{1-\ r\,r'\,e^{-P/2}\,e^{i\phi}}\,E_{\text{in}} \\ E_{\text{out}} &= \left(-r+\frac{t^2\,r'\,e^{-P/2}\,e^{i\phi}}{1-r\,r'\,e^{-P/2}\,e^{i\phi}}\right)E_{\text{in}} \end{aligned}\right. \tag{2.5}$$

So the (amplitude) reflection coefficient of the cavity is given by:

$$r_{\text{FP}} = \frac{E_{\text{out}}}{E_{\text{in}}} = \frac{-r+r'\,e^{-P/2}\,e^{i\phi}}{1-r\,r'\,e^{-P/2}\,e^{i\phi}}\ . \tag{2.6}$$

This coefficient has a resonance when the round trip phase ϕ is an integer multiple of 2π. Therefore, if we consider only one given resonance, we can replace $e^{i\phi}$ by $e^{i\delta\phi}$, where $\delta\phi = \phi - 2m\pi$ (with $m \in \mathbb{Z}$).

Because the WGM microcavities have a high finesse, we can assume that the mirror transmissions $T = |t|^2$, $T' = |t'|^2$ and the internal losses P verify $T, T', P \ll 1$. Then a limited expansion gives :

$$e^{-P/2} \simeq 1 - P/2 \quad r = \sqrt{1-T^2} \simeq 1 - T/2 \quad r' = \sqrt{1-T'^2} \simeq 1 - T'/2 \tag{2.7}$$

and, in the neighborhood of a resonance, as long as $\delta\phi \ll 2\pi$:

$$e^{i\delta\phi} \simeq 1 + i\delta\phi \tag{2.8}$$

So, neglecting all the second order terms, the expression of the reflection coefficient r_{FP} in equation (2.6) becomes:

$$r_{\text{FP}} = \frac{E_{\text{out}}}{E_{\text{in}}} \simeq \frac{\dfrac{T-(T'+P)}{2}+i\delta\phi}{\dfrac{T+(T'+P)}{2}-i\delta\phi} \tag{2.9}$$

Here, the "reflected" signal is the field that escapes from the coupling region, which should be identified to the field transmitted by the taper. This leads to the normalized (intensity) transmission $\mathcal{T}_{\text{out}}$ at the taper output:

$$\mathcal{T}_{\text{out}} = \frac{\mathcal{P}_{\text{out}}}{\mathcal{P}_{\text{in}}} = \left|\frac{E_{\text{out}}}{E_{\text{in}}}\right|^2 = 1 - \frac{T\,(T'+P)}{\left(\dfrac{T+T'+P}{2}\right)^2+\delta\phi^2} \tag{2.10}$$

One notes that, on resonance, when the total internal losses $P + T'$ match the coupling losses T, the transmission $\mathcal{T}_{\text{out}}$ drops to 0. This effect is known as "critical coupling". Moreover, we can observe that the internal losses P can not be completely distinguished from the radiation losses T', and we will merge them in the so called "intrinsic" losses, in contrast with the "coupling losses" represented by T.

It is more useful to write these expressions in terms of angular frequency by using the fact that $\phi = N\omega/c\ L$, where L is the round-trip length and N the internal refraction index. This introduces the FSR of the cavity $\Delta\omega_{\text{FSR}} = c/NL$, such that $\delta\omega = \Delta\omega_{\text{FSR}}\delta\phi$. In the case of WGM, we will furthermore write $N = N_S$ for silica, and $L = 2\pi\, a$, so that $\Delta\omega_{\text{FSR}} = c/2\pi N_S a$. Using the same scaling factor, we introduce the intrinsic and coupling linewidths :

$$\gamma_I = \Delta\omega_{\text{FSR}}\ (P + T')\ , \quad \text{and} \quad \gamma_C = \Delta\omega_{\text{FSR}}\ T\ . \tag{2.11}$$

With these notations, the intrinsic and coupling finesses are:

$$\mathcal{F}_I = \frac{2\pi}{T} = \frac{2\pi\Delta\omega_{\text{FSR}}}{\gamma_I} \quad \text{et} \quad \mathcal{F}_C = \frac{2\pi}{T' + P} = \frac{2\pi\Delta\omega_{\text{FSR}}}{\gamma_C}\ , \tag{2.12}$$

and the taper transmission writes :

$$\mathcal{T}_{\text{FP}} = 1 - \frac{\gamma_I\gamma_C}{(\frac{\gamma_I + \gamma_C}{2})^2 + \delta\omega^2}\ . \tag{2.13}$$

However we need to take into account a small mismatch which is difficultly avoided between the incoming mode and the mode of the cavity. For this purpose we introduce a phenomenological complex overlap parameter α, with $|\alpha| \in [0, 1]$ which measures the fraction of the incoming field that actually contributes to excite the cavity. Therefore, equation 2.4 should be rewritten as follows:

$$\left\{ \begin{array}{ll} E_{\text{cav}} = \alpha\ t\ E_{\text{in}} + r\ E'_{cav} & E'_{\text{cav}} = r'\ e^{-P/2} e^{i\phi}\ E_{\text{cav}} \\ E_{\text{out}} = -r\ E_{\text{in}} + \alpha^*\ t\ E'_{cav} & E'_{\text{out}} = t'\ E_{\text{cav}} \end{array} \right. \tag{2.14}$$

So the following equation are obtained for the taper transmission and the cavity buildup:

$$\left\{ \begin{array}{l} \mathcal{T}_{\text{FP}} = 1 - |\alpha|^2\ \dfrac{\gamma_I\gamma_C}{(\frac{\gamma_I + \gamma_C}{2})^2 + \delta\omega^2} \\ \dfrac{\mathcal{P}_{\text{cav}}}{\mathcal{P}_{in}} = \left|\dfrac{E_{\text{cav}}}{E_{\text{in}}}\right|^2 = \dfrac{c}{2\pi N_S a} \dfrac{|\alpha|^2\ \gamma_C}{(\frac{\gamma_I + \gamma_C}{2})^2 + \delta\omega^2}\ . \end{array} \right. \tag{2.15}$$

The signal detected at the output

In general, we investigate the microcavity by detecting the throughput of the fiber taper on the output photodetector : $I_{\text{PD}}(\delta\omega) = \mathcal{T}_{FP}(\delta\omega) \times I_{in}$. In the wavelength range where the WGMs are not excited (out off resonance $\delta\omega \gg \gamma_I + \gamma_C$, or weak coupling $\delta\gamma_C \ll \gamma_I$), one has $\mathcal{P}_{\text{out}} = \mathcal{P}_{\text{in}}$ or equivalently $\mathcal{T}_{\text{FP}} = 1$. When a WGM is excited, the transmitted signal decreases. Therefore, to characterize the effect of a signal coupling into a WGM resonance, we can introduce the so-called "dip" parameter dip, defined by:

$$\mathcal{D}(\delta\omega) = 1 - \mathcal{T}_{\text{FP}} \tag{2.16}$$

Taking into the expression of $\mathcal{T}_{\text{FP}}$ in equation 2.15, it is then written as follows:

$$\mathcal{D}(\delta\omega) = |\alpha|^2 \frac{\gamma_I \gamma_C}{(\frac{\gamma_I + \gamma_C}{2})^2 + \delta\omega^2} \tag{2.17}$$

According to this equation, we recognize that a WGM resonance has a Lorentzian shape of full width at half maximum (FWHM) $\gamma_{\text{tot}} = \gamma_I + \gamma_C$. Considering the definition of quality factors $Q = \omega/\Delta\omega$ where $\Delta\omega$ is the FWHM, one has $Q = \omega/\gamma_{\text{tot}}$, leading to the same result as in equation (1.35). This also means that the intrinsic Q factor of a microcavity can be measured when the losses induced by the taper are small enough, *i.e.* γ_C is very small with respect to γ_I, as will be discussed later. On resonance, the dip is:

$$\mathcal{D}(\delta\omega = 0) = |\alpha|^2 \frac{4\gamma_I \gamma_C}{(\gamma_I + \gamma_C)^2} \tag{2.18}$$

From equations (2.17) and (2.15), the build-up factor of the circulating power inside the cavity is given as follows:

$$\frac{P_{cav}}{P_{in}} = \frac{c}{2\pi N a} \frac{|\alpha|^2}{\gamma_I} \mathcal{D}(\delta\omega) = \frac{|\alpha|^2 F_I}{2\pi} \mathcal{D}(\delta\omega) \tag{2.19}$$

where F_I is the intrinsic cavity finesse, defined as FSR divided by the FWHM. This equation indicates that the cavity build-up factor is proportional to its intrinsic finesse. The energy storage in a cavity is $W_{cav} = P_{cav}\tau_R$, where $\tau_R = 2\pi Na/c$, so it is also expressed as follows:

$$W_{cav} = \frac{|\alpha|^2}{\gamma_I} \mathcal{D}(\delta\omega) P_{in} \tag{2.20}$$

2.2.1.2 Effects of the coupling gap g adjustment

In this subsection, we will analyze the modification of the dip induced by the gap tuning. These modifications are characteristic features of the evanescent coupling, based on the so-called frustrated total internal reflection phenomenon (FTIR).

From equation (2.18), we deduce that two conditions should be fulfilled at the same time to achieve critical coupling condition. The first one the condition $\gamma_I = \gamma_C$, which will be discussed here, while the second one is the mode matching condition – mostly gap independent – and for more simplicity we will assume that it is properly achieved, ensuring the condition $|\alpha| = 1$.

The gap effect on the width

Note that value of the intrinsic Q factor of a given microcavity is a fixed parameter, leading to a fixed γ_I, and the coupling condition will thus be analyzed through the tuning of the γ_C, which is related to the evanescent gap g.

Therefore, we introduce the exponential dependence of the transmission T as a function of the coupling gap g [38]. This can be written as follows[1]:

$$T = T_0 \ \exp(-2\kappa g), \quad \text{so} \quad \gamma_C = \gamma_C^0 \ \exp(-2\kappa g) \tag{2.21}$$

where $\kappa^{-1} \approx (N_\mathrm{S}^2 - 1)^{-1/2} \ \lambda/2\pi$ represents the evanescent wave characteristic depth. Here γ_C^0 denotes the coupling losses when the coupler is in contact with the cavity.

Looking into the expression (2.18) of the dip, this leads to a dip on resonance as a function of the g given by the expression:

$$\mathcal{D}(\delta\omega = 0) = \frac{1}{\cosh^2 \kappa(g - g_c)} \tag{2.22}$$

where the “critical coupling” gap g_c ensuring $\mathcal{D}(\delta\omega = 0) = 1$ is defined by :

$$g_c = \frac{1}{2\kappa} \ln \frac{\gamma_C^0}{\gamma_I} \ . \tag{2.23}$$

(a) The critical coupling region: $\gamma_C = \gamma_I$ or $g = g_c$

As mentioned above, this position is of great importance for both active and passive devices. The corresponding dip on resonance reaches its maximum value 1, thus the

---

[1] This mathematical form relies on the assumption that the evanescent field decreases with an exponential dependance, which is legitimate for large sphere and/or prism coupling, but for smaller spheres and/or thin tapers is only an approximation.

output signal drops down to zero. Also the loaded linewidth at this position is twice of the intrinsic linewidth. The circulating power in the cavity is express as:

$$P_{cav} = \frac{F_I}{2\pi} P_{in} \tag{2.24}$$

For the cavities used in this work, the value of finesse is typically on the order of 10^5 - 10^6. Consider a modest input power 1 μW and $\mathcal{D} \approx 1$ in an optimized coupling conditions, the resulting circulating power in the cavity P_{cav} can be larger than 100 mW.

(b) The undercoupled region: $\gamma_C \ll \gamma_I$ **or** $g > g_c$
In this condition, the coupling gap g is large, so the measured loaded linewidth is treated as asymptotic unloaded linewidth, which is determined by its intrinsic losses. This is a common approach for obtaining the intrinsic Q factor of a cavity.

The related circulating power inside the cavity can be thus written as follows:

$$P_{cav} = \frac{F_I}{2\pi} \frac{4\gamma_C}{\gamma_I} P_{in} \propto \exp(-2\kappa g) \tag{2.25}$$

As $\gamma_C \ll \gamma_I$, only a small portion of the input light is coupled into the cavity.

(c) The overcoupled region: $\gamma_C \gg \gamma_I$ **or** $g < g_c$
In the opposite, when g is smaller than g_c, the circulating power inside the cavity is expressed as:

$$P_{cav} = \frac{F_I}{2\pi} \frac{4\gamma_I}{\gamma_C} = 4\frac{F_C}{2\pi} P_{in} \propto \exp(+2\kappa g) \tag{2.26}$$

where F_C is the finesses determined by the coupling losses. The circulating power is limited by the losses induced by the coupler. In this conditions, the light can enter easily into the cavity but flows out very fast too, and the coupling efficiency becomes very weak again.

The gap effect on the resonance position

Another important feature, though often ignored, arising from FTIR is the phase change on reflection experienced by evanescent waves. Hence the reflection coefficient r involved in (2.4) or (2.14) has a given non-zero phase. As the corresponding phase factor is multiplied by $T(g)$, it introduces a resonance frequency shift $\Delta\omega_C$ which depends exponentially on the gap g:

$$\Delta\omega_C = \Delta\omega_C^0 \ \exp(-2\kappa\, g). \tag{2.27}$$

Here $\Delta\omega_C^0$ is, like for γ_C^0, the value achieved in contact. This shift is quite obvious on experimental data (see 2.22). Its accurate theory and use for mode identification will be presented in the thesis of Yves Candela, as well as its dependance with respect to α.

Summary

To conclude, with this model of "Evanescently coupled Fabry-Perot" which captures most of the experimental observation, we have a good description of the gap effect on the WGM excitation, and provides an efficient way to analyze our experimental data, as will be shown in the following section. As an example, in figure 2.2.1.2(a) we plot the dip $\mathcal{D}$ as a function of the gap g, using typical values of $\kappa = 2\pi/780$ nm and $g_c = 300$ nm. The critical coupling gap g_c clearly separates the two regions of undercoupling and overcoupling region. In figure 2.2.1.2(b) the effect of g on the shift and linewidth of a resonance is shown, using typival values of $\Delta\omega_I = 15$ MHz, $\Delta\omega_C^0 = 3$ GHz and $\Delta_{shift}^0 = 900$ MHz.

2.2.2 WGM Doublets

In the previous work done in 1995 in our group [48], it was discovered that the high Q factor WGMs above 10^8 typically split into doublet mode structures. It was suggested that such a splitting is due to the coupling between clockwise (CW) and couterclockwise (CCW) WGMs, which results from the internal backscattering caused by surface roughness or density fluctuations in silica which behave as Rayleigh scatterers. These two components, corresponding to standing waves, are called symmetric and asymmetric modes. This backscattering effect induces some feedback which has been used for the laser frequency-locking application [21]. Several papers have been devoted later to refine this interpretation [49, 74]. In 2007, an experiment using a subwavelength fiber tip as a Rayleigh scatter to control the back scattering was successfully carried out by V. Sandoghdar group to examine this mechanism [75]. Meanwhile, this doublet structure in an ultrahigh Q WGM microcavity sensor has been also used to detect single nanoparticle [76].

There is therefore a need to elaborate the "Evanescent F-P model" to analyze these doublet structures, as they will be frequently observed in the characterization of both passive and active ultra-high Q WGM silica microcavities. The doublet structure in the transmission can phenomenologically be expressed as follows:

$$I_r = \left| 1 - (\alpha_1 \frac{\gamma_C}{\gamma_1/2 - i(\delta\omega + \Delta\omega/2)} + \alpha_2 \frac{\gamma_C}{\gamma_2 - i(\delta\omega - \Delta\omega/2)}) \right|^2 \tag{2.28}$$

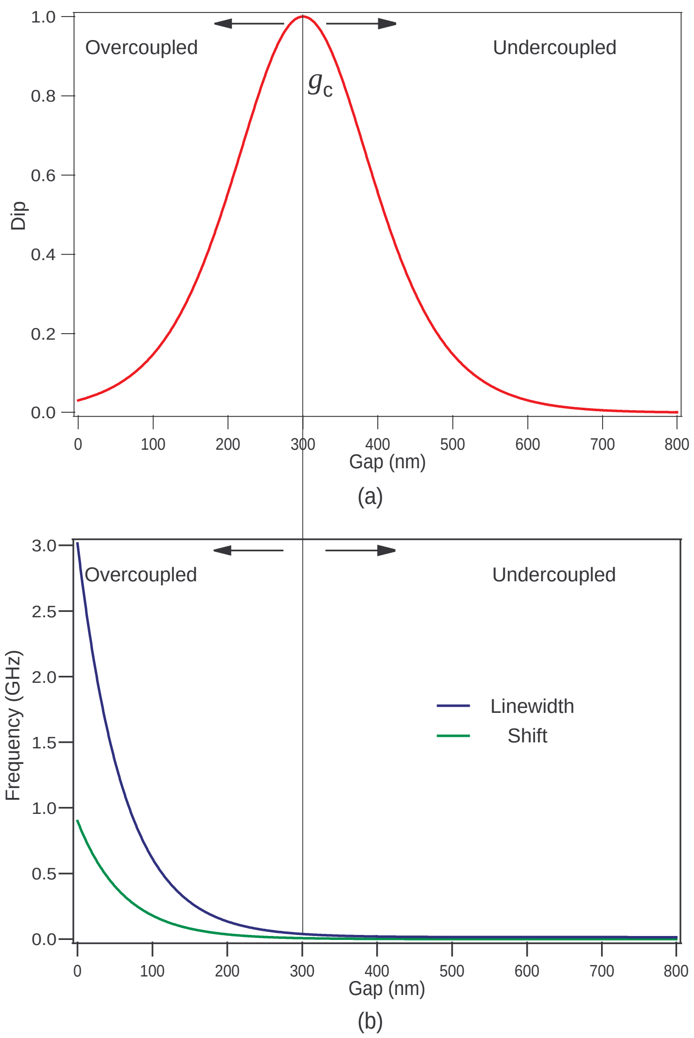

Figure 2.8: (a) Plot of dip as a function of the coupling gap (g) for $\kappa = 2\pi/780$ nm and $g_c = 300$ nm. Undercoupled region: $g < g_c$; Overcoupled region: $g > g_c$. (b) Plot of the shift and linewidth of a resonance as a function of g.

where α_1 and α_2 are the coupling efficiency coefficients of each mode, γ_1 and γ_2 their widths, $\Delta\omega$ their spacing in pulsation. Usually, when scatterers are uniformly dispersed in the cavity, and when the excitation is done by a traveling wave, one has $\alpha_1 = \alpha_2$ and $\gamma_1 = \gamma_2 = \gamma_I + \gamma_C$. However, in some special cases, one can also observe strongly asymmetric doublets.

In figure 2.9 is plotted a theoretical transmission spectrum of a WGM doublet calculated in undercoupled region where $\gamma_C \ll \gamma_I$, in the case where $\Delta\omega \ll \gamma_I$.

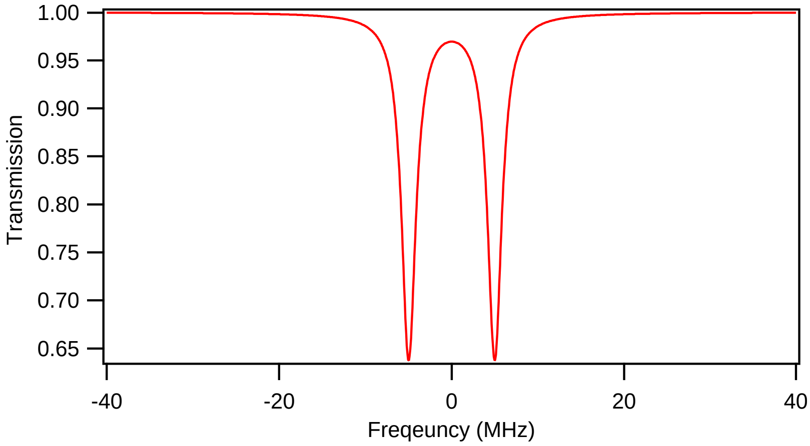

Figure 2.9: Calculated transmission spectrum of a WGM doublet.

2.3 Excitation of WGMs in microspheres

In previous sections, we have reviewed the theory background of the WGMs in microspheres and the fiber tapers, followed by the detail introduction of the technology used in the fabrication of these cavities and taper couplers. Moreover, an "evanescent Fabry-Perot model" has been just described for a good understanding of the coupling mechanism. In this section, the experimental details about the excitation of these WGMs in a silica microsphere are presented. First, I will introduce the design and functionality of our experimental setup. Subsequently, a new method to map the electromagnetic field distribution is developed, which allows one to identify and excite the small mode volume WGMs in silica microspheres. It is also been validated by successful theoretical fit on the mapping result. It should be mentioned that the investigation of the coupling gap effect on WGM resonances will not be presented for the microsphere experiment, but for the microtoroid part in the following section, since the effect on both cavities follows the same rule as we described in the previous section.

2.3.1 Experimental setup

Basic experimental setup

As described in the "Evanescent F-P model", the WGM resonances in a microcavity coupled by a fiber taper are revealed by the taper transmission spectrum, where the Lorentzian dip is the signature of a WGM resonance.

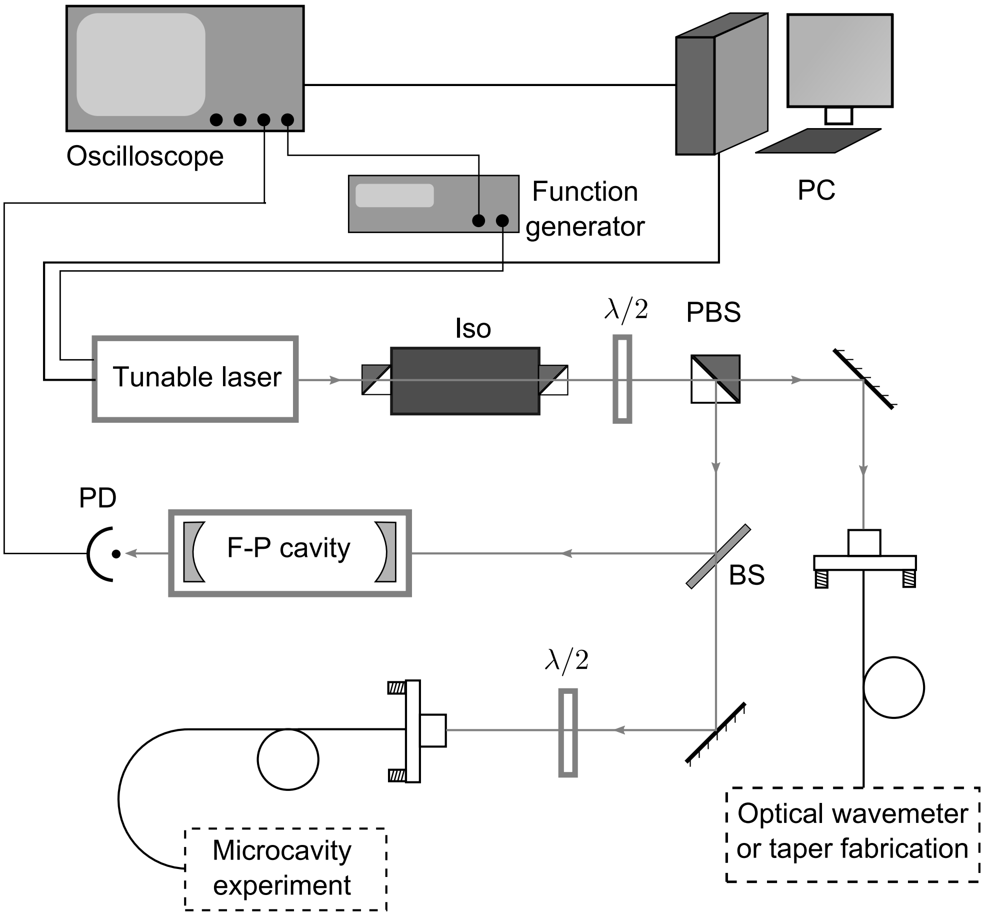

Figure 2.10: Schematic of the setup for the characterization of high Q WGMs. Iso is an optical isolator; BS is a beam splitter and PBS is a polarizing beam splitter; PD is a photodiode detector.

There are several spectroscopy method to record and analyze the transmission spectrum. For instance, one can launch a broadband source (e.g. LED) in a taper and analyze the transmitted signal using a fibre optical spectrometer. This method allows to get quickly an idea of the locations of WGMs in a wide spectrum window, however it is strongly limited in terms of signal and resolution. Considering a typical spectrometer with a resolution about 0.01 nm for operating wavelength 780 nm, the maximum Q-factor that it can measure is on the order of 10^4. To overcome this limitation, the laser spectroscopy is the most common method. In this case, the maximum Q-factor it can resolve is determined by the linewidth of probing laser source. For the highest Q-values, the linewidth of the laser can become limiting and cavity ring-down spectroscopy becomes the most accurate method.

Figure 2.10 illustrates a basic schematic of the setup used to resolve the ultra narrow WGM resonance. The laser source for a passive cavity experiment is an external cavity laser diode (Newfocus TLB6300), which possesses a narrow linewidth of 300 kHz, and a mode-hope-free tuning range of 15 nm. Meanwhile, a triangle wave generated from a function generator allows to finely scan the laser frequency over the selected WGMs. It is also controlled by a computer through a GPIB connection, so that a wide scan can be performed. In order to control the beam polarization, a polarized beam splitter is used to split the laser beam into two separated linear polarized beams. One beam is then coupled into a fiber for taper fabrication or precise wavelength measurement by application of an optical wavemeter. The other beam is coupled to a fiber taper for microcavity experiment. A $\lambda/2$ waveplate inserted before the BPS is used to control the intensity ratio of these two beams.

As shown in figure 2.10, a normal glass sample plate is also used as an optical beam splitter, allowing to send a small fraction of the light into a home made confocal Fabry-Perot cavity (FP). This FP is used as frequency reference, its FSR=$c/4L$ being determined by the designed cavity length L. The transmitted light intensity is measured with a silicon photodiode detector, thus providing a frequency marker for calibration. Finally, the FP signal and the signal transmitted by the taper are displayed on a digital oscilloscope.

Fiber taper coupled microcavity setup

Here the schematic of a fiber taper coupled microsphere system is shown in figure 2.11(a). First, a low loss subwavelength fiber taper is produced by pulling a single-mode(SM) optical fiber heated by a torch as described in section 2.1, and the taper stage is transferred to this setup. It is then fixed on a three-axis translation stage of large tunable range. Second, a silica microsphere is fabricated from a standard SM fiber as described in section 1.2. The microsphere with its holder are mounted on a compact mirror mount combined with a goniometer and a three-axis piezoelectric stage (PZT), so that the two rotational direction shown as two arrows bellow the sphere can be optimized for the best cavity coupling condition. By application of the two translation stages, the microsphere is placed into the evanescent field of the fiber taper. Subsequently, by scanning the tunable laser diode, the taper throughput signal is monitored by the same oscilloscope as shown in figure 2.10.

Also shown in 2.11(b) is the photo of such an experimental setup. A Leica microscope is used to inspect the top view of the sphere and taper, while the side

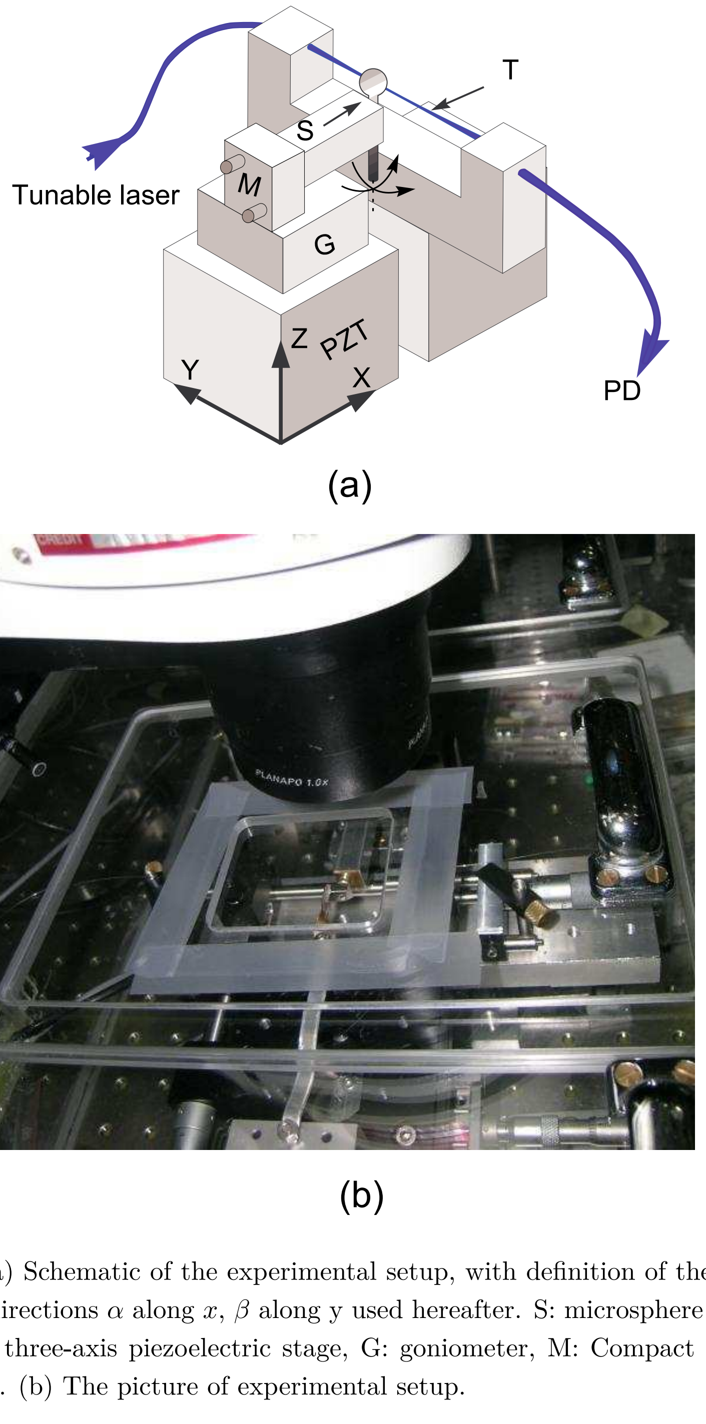

(a)

(b)

Figure 2.11: (a) Schematic of the experimental setup, with definition of the x,y, axes and two rotational directions α along x, β along y used hereafter. S: microsphere (not to scale), T: taper, PZT: three-axis piezoelectric stage, G: goniometer, M: Compact mirror mount, PD: photodiode. (b) The picture of experimental setup.

view can also be detected through a prism. It should be mentioned that this setup is placed in a clean chamber to prevent the contamination of most dust and water in the air. The typical lifetime for a low loss taper is about one week and for a 10^8 Q factor microsphere can be as low as one day, which depends on the opening times. To achieve better life time, one can also fill the chamber with clean and dry gas.

2.3.2 Excitation mapping of WGMs in a microsphere

As described in section 1.1.2, a small ellipticity of the microsphere breaks the spherical symmetry and lifts the degeneracy of the polar modes, thus leading to a huge number of WGM resonances. These modes are characterized by three integer orders n, ℓ, m and their polarization. The radial order n is determined by the number of antinodes of the radial field distribution, which will not be considered here. The orders ℓ and m correspond to a field distribution approximately proportional to the spherical harmonic Y_ℓ^m. Thus an order $q = \ell - |m|$ designates the number of antinodes of the polar field distribution minus one.

Therefore the “fundamental mode” $n = 1$ and $q = 0$, corresponding to a ray tightly bounding close to the equator of the cavity, is characterized by a single antinode along both the polar and radial directions, and achieves the smallest mode volume. Most applications depending on the mode volume can be optimized by selectively working on this mode, which needs to be unambiguously identified.

In the past decades, several approaches have been devoted to this question [77, 78, 79, 80]. In [77], the near-field of a microsphere is imaged on a camera through a coupling prism and a microscope. Refs. [78] and [79] are based on direct detection of the near-field: a fiber tip is scanned along the sphere surface in order to map the evanescent field, for a fixed excitation frequency. In [80], the near-field of weakly confined leaky modes is directly imaged on a camera. The dependance of the coupling efficiency with respect to the mode order that is at the heart of the present work in this section has been used in [81] to filter out high order WGMs of a cm-sized microdisk using an auxiliary coupling prism.

In the following, we will show that near-field mapping can readily been obtained by using the tapered fiber coupler technique as previously described and a widely tunable laser. The near-field distribution is revealed through the spatial dependence of the excitation efficiency. The originality of this method lies in the use of the taper itself, eliminating the need of additional tools used in other approaches. This method can also applied to a microtoroid, for which no simple analytic description exists. It will be described in next section.

Typical transmission spectra

The influence of a small ellipticity as described in equation (1.25), gives the shift of low q order modes. To characterize this effect, we define a “multiplet” as the set of WGMs sharing the same polarization, n and l interference orders. Figure 2.12 shows the sequence of equally spaced lines of a given multiplet as expected from equation (1.25). Thus the ellipticity e can be deduced using equation 1.26, and is about 0.4% in this case. The absence of a resonance at the location pointed by an arrow ascertains the identification of the maximal frequency $q = 0$ WGM, and the subsequent determination of the other q values. Since the $q = 0$ mode has maximal frequency in a multiplet, we also can conclude that such a microsphere is prolate. The “excitation” or “coupling efficiency” is then defined as the relative depth of this transmission dip $C = 1 - T_{\text{res}}/T_0$, where T_0 is the out-of-resonance transmission and $T_{\text{res}} < T_0$ is the on-resonance transmission. Note that C corresponds to $\mathcal{D}$ if $\alpha = 1$ and $g = g_c$, which can not be the case for all the work.

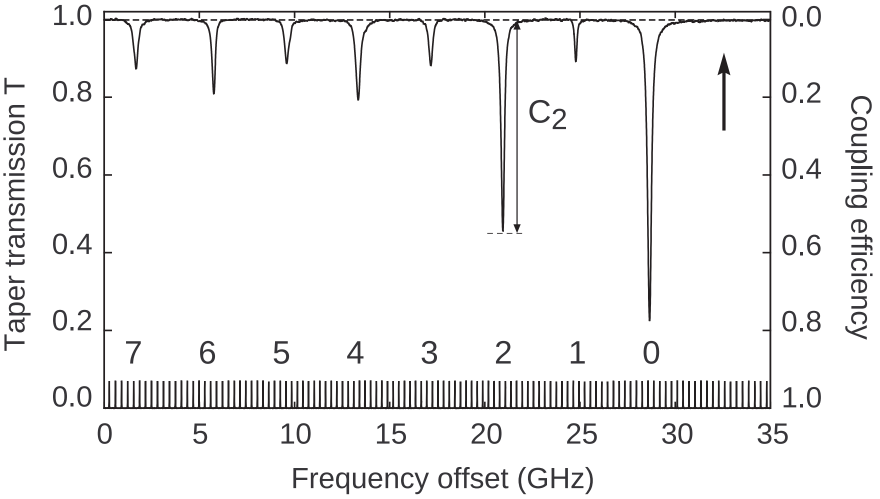

Figure 2.12: Typical taper transmission spectrum for a prolate microsphere of diameter $D \approx 68$ μm and ellipticity $e \approx 0.4\%$. Each line corresponds to the $q = \ell - |m|$ value given below it. The bottom curve is the spectrum of a confocal Fabry-Perot interferometer providing the frequency scale.

A mapping result without optimization

The location of the “absence” can be one approach to identify the fundamental mode of a multiplet. However, this can not work properly, if the high order modes are

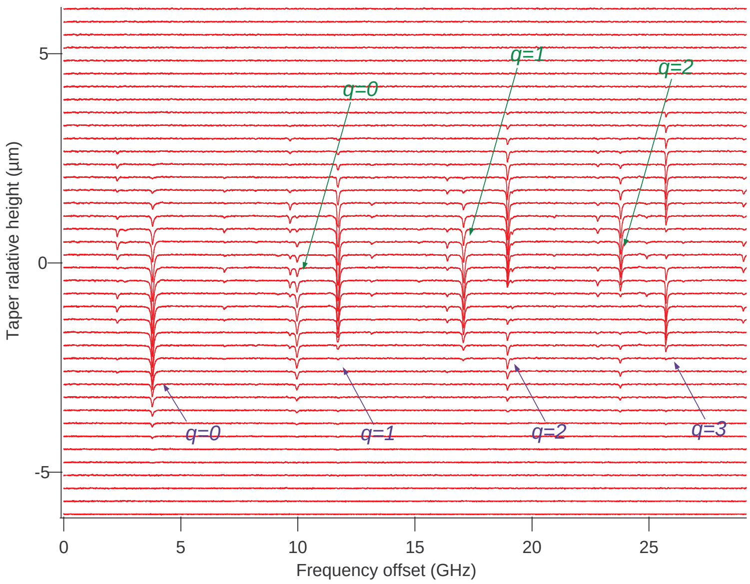

Figure 2.13: Waterfall of successive spectra obtained when scanning the taper along z-position: the curves are horizontally offset by a constant quantity to reflect the z-steps. The antinodes are counted to recognize the fundamental mode of a multiplet. The corresponding q orders are denoted by the arrows. The two different colors designate different families.

more efficiently excited by the taper or there are several families mixing together. Therefore, we develop a mapping method which allows to accurately identify the fundamental mode by using the taper coupler itself.

By moving the microsphere along Z direction using PZT, we observe the oscillations of the coupling efficiency of different modes, which are directly related to their field distributions. To analyze these spectra systematically, we scan the height z of the sphere step by step, with the WGM's transmission spectrum recorded at each step. The resulting spectra are displayed as a waterfall in figure 2.13.

The successive curves are horizontally offset according to the corresponding z value, so that the abscissa corresponds to both the coupling efficiency and the z-coordinates. The overlapping absorption dips allow a clear visualization of the field distribution of the different modes, with $q+1 = \ell - |m| + 1$ antinodes. When reading the diagram, one can see several WGM families with 2 $q = 0$ modes identified, which is also confirmed with the observation of the “absence”. However, the field distribution is so asymmetric, which is due to the fact that the taper is not parallel to the equator of the WGMs. In fact, this also affects the coupling efficiency of the fundamental modes. Thus the rotation angles of the microsphere need to be optimized.

The optimization of WGM equator

Due to the melting process of the microsphere, there is always a slight angle between the geometrical revolution axis and the axis of the stem. Also, the taper is not always parallel to its holder plane. Thus, a goniometer and a compact mirror mount are used in the setup to adjust two rotational angles α and β. For clarity, figure 2.14 gives the schematic of these two angles in both front view and side view. The two arrows bellow the sphere point out the proper rotation direction to correct these two angles. It should be mentioned that in the following we will consider that the taper is scanned, instead of the cavity . The information of these two angles are actually hidden in the oscillations of the dips when scanning a taper vertically along Z axis. First, let us consider the angle α. According to the field distribution of the WGMs, $\alpha = 0$ means that there is a value of z for the taper, where the coupling efficiency C_q of even q order modes reaches their maximum while that for odd q order modes is *zero*. Therefore, we can tune the goniometer in two opposite directions, and compare each values of C_q for odd q modes when taper is in the position where $C_{q=0}$ reaches its maximum. Then the proper direction can be found.

After correcting the angle α, we can now adjusting β using the mirror mount M. The approach to do this is much easier compared with the alignment of α. Figure 2.15(a) and (b) sketched the two conditions for adjustment of β. In the case of $q = 2$, when the taper is scanned vertically, the oscillation of the $C_{q=2}$ can be clearly observed with 3 unbalanced peaks. Based on the asymmetric peaks, it is straightforward to deduce the tilted angle direction, and then compensate it.

Mapping result with optimized angles

For example, we have recorded mapping data after correcting α and β shown as a 3D waterfall in figure 2.16 (a), for a sphere of diameter $2a = 56$ µm and ellipticity $e = 0.6\%$. For a detailed analysis of these data we use a simplified expression of the coupling efficiency valid in the thin taper limit, assuming that the overlap integral of the WGM and the coupler fields is simply proportional to the WGM field. In this model, using spherical coordinates (r, θ, ϕ) with origin on the sphere center, the coupling efficiency writes:

$$C_q(r,\theta) = K_q \left|Y_\ell^{\ell-q}(\theta)\right|^2 e^{-2\kappa(r-a)} \gamma_q^{(0)}/\gamma_q^{(\mathrm{L})} \tag{2.29}$$

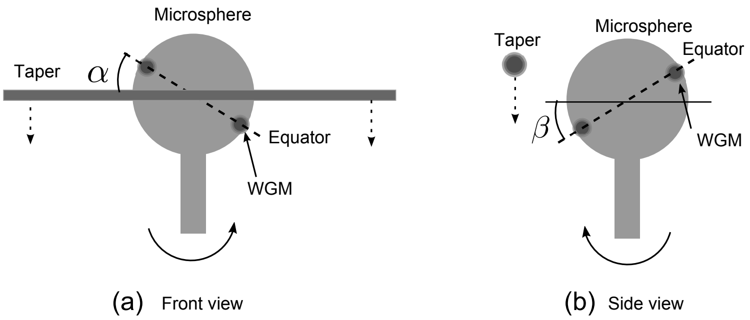

(a) Front view (b) Side view

Figure 2.14: Schematic of the two side views in the taper-sphere system. The dashed line indicates the WGM equator.

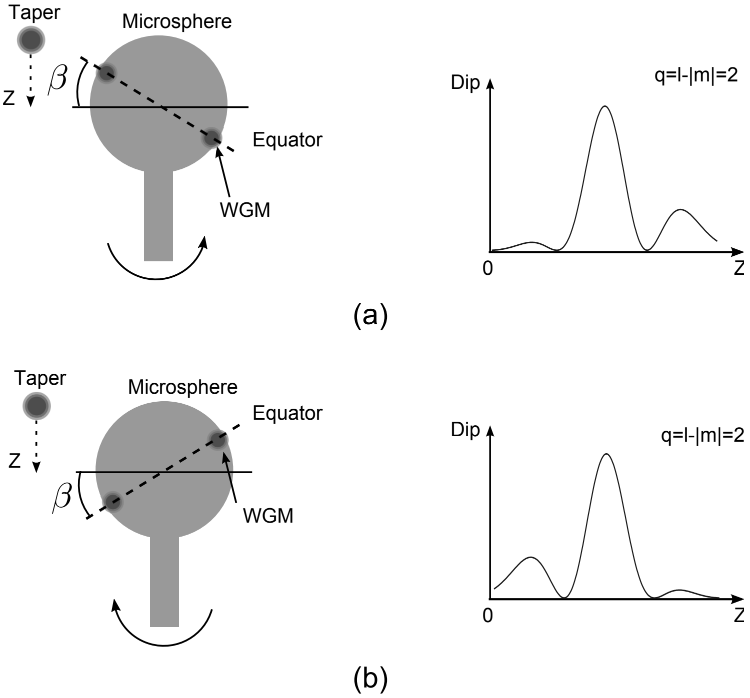

Figure 2.15: Sketch of the two conditions to correct β. The right figures are the schematic of $C_{q=2}$ versus the position z. The arrow below the cavity indicates the rotation direction to compensate β.

where K_q is a scaling coefficient depending on the taper diameter and its effective index, $\gamma_q^{(0)}$ is the intrinsic linewidth and $\gamma_q^{(\mathrm{L})}$ the observed loaded linewidth, κ^{-1} is the evanescent wave characteristic depth. The ratio of the two linewidths allows to take into account the line broadening.

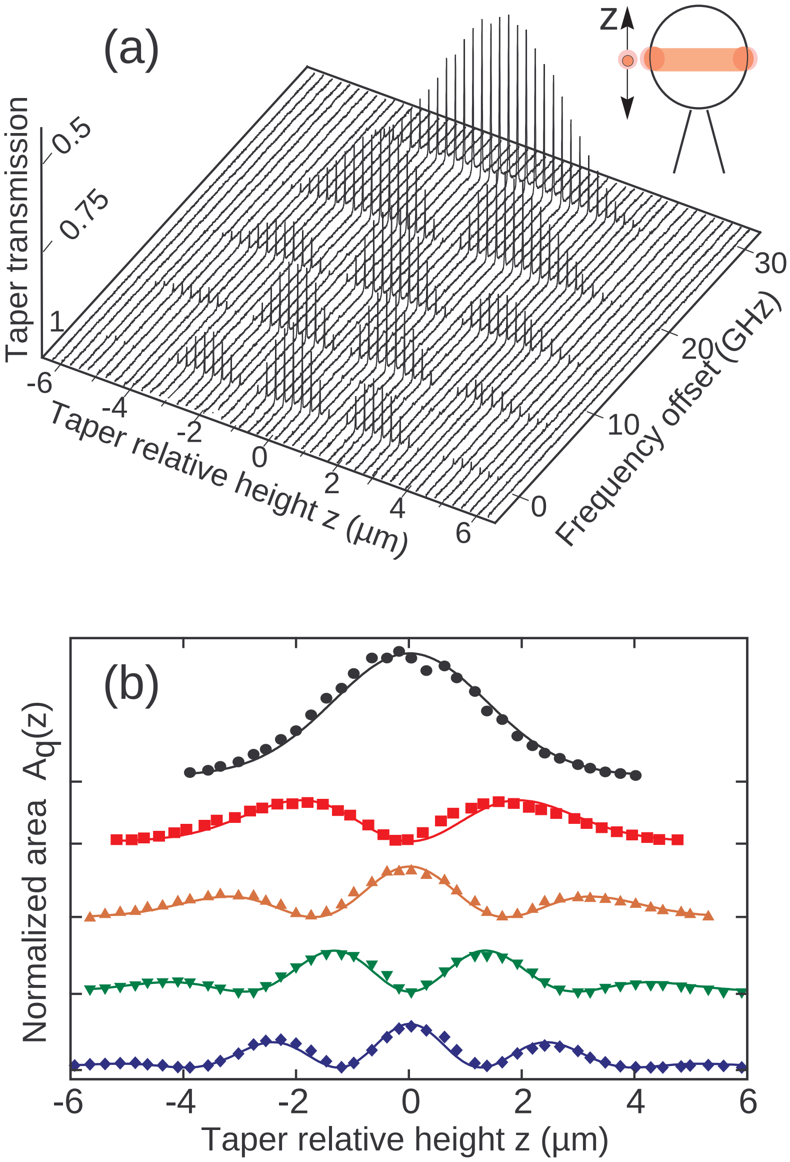

Figure 2.16: (a) 3D-plot of taper transmission spectra for different z-positions; Inset: sphere and taper relative positions. (b) Normalized resonance area for $q = 0 \cdots 4$ as a function of z. Symbols: experimental data; Solid lines:best fit of the data using equation. 2.30.

From the experimental results, we have extracted the coupling efficiency and linewidth of all the resonances, and plotted in figure 2.16 (b) the normalized area of the resonances, defined as $A_q(z) = C_q(z)\gamma_q^{(L)}/\gamma_q^{(0)}(z)$. The data obtained for different q values are offset to evidence the similarity with figure 2.16 (a).

When substituting the spherical harmonic by its Hermite-Gauss asymptotic expression for large ℓ and small q, and using a second order expansion of the gap $g = r - a = g_0 + z^2/2a$, equation (2.29) leads to:

$$A_q(z) \propto H_q^2(\sqrt{\ell}\, z/a)\ \exp[-(\ell + \kappa a)\, z^2/a^2]\ . \tag{2.30}$$

We then perform a global fit on our data according to Eq. 2.30, using different amplitudes but the same horizontal scale for the 5 q values. This fit is plotted as solid lines in figure 2.16 (b) and is in very good agreement with the experimental points, thus proving that our model is accurate and that the measured profiles are actually related to the field distribution. However, the fitted z-scale does not match the expected one but is larger by a factor of about 1.4. This does not come from mechanical effects or from the PZT calibration, but is due to the finite diameter of the taper. It results in an effective z corresponding to the maximum of the fields overlap, smaller than the taper center relative height. This idea is confirmed by a simple numerical simulation of the overlap integral.

To summarize, we have developed a new and robust method to characterize the angular structure of WGMs of a spherical microcavity. Based on the taper used for excitation, it eliminates steric problems arising for other methods. It allows to accurately position the coupling device at the equator location, thus optimizing the coupling to the most confined mode and canceling the coupling to odd-modes.

2.4 Excitation of WGMs in microtoroids

The on-chip silica microtoroids are produced by melting the microdisks with undercuts, as already described in section 1.3. Such microtoroids have been attracting great interest since their first demonstration in 2003[16]. Due to their advantages compared to the microspheres, such as cleaner spectrum, smaller mode volume and compatibility for on-chip integration, they have become highly competitive in most of applications. Unlike microspheres, the fiber taper couplers are up to now the only approach to effectively excite the high Q WGM modes in such cavities.

In the previous work in our group, a neodymium implanted toroid was excited by free space laser beam, and its photoluminescence was collected using a angle polished fiber tip[82]. However, the coupling efficiency of this technique is very low. In the following, we will provide the experimental studies on fiber tapered coupled microtoroids in detail, including the gap effect analysis based on section 2.2.1.2 and the excitation mapping of WGM field distributions using the same method as described in the former section.

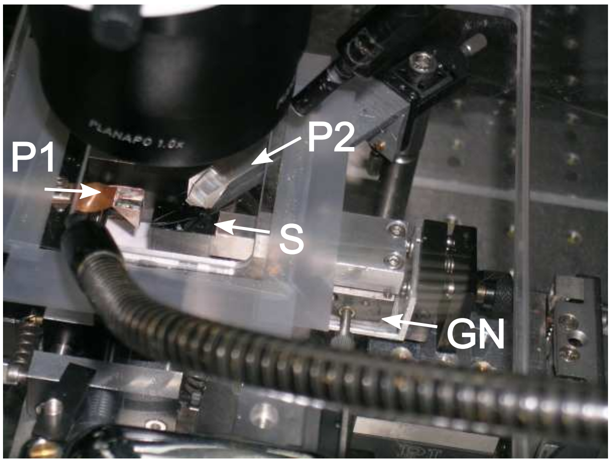

Figure 2.17: The image of the experimental setup. S: the silicon substrate sample; P1 and P2: the sideview prisms; GN: goniometer.

2.4.1 Experimental setup

The basic setup of this experiment is the same as sketched in figure 2.11. Figure 2.17 shows the picture of this setup. The microtoroid samples are placed on a metallic holder mounted on the goniometer. Both prisms P1 and P2 are placed on the side of the sample, and provide a side view to position the fiber taper on the vicinity of the selected microcavity. The goniometer allows one to adjust the angle of the sample plane in order to make it parallel to the taper.

As an example, figure 2.18 is a side view image taken from the prism P2. By adjusting the focus of microscope, one can clearly see that the taper is located in the vicinity of the cavity C2. On these photos, one can see the reflected images of the tapers and of the microdisk (inset).

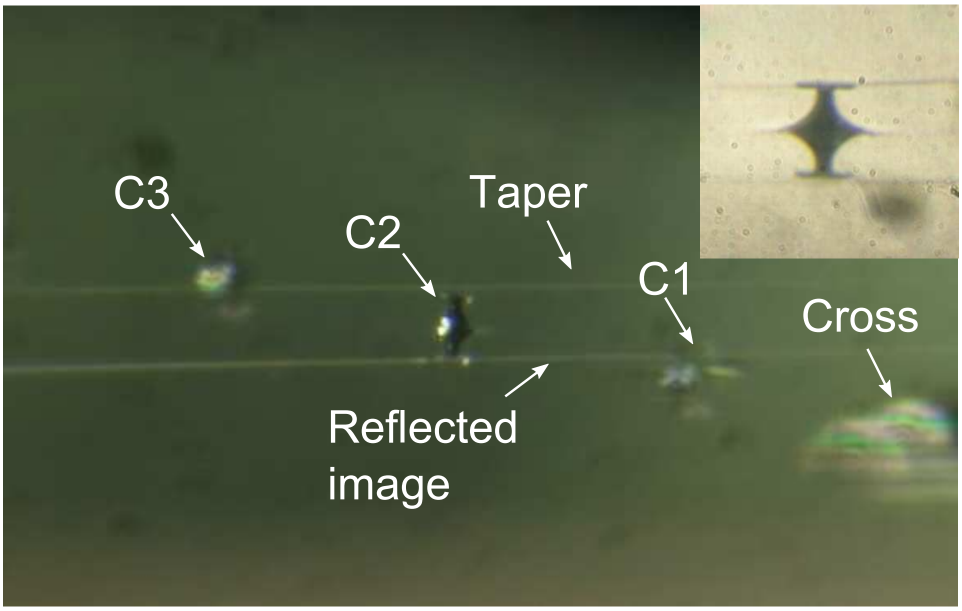

Figure 2.18: A side view image taken from the prism P2, where the arrows represent the taper and the microdisks. Inset: a side view of a microdisk with a larger magnification.

2.4.2 Typical WGM resonance spectra

Q factor of a microdisk

The silica microdisks, fabricated to be used as mother form of the microtoroids are also well-known WGM resonators. Such microdisk structures have been applied to various kinds of semiconductor lasers [83, 84] and more recently for an all-optical flip-flap memory [85]. However, their Q factor is still limited by the surface roughness after production, which is at least 2 or 3 order of magnitude lower than that of a silica microtoroid [86].

The undercut microdisk considered here has a diameter of 59 μm and thickness of 2.7 μm. It stands on a silicon circular pedestal of 22 μm in diameter, as can be seen from the inset of figure 2.18. Before it is melted into a microtoroid, it is first tested by using a fiber taper coupler. Figure 2.19 represents a WGM resonance of this disk. The inset gives the top view of this system, where a white spot in the center of the microdisk results from the reflection on the silicon pedestal. By scanning the laser wavelength around 776.3 nm, a broad WGM resonance is recorded. The solid line is the fit using equation (2.15). The linewidth from the fit is 4.8 GHz, corresponding to a loaded Q of 8×10^4.

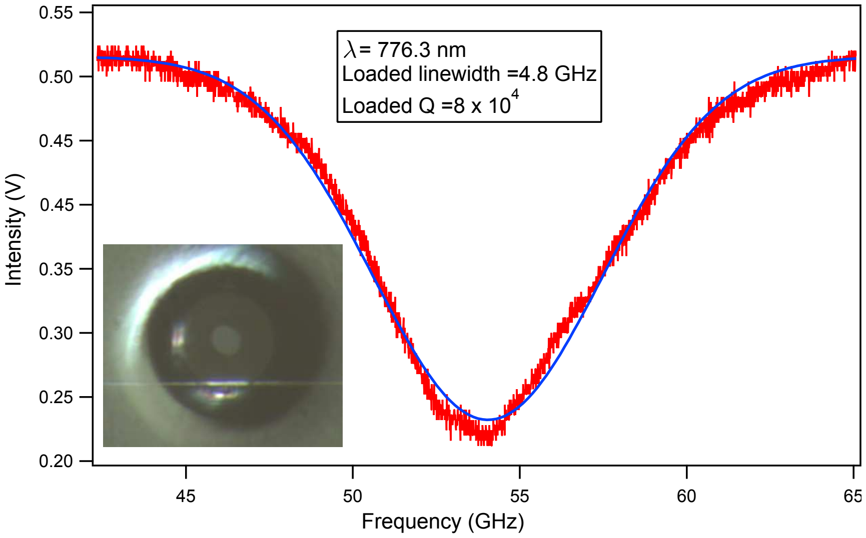

Figure 2.19: A WGM resonance spectrum from a fiber taper coupled microdisk resonator. Inset: a top view of this system.

Q factor of a microtoroid

The selected microdisk is then successively irradiated by a CO_2 laser beam. The induced surface tension acting on the molten material rolls up the edge of the microdisk, leading into a toroidal shape cavity. Details of the fabrication method can be found in section 1.3.2. The resulting microtoroid has an outer diameter of 44 μm and minor diameter of 6.3 μm, as shown previously in figure 1.18 (c) in chapter 1.

The Q-factor of this cavity is measured by monitoring the WGM resonances in the transmission spectrum of a fiber taper coupler. The Newfocus external cavity laser is chosen, because of its good tunability range that is larger than one FSR of this cavity. In general, the calculated FSR is about 3 nm estimated by $\Delta\lambda_{\text{FSR}} = \lambda^2/(\pi N D)$, where N is approximately 1.45, and D is the outer diameter 44 μm. By scanning the excitation wavelength over one FSR, the narrowest resonance corresponding to the best confined WGM mode can be observed. The polarization is controlled by a $\lambda/2$ waveplate. Note that the input probing laser power is controlled below 500 nW so that there is no thermal effect on the monitored resonances. This can be easily checked by looking at the resonance shape on both up and down wavelength scanning directions[2].

---

[2] The value of input power to avoid the thermal effect also depends on the scanning speed, coupling efficiency, Q factor and the other parameters. The thermal effect of a WGM cavity will

Figure 2.20 displays an ultra-high-Q WGM resonance spectrum of this cavity. It shows two sharp resonance peaks, corresponding to the same WGM doublet structure as previously described for microspheres. The inset shows the top view of a taper-coupled microtoroid system. The coupling gap g between the taper and cavity is controlled at about 500 nm in order to be in the under-coupled region. In this case, the measured Q factor can be interpreted as the unloaded intrinsic Q factor of this cavity. Furthermore, the doublet model described in equation 2.28 is then used to fit this result, shown as a solid line in this figure. The well fitting parameter gives the spacing of these two peaks $\Delta\omega/2\pi = 15$ MHz and the linewidth of each peak $\delta\omega/2\pi = 2.6$ MHz. Thereby, the intrinsic Q factor calculated by $Q = \nu/\delta\nu$ is 1.5×10^8. Clearly, the resulting Q factor of this cavity is much higher than the one of its microdisk mother form.

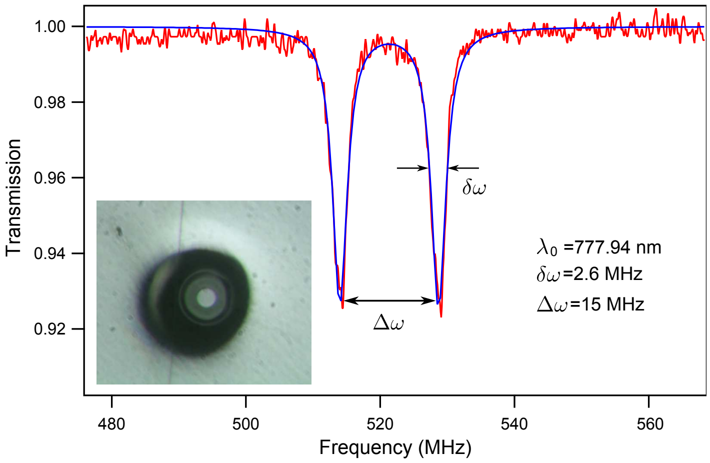

Figure 2.20: A WGM doublet transmission spectrum of a taper coupled silica microtoroid. λ_0 is the center wavelength, $\delta\omega$ is the linewidth of each peak, and $\Delta\omega$ is the spacing between these two peaks. Inset gives the top view of a taper and a microtoroid.

Transmission spectra of toroids with different shapes

Microtoroids support much less WGMs resonances than microspheres due to its reduced volume. Besides the effect of its outer diameter, the minor diameter also plays an important role in the compression of WGM modes. However, this condition is also dependent on the working wavelength. The required minor diameter size for $\lambda = 780$ μm to achieve very clean spectrum is smaller than $\lambda = 1550$ nm. Due to

---

be discussed in the next chapter.

the thickness of our microdisk samples (2.7 μm), the produced microtoroids have a minor diameter in the range of 7 μm. The higher order modes that have lower effective index thus exist in these “thick” toroids. Considering the phase matching condition, a thin taper that also has low effective index can therefore be used to excite these high order modes. Here, a single mode fiber taper of submicrometer diameter was chosen to study the mode structure of these cavities.

Because the very narrow resonance could be missed by a wide range scan, the technique that we used consist in joining successive fine-scan spectra. First, a triangle wave with amplitude of 2 V and repetition rate of 5 Hz is output from a function generator, modulating the piezoelectric transducer(PZT) of the external cavity tunable laser (NF TLB 6300). This provides a fine tuning over a range of 21.45 GHz, and the resulting spectrum displayed on the digital oscilloscope is recorded by a computer. Subsequently, we scan the center wavelength of the laser source step by step by using its stepper motor. For each step, we keep an overlap region that is about 1/3 of the former spectrum, and join them together. It should be mentioned that the cavity is kept in undercoupled region during the measurement and the polarization of input laser is optimized to excite either TE or TM modes.

Figure 2.21(a) shows a broad transmission spectrum from the previously discussed ultra-high Q microtoroid A. The inset is its optical micrograph, where we can see a very symmetric toroid on the silicon pedestal. From the transmission, one can clearly see its rich spectra of WGM resonances. This is because the fact that the 6.4 μm minor diameter permits many high order modes surviving in this cavity around 780 μm, as also discussed in section 1.1.3. The rich spectrum makes it difficult for the location of fundamental modes, nevertheless the mapping technique is very helpful for this purpose, as we will discuss later. Note that several equally spacing modes are labeled with their wavelength positions, measured accurately by using a 0.1 pm resolution home-made wavemeter. The spacing corresponds to one cavity FSR of about 1.42 Thz, which is in good agreement with the expected value.

Also shown in Figure 2.21(b) is another microtoroid cavity B. As we can see from the inset image, this cavity is asymmetric due to the nonconstant minor diameter around its periphery. It likely results from an offset of the center of the CO_2 laser beam with respect to the microdisk center, leading to an asymmetric temperature map during the melting process. However, the resulting spectrum is much cleaner than the former one. This is attributed to its special structure, where the largest minor diameter is about 4.3 μm and the smallest one is about 2.8 μm allowing to filter out the high order modes. However, this structure also induces radiation losses

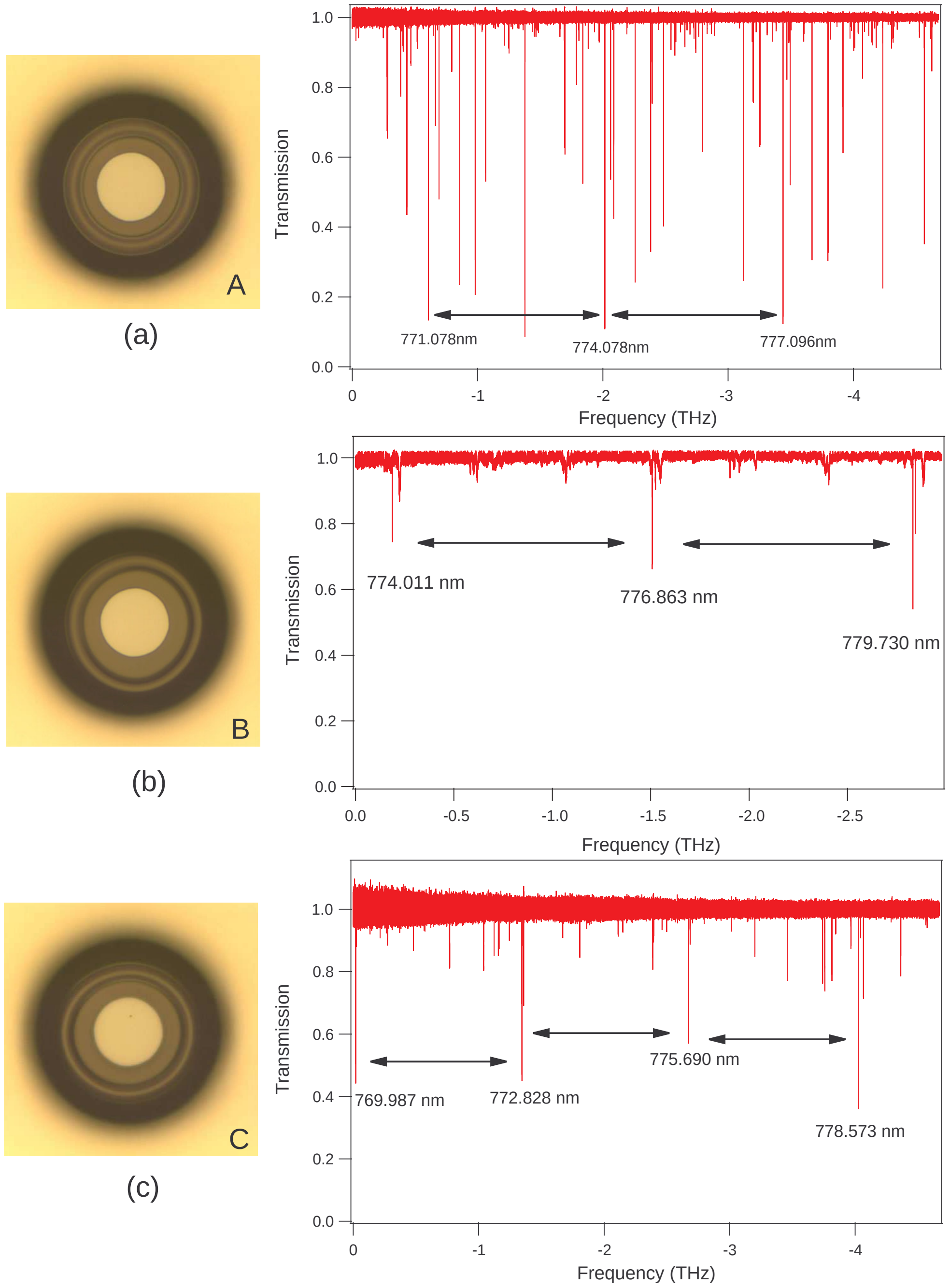

Figure 2.21: Wide transmission spectra of 3 different microtoroids. Inset: the corresponding cavity micrograph taken by 50x optical microscope. (a) Range:$770-780$ nm, FSR: 1.42 THz; (b)$773.7-780.1$ nm, FSR: 1.51 THz; (c)$770-780$ nm, FSR: 1.43 THz.

to low order modes, leading to an obvious reduced Q factor which is on the order of 10^6.

Figure 2.21 (c) shows the transmission spectrum of a less asymmetric toroid C. The minor diameter ranges from about 5.1 μm to 6.1 μm. Surprisingly, the cavity owns a good Q factor as high as 1.6×10^8, while at the same time the mode numbers excited in one FSR is reduced a lot compared to toroid A. The measured FSRs of these cavities are then used to calculate the approximate cavity outer diameter ($D = c/(N\pi FSR)$), which is in good agreement with the measured values using optical microscope. Table 2.1 provides the comparison between calculated and measured values of the diameter.

Microtoroid	FSR	Calculated Diameter	Measured Diameter
A	1.53 Thz	43.6 μm	43.9 ± 0.3 μm
B	1.42 Thz	46.4 μm	45.2 ± 0.3 μm
C	1.43 Thz	46.0 μm	46.5 ± 0.3 μm

Table 2.1: Comparison between calculated and measured values of the diameter.

Finally, we have found another approach for engineering the mode properties of toroidal microcavities instead of simply reducing their minor diameter. This method could be very helpful in the case of shorter working wavelength (in visible or violet region), where reducing the minor diameter becomes very difficult.

2.4.3 The impact of the gap

Like for microspheres, gap effect provides a direct control on the loaded Q factor and coupling efficiency. This is practical in kinds of experiments where the taper and cavity coupling needs to be optimized first. In section 2.2.1.2, we have provided a theoretical model to analyze such effects. Here, we will apply the theory for the global fitting of the experimental data obtained from toroid A and also to confirm the validity of this model. To investigate the impact of the gap, we give a step by step signal to a PZT, which control the gap direction of the taper stage. In each step, a new transmission spectrum is recorded.

Non-doublet modes

The gap effect is first investigated on a non-doublet WGM at 771.1 nm, which has a Q factor of 1.2×10^7. Figure 2.22(a) and (b) are the common plots of the recorded transmission spectra for all the successive gap positions. The color bar labels the gap

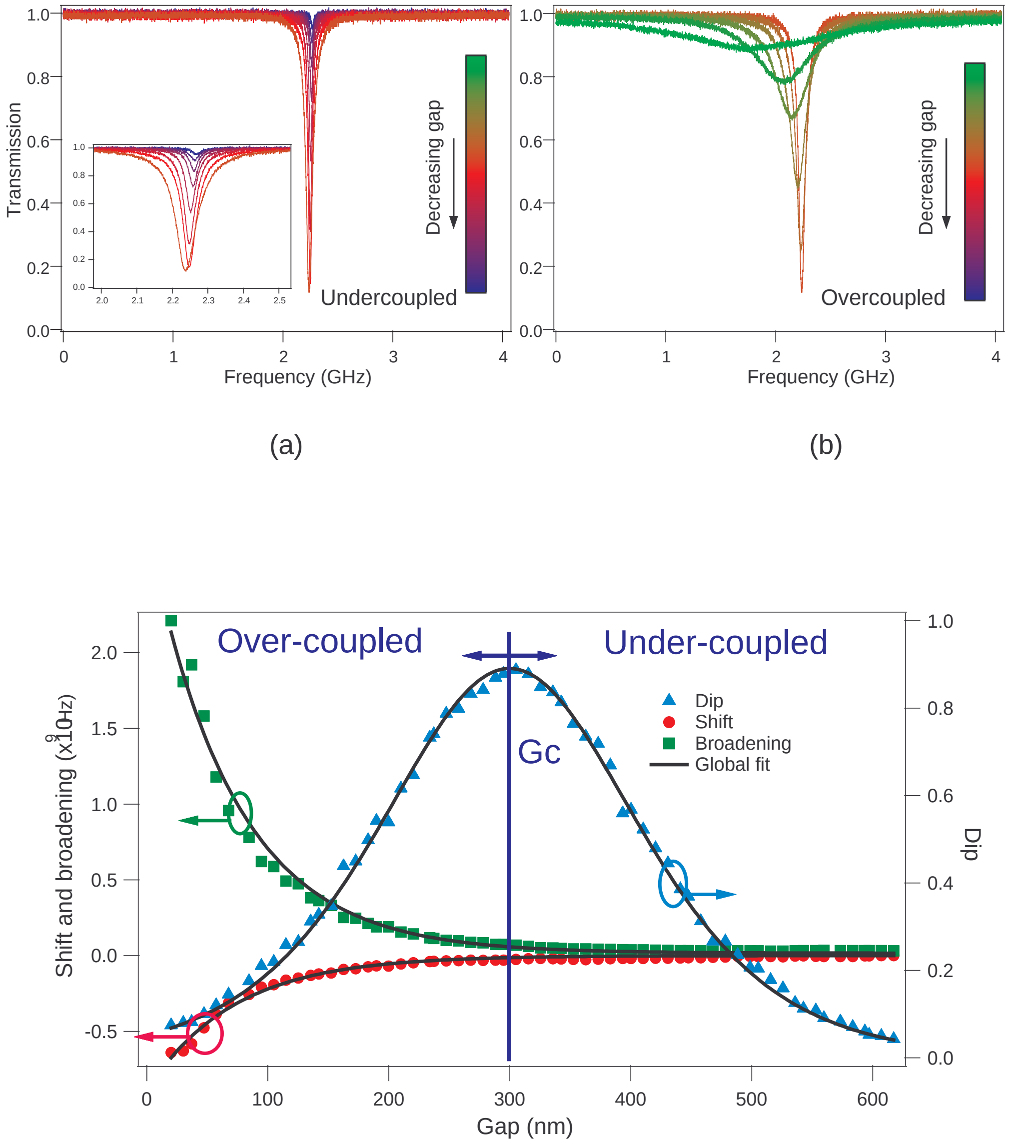

(a)

(b)

(c)

Figure 2.22: The impact of gap on a typical microtoroid WGM resonance at 771.08 nm excited by a fiber taper. (a)(b) selected transmission spectra taken at different gap steps, with a color bar labeling the gap decreasing direction. (c) The coupling efficiency, broadening and shift of this mode as a function of the taper-cavity gap. The solid lines denote a global fit based on the model discussed in section 2.2.

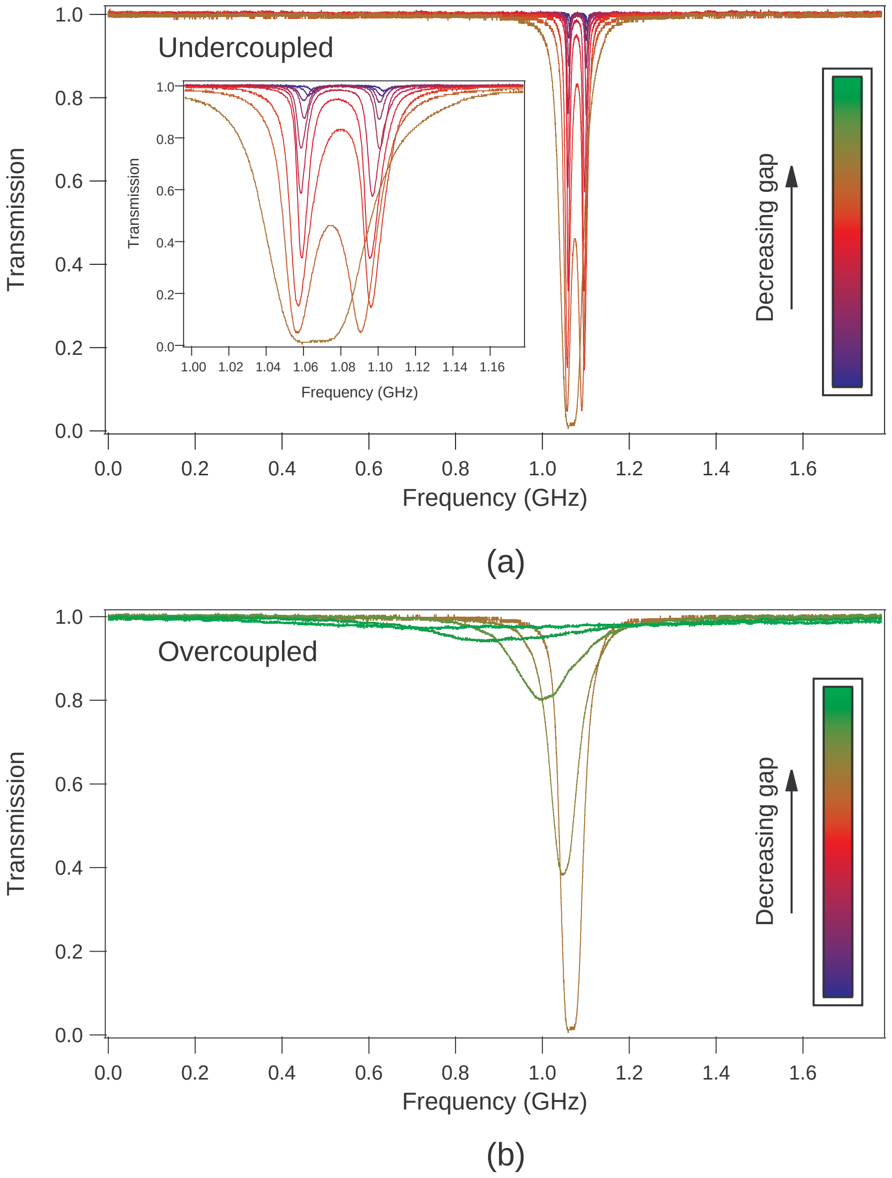

Figure 2.23: The impact of gap on a doublet WGM resonance (microtoroid) at 779.72 nm excited by a fiber taper. (a) Undercoupled region; (b) Overcoupled region.

decreasing direction. Due to the unperfect phase matching condition, the coupling efficiency at critical coupling position $g = g_c$ is only 89%. According to this position, we have separated the spectra into two regions: undercoupled and overcoupled, as shown in figure 2.22(a) and (b), respectively. In undercoupled region, one can observe that the resonance position shifts to shorter frequency and the resonance linewidth increases when the gap is decreasing as expected from section 2.2. These phenomena are more obvious when reaching the overcoupled region.

To analyze these data, we fit each spectrum using equation(2.15) and extract the resonance position, linewidth and coupling efficiency (dip) information. They are then plotted as a function of gap, as shown in figure 2.22 (c). Finally, the theoretical equations (2.21),(2.22) and (2.27), derived in section 2.2, are used to globally fit these curves with a common parameter κ, shown as solid lines. It is worthy mentioned that the ratio of measured linewidth at $g = g_c$ and $g \ll g_c$ is about 2.2 which is very close to the expected value of 2.

High-Q doublet mode

In the case of a doublet WGM, which has a Q factor of 7.8×10^7 and a splitting of 39 MHz, the impact of gap is shown in figure 2.23. From this figure, one can find that the WGM shift and brodening are the same as for a non-doublet mode. However, one can find that the gap effect on the coupling efficiency is different, resulting from the overlap of two degenerate peaks. Nevertheless, due to the contribution of these two components, the coupling efficiency reaches a value as high as 99.5%, which is close to the literally defined critical coupling condition.

2.4.4 Excitation mapping of toroid WGMs

As previously mentioned, a thick toroid can possess a rich WGMs spectrum, requiring better understanding of their mode properties. However, a general analytical theory for their mode structure and resonance positions is not available, in particular because the Helmholtz equation is no longer separable. As a result, the orders n and ℓ no longer exist but m (angular momentum around the revolution axis z) and q (number minus one of polar antinodes) keep their significance. Therefore, an experimental characterization of their field distribution is highly desirable. Our new method as described in section 2.3.2 can conveniently be adapted to monitor this field distribution.

Because of the large curvature of the toroid's minor-diameter, a vertical scanning

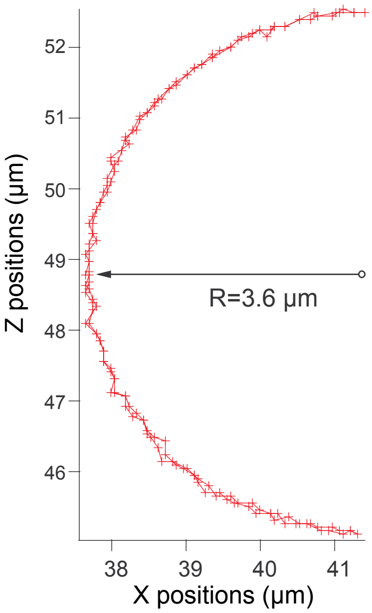

Figure 2.24: The circular scan of the microtoroid

would result in a very large gap, and a vanishing signal. Therefore we have replaced the linear z scanning by a circular θ scanning, intended to keep an almost constant coupling gap (θ is defined in the inset of figure 2.25). We have used the rather thick microtoroid A, in order to observe several modes in a typical frequency range of 30 GHz. The circular motion of the taper is given in figure 2.24. We perform a circular scan with radius of 3.6 μm, corresponding to a constant gap about 400 nm. The scan starts from an estimated equator position $\theta = 0$ to $\theta = \pi/2$, then turns to $\theta = -\pi/2$ position, finally goes back to the original position.

The result of this experiment is shown in figure 2.25. It is plotted as a 3D-plot similar to figure 2.16 (a), the third coordinate being the angle θ, ranging from $-\pi/2$ (below the toroid) to $\pi/2$ (above the toroid). This figure shows several modes with clearly distinct angular intensity distributions, and in particular a fundamental mode $q = 0$ at a frequency offset of about 10 GHz. The WGM in front is mostly localized at large value of θ, with $q \geq 3$. One can notice that the resonances are broader and more pronounced on the left side of the figure because of an imperfect control of the circular motion, leading to a smaller gap on this side than on the opposite one, but this does not prevent the WGMs' characterization.

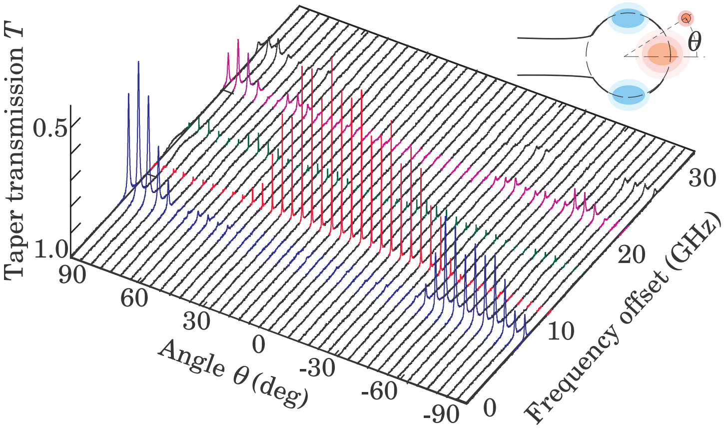

Figure 2.25: 3D-plot of taper transmission spectra for different θ. Inset : definition of θ coordinate.

Chapter 3

Thermal effect-based microlaser characterization

The optical properties of passive silica microspheres and microtoroids have been theoretically and experimentally investigated in the previous chapters. Their ability to store light in small volumes for a very long lifetime leads to the studies on ultra-low threshold lasers.

Another interesting feature of WGM cavities is that they support well behaved modes over a large frequency range, limited only by the transparency of the material. This allows broadband emitters, like those considered in Chapter 4, to automatically find a high-Q mode close to resonance with them. This also enables to launch the pump laser directly in a WGM instead of using, for example, a focused free beam. This ensures not only a nearly perfect overlap between the gain medium and the lasing mode, but also allows to benefit from cavity buildup at the pump wavelength, and finally provides an efficient and accurate way to monitor the absorbed pump power.

When using this "intracavity pumping" scheme, the pump laser frequency is usually locked to a resonance mode, with a variable input power, in order to characterize the laser performance. However, it becomes very difficult when the resonance mode features ultra-high-Q factor or high nonlinear behavior. It comes out that by scanning the pump laser across the resonance instead of the locking technique is more practical [30, 19, 87].

In this chapter, I will show that this approach also provides an original real-time measurement technique for the pump–emission characteristic, relying on the thermal effect. When scanning the pump frequency across the resonance, absorption induces self heating of the cavity, and the resulting thermal drift of the resonance line slows down the power scanning by replacing the sharp Lorentzian dip by a broad asymmetric profile characteristic of thermal bistability. This feature helps us to detect the onset of laser effect on the emitted light.

The detailed study on optical performance of these microlasers will be presented in chapter 4. In this Chapter, a theoretical framework of thermal nonlinear effect in a fiber coupled WGM microcavity is first introduced. Second, the detailed experimental setup and recording method are described. Finally, the laser action is proved and the validity of this method is also confirmed by repeating the result using different scanning speeds including a step-by-step record.

3.1 Thermal bistability

The high circulating light energy built in the high-Q WGM microcavities permits investigation of various nonlinear effects in a very low threshold region, including Kerr bistability [88]. Particularly, the absorption of the circulating light contributes to the warming of the cavity, leading to the thermal expansion and the change of its reflective index. The resulting thermal-optical effects leading to thermal bistability have been widely studied [89, 90]. These effects are normally undesirable for most applications. However, they can be useful in some applications like loss characterization [91]. In this work, it is also used for microlaser characteristic measurement. In the following, we will briefly introduce a theoretical model of the thermal bistability effect.

3.1.1 Theoretical model

Physical constants

The thermal-optical effect obviously depends on the material of microcavities. Here we give those of silica:

Thermal conductivity	κ	1.38		$\mathrm{W.m^{-1}.K^{-1}}$
Specific heat	c_p	740		$\mathrm{J.kg^{-1}.K^{-1}}$
Density	ρ	2.2	$\times 10^3$	$\mathrm{kg.m^{-3}}$
Expansion coefficient	$1/L\, dL/dT$	5.4	$\times 10^{-7}$	$\mathrm{K^{-1}}$
Thermo-optics coeff	dN/dT	1.2	$\times 10^{-5}$	$\mathrm{K^{-1}}$

This gives :

Heat capacity	$C_p = \rho\, c_p$	1.63	$\times 10^6$	W.m^{-3}.K^{-1}
Heat diffusion	$D = \kappa / C_p$	8.5	$\times 10^{-7}$	m^2.s^{-1}

Assuming a sphere diameter of $2a = 66$ μm, and pump wavelength for neodymium $\lambda = 804$ nm, we get :

Frequency	ν_0	3731		GHz
Refraction index	N	1.454		$--$
Size parameter	$x = k\, a$	258		$--$
Angular order	ℓ	362		$--$
Fund. Mode volume	V_m	0.5	$\times 10^3$	μm^3
Sphere volume	V_S	113	$\times 10^3$	μm^3
Sphere heat capacity	$C_S = V_S C_p$	1.8	$\times 10^{-7}$	J.K^{-1}

Time scales

To understand the thermal nonlinearity, three time scales are defined in order of magnitude by:

- *Mode homogenization* : $\tau_m \approx w^2/D = 7$ μs;
- *Sphere homogenization* : $\tau_S \approx a^2/D = 1$ ms;
- *Sphere thermalization* : this time, defined as the time needed to cool the sphere down to equilibrium temperature, is more difficult to estimate. One can first estimate the convective time which likely is the shortest dissipation time:
  - Ilchenko et al. use the Nusselt number [89], which is close to 0.3 for room temperature air. So $\tau_{th} = a^2/(D\mathrm{Nu}) \approx 4$ ms, when using the thermal diffusivity of silica. But the Nusselt number definition implies to use the thermal diffusivity of air $D_{air} \approx 2 \times 10^{-5}$ m^2.s^{-1}, which leads to a value of 0.2 ms which is clearly underestimated.
  - Another approach would be the use of Newton's formula of heat transfer, with a coefficient $h \sim 30$ W.m^{-2}.K^{-1} for air. One then estimates the relaxation times $\tau_{th} = C_S/h\pi a^2 \approx 2$ s, which is obviously overestimated

because it does not correctly take into account the geometry and the air convection.

- A we will see later, this parameter can be measured, and its order of magnitude in our experiment is in the range of 10 ms.

One can also evaluate the conduction time into the stem. Assuming that room temperature is reached in the mother fiber, and a neck of 50 μm in length and 20 μm in diameter, we get a heat resistance of $\mathcal{R} \sim 2.6 \times 10^6$ K.W^{-1}, and a time $\tau_{th} = \mathcal{R} C_S \sim 2$ s.

Thermal frequency changes:

As described in chapter 1, the WGM resonance position of a microsphere can be express as follows:

$$\nu = \frac{f(\ell, n)}{Na} \tag{3.1}$$

where $f(\ell, n)$ is dependent on the radial order n and angular order ℓ, N is the refractive index and a is the sphere radius. This gives:

$$K = \frac{\partial \nu}{\partial T} = \nu\Big(- \frac{1}{N}\frac{\partial N}{\partial T} - \frac{1}{a}\frac{\partial a}{\partial T}\Big) \approx -3.1 \text{ GHz} \cdot \text{K}^{-1} \tag{3.2}$$

where T denotes the temperature. This gives the slope of the resonance shift with respect to temperature. Because the thermal expansion coefficient is much smaller than the thermo-optics coefficient, the main contribution to thermal effect in a silica microsphere comes from refractive index change.

Heating of the sphere:

Consider the fact the power contributing to the heat in a microsphere is simply proportional to the coupling efficiency (or the dip) described in equation (2.17), one can derive the expression of the heat energy transfer into the cavity:

$$P = \eta \mathcal{D} P_{in} = \eta \frac{\gamma_I \gamma_C}{(\omega - \omega_0(T))^2 + ((\gamma_I + \gamma_C)/2)^2} P_{in} \tag{3.3}$$

where η is a phenomenological parameter. It accounts for a possible mode mismatch parameter and also for the fact that not all the dissipated energy is converted to heat. P_{in} is the incoming pump power and $\omega_0(T)$ gives the resonance position, which is dependent on the temperature: $\omega_0(T) = \omega_0 + 2\pi K(T - T_0)$, T_0 being the room temperature.

Thermal evolution:

In the case of a slow evolution where sweeping is at the ms time scale, we have to take into account the frequency (hence time) dependent heating and the thermalization cooling of the sphere and write for $\theta(t)$ the temperature offset $T(t)-T_0$. Considering the energy conservation, the energy change results from heating by the laser and the heat leakage:

$$C\frac{\partial\theta}{\partial t} = \frac{\eta\,\gamma_I\,\gamma_C\,P_{in}}{(\omega(t)-\omega_0-2\pi\,K\theta(t))^2+((\gamma_I+\gamma_C)/2)^2} - \gamma_{th}\,\theta(t) \tag{3.4}$$

where C is the heat capacity, in J/K, of the *effective* heated volume, the size of which depends of the scanning speed, according to the time scales discussed above.

3.1.2 Numerical and experimental results

Equation 3.4 is an ordinary differential equation, which can be solved numerically. This allows to simulate the thermal effect and to calculate both the temperature evolution and the corresponding WGM transmission spectrum. This also allows to fit the experimental spectrum and deduce the temperature curve, as is shown in Fig. 3.1.

This procedure is applied to a typical thermal bistability spectrum recorded from a Nd^{3+}:Gd_2O_3 activated silica microsphere with diameter of 66 μm, shown as a red curve in figure 3.1. The intrinsic linewidth $\gamma_I/2\pi$ measured in undercoupled region at low pump power level is 44 MHz, which corresponds to an intrinsic Q factor of 8.5×10^6 at the wavelength $\lambda = 804.41$ nm. The pump laser is linearly scanned over a small frequency range of about 640 MHz with a 5 Hz repetition rate, and with 5.5 μW input power. Using these parameters in equation 3.4, we perform a fit on the experimental data. As can be seen in figure 3.1, the black solid fit line is in good agreement with the experimental data. At the bottom of figure 3.1 is also shown the cavity temperature response (upper green curve) calculated at the same time as the fitting transmission curve..

The parameters provided by the fit are $\eta/C = 8.17\times10^6$ K/J and $\gamma_{th}/C = 120$ s^{-1}. As η is expected to be close to one, the order of magnitude of C is similar to the heat capacity C_S of the whole sphere calculated in 3.1.1. The deduced thermal time constant τ_{th} in therefore in the range of 10 ms. This value could actually be simply deduced from the exponential relaxation of temperature observed in Figure 3.1 for $t \in [0.075, 0.10]$.

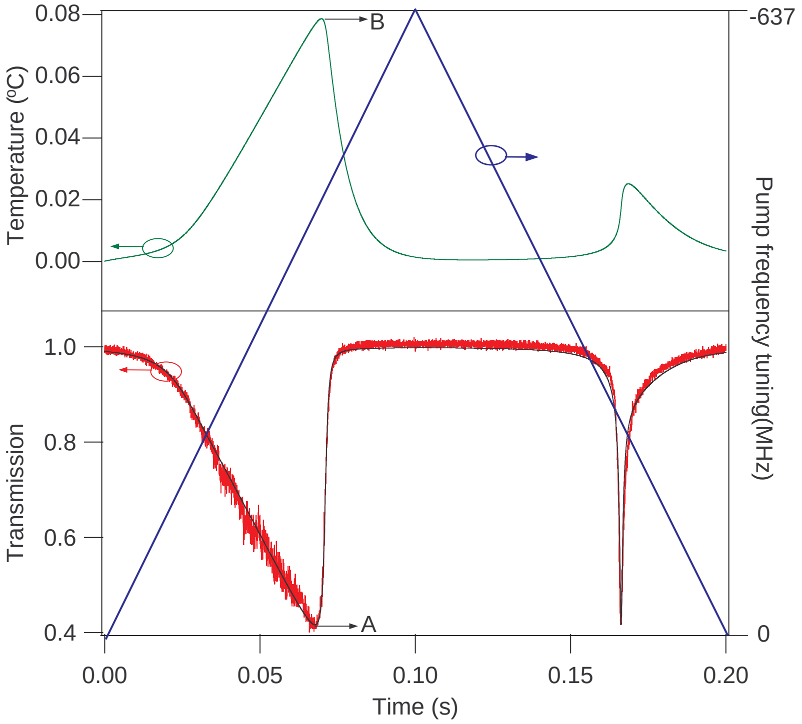

Figure 3.1: Thermal bistability behavior of a taper coupled microsphere system. The lower red curve is an experimental transmission spectrum, while the black solid line is the theoretical fit. The upper green curve corresponds to the calculated cavity temperature as a function of the tuning time. The blue curve then designates the linear tuning frequency of the pump laser. In forward scan: the maximum position of dip and temperature are labeled as A and B, respectively

We now have the elements to further interpret the details of the spectrum shown in Figure 3.1. This spectrum can be split in two parts: forward scan (decreasing frequency) and backward scan. In the forward scan, when the pump laser frequency reaches the vicinity of the WGM resonance, a fraction of the light is coupled into the cavity, then the resulting heating shifts the the resonance center position to lower frequency. This leads to the distortion of the Lorentzian lineshape. There is a position A where the shift of the resonance center is caught up by the tuning laser, it reaches its maximum absorption.

Later the temperature keeps rising to position B, where the heat income is equal to the heat dissipation. After this position B, the dip decrease faster, because the cavity temperature starts decreasing and pulls back the resonance center. It can be seen from the sharp dip side in the figure 3.1. On the other hand, when the laser is scanned backwards to the larger frequency, due to the fact that the heating of the cavity always drift the resonance to the shorter frequency side, the backward scan spectrum gives a narrower resonance compared to cold cavity condition. It also explains the reason why the maximum cavity temperature in backward scan is always smaller than the forward scan.

Here the WGM resonance dip is used to sweep the the pump power injected in the microcavity. Without thermal effect, to observe a weak microlaser signal one would need a detector having simultaneously a high sensitivity and large bandwidth. The thermal nonlinearity helps to solve this problem, since it slows down the power scan, and thus releases the bandwidth condition on the detector.

3.2 Experimental setup and method

In this section, the detailed experimental setup to investigate the laser action of a Nd^{3+} doped microsphere system is described. To acquire the emission spectra with different absorbed pump power, the scanning method is used and a step-by-step method is also worked out to control the pump laser frequency in the vicinity of a WGM and synchronize the acquisition of emission spectra and transmitted pump signal readout.

3.2.1 Experimental setup

Figure 3.2 illustrates the schematic of experimental setup for characterizing a low-threshold fiber-coupled microsphere laser. A free running laser diode (Sanyo DL-8141) of wavelength $\lambda \sim 804$ nm is coupled to the fiber taper and used to excite neodymium ions in the microsphere. At the throughput of the taper, a dichroic mirror allows to separate the remaining pump ($T = 80\%$) and the emitted signal ($R = 99\%$). A silicon detector (PD1) is used to detect the pump signal and display it on the digital oscilloscope.

For a better characterization of the emission properties, a high reflection gold mirror fixed on a kinetic flap mount is employed to conveniently switch between two spectrometers :

Spectrometer A ($f = 0.3$ m): This spectrometer is an ACTON SpectraPro-300i, of 0.3 m focal length, equipped with a 300 gr/mm grating (blazed at 1 μm) and with a 1024×128 pixel thermo-electrically cooled CCD (CCD1). It gives a wavelength resolution of about 0.2 nm and a wide spectrum range of 240 nm. It is mostly used for the studies of photoluminescence spectrum and lasing modes. A RG850 long pass filter is added in front of it to avoid the disturbance due to a fraction of pump signal.

Spectrometer B (f = 1.5 m): The splitting of WGMs in a microsphere due to its small elipticity can not be resolved by the previous spectrometer. For this purpose, a monochromator Jobin-Yvon THR1500 with a resolution of 0.01 nm and a small spectrum range of about 0.5 nm is employed. As shown in figure 3.2, the output beams from THR1500 is split in two beams, that are sent to a high sensitivity silicon camera (CCD2) and to an InGaAs photodetector PD2.

The signals from PD1 and PD2 are then simultaneously monitored by a digital oscilloscope. They are all calibrated to the signal output from the fiber taper for each experiment. Also, the key equipments including pump laser source, spectrometer A, high sensitivity silicon camera and oscilloscope are remotely controlled by a PC or through the NIDAQ 6025 card.

3.2.2 Step-by-step recording method

As previously described, the thermal effect can induce a gentle slope in the vicinity of a WGM resonance dip on its transmission spectrum. In this way, when looking into this resonance dip, the pump power coupled to the cavity change is slowed down. Thus, one expected that the corresponding laser emission action can be well studied by properly scaling the dip power so that it can cover the pump threshold and gradually change the pump frequency towards the resonance center. On the other hand, note the computer can now well communicate with most of the equipments, it is therefore very convenient to control and coordinate them for automatic data acquisition[1]. Compared to the manual operation, this can greatly increase the efficiency and accuracy of data acquisition process.

Figure 3.3 gives the flow chart of this procedure and its corresponding timing diagram. First, a DAC signal generated following $V_n = V_0 + N * Vstep$ is applied to the pump laser current controller in each step, leading to the gradually changed laser frequency. After a waiting time t_1, the trigger pulse is output to trig both the digital oscilloscope and the CCD. This is used to obtain corresponding signals from

---

[1] This can be done by software development (Basic, C, Fortran and so on) or directly use of specialized software like Labview and Igor Pro. In our experiment, the last one is chosen.

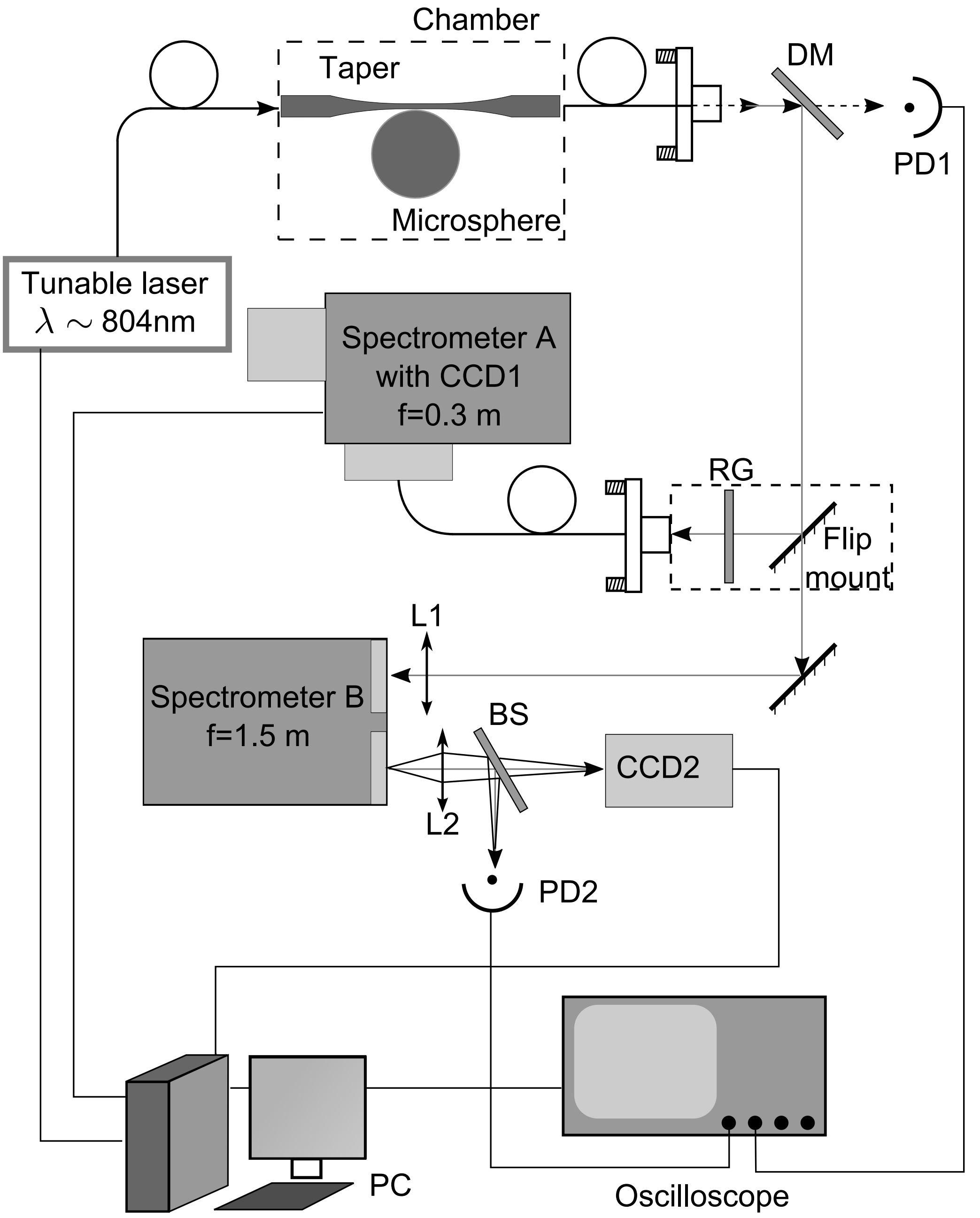

Figure 3.2: Schematic of the experimental setup for microlaser characterization. A free running diode laser ($\lambda \sim 804$ nm) is used as pump source. The pump and microlaser beams in the taper throughput are denoted as dashed line and solid line, respectively. DM: dichroic mirror; RG: 850 nm long pass filter; BS: 50 : 50 beam splitter; PD1: silicon photodetector; PD2: InGaAs photodetector.

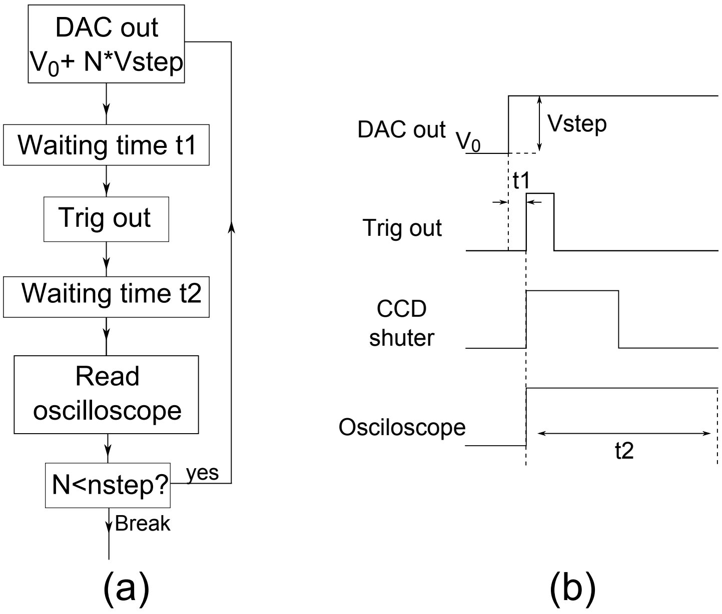

Figure 3.3: (a) Flow chart of the step-by-step data acquisition procedure; (b) The corresponding timing diagram.

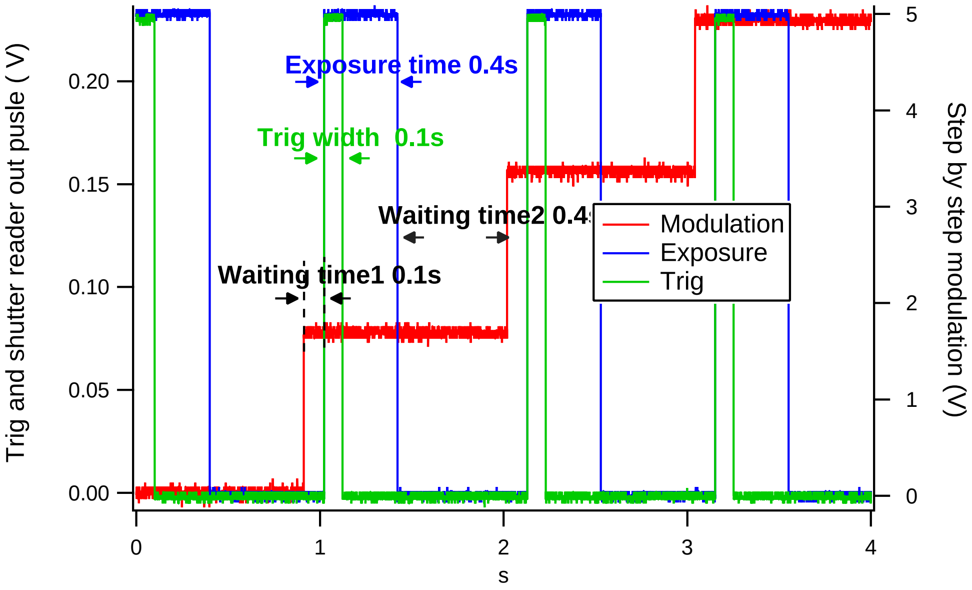

Figure 3.4: A timing sample for the step-by-step data acquisition.

photodetectors on oscilloscope and spectra from CCD. The exposure time of CCD t_{exp} is preset in spectra software (Winview or Winspec). The second waiting time $t_2 > t_{\mathrm{exp}}$ is used to delay the step for CCD exposure and also for the averaging of pump signal (from PD1) and emission signal (from PD2) on oscilloscope.

Also shown in figure 3.4 is the timing sample. The red curve denotes the gradually increasing staircase shaped input signal defining the pump frequency. The blue curve corresponds to the CCD shutter readout, and the green one is the trig pulse. In this figure, one can see the well coordinated signals for each channels.

3.3 Results

The former section has provided detail information about the experimental method and the corresponding setup. In this section, a microsphere laser experiment is carried out. The threshold behavior on the emission spectra is first given using the step-by-step data acquisition, providing the strong evidence of a laser action. Subsequently, a real-time method recording the laser threshold and slope efficiency is presented by scanning the pump laser frequency. By comparing the results obtained using different scanning speeds and the step-by-step record, the validity of this method is confirmed. This method provides a rather efficient way to investigate the ultra-low threshold laser action in such WGM microcavities.

The active microsphere used here is prepared by simply functionalizing a silica microsphere using Nd^{3+}:$\mathrm{Gd_2O_3}$ nanocrystals (more details will be given in the following chapter). The important fact is that such active microspheres still possess ultra-high-Q factors, even at the pump wavelength. They are thus very sensitive to their environment[2]. In order to verify the new characterization method presented in this work, an active microsphere was stored in the clean chamber for a few days to achieve stable lasing conditions. In fact, some of the properties on this sphere was already given in section 3.1.2.

First, the excitation mapping method is used to select low-q order modes for pumping. The pump laser frequency is then scanned in the vicinity of a selected WGM $\lambda = 804.41$ nm. This is done by application of a triangle wave with slow repetition rate 5 Hz on the pump laser controller. The scanning range is typically occupied by the WGM dip with obvious thermal nonlinearity. Subsequently, by

---

[2] The aging problem due to the contamination of dust and water in the air is often observed. A 10^8 Q factor can drop down to 10^7 in several hours depending on its environment condition. Nevertheless, it can stay at 10^7 for several days.

monitoring the spectrometer A, the pump power is adjusted to be able to observe clearly the lasing behavior in the vicinity of threshold. It should be mentioned that the measured cavity Q factor at $\lambda = 804.41$ nm is 8.5×10^6 and Q factor at $\lambda = 1083$ nm is 4.7×10^7.

3.3.1 Evidence of lasing

As previously mentioned, the step-by-step record method has been used here. The pump laser frequency is gradually decreased step-by-step for a range of 563 MHz to cover the selected WGM resonance. At each frequency step, the transmitted pump signal is obtained by averaging the data from oscilloscope and the CCD1 shutter is set on to obtain the emission spectrum. The corresponding averaging time and exposure time are set to 0.4 s. It takes about 50 s to finish 50 data acquisition steps. Figure 3.5 (a) gives the results on the intensity of transmitted pump signal.

In this figure, the base line (empty triangle) representing transmitted pump power without a microsphere is recorded with the coupling gap $g \sim \infty$. Subsequently, the gap is decreased to about 150 nm in order to efficiently excite the resonance mode. The transmission dip distorted due to the thermal effect can be easily observed. Figure 3.5 (b) shows a 3D plot of parts of the spectra as a function of the frequency steps, corresponding to the transmitted pump signal in a rectangle box in (a). As can be seen from this figure, two laser actions occur at different threshold positions (step 18 and 20) for $\lambda = 1088$ nm (A) and 1080 nm (B), respectively.

For further verification, the intensity of emission signals are deduced from the spectra. They are then plotted in Figure 3.6 as a function of absorbed pump power. The absorbed pump power is determined by simply subtracting the transmitted pump signal from the base line in Figure 3.5. The emission intensities are obtained by integrating the spectra (taking into account their background) on 4 nm wide windows, limited by the spectrometer resolution.

The results for the two laser peaks are represented by the red and green curves in Figure 3.6. Moreover, the integrated intensity of photoluminescence signal (PL C) around 1054 nm is also calculated, and plotted with green symbols after magnification by a factor 10 to make it comparable with the lasing signals. The values of threshold pump power for lasing A and lasing B are found to be 450 nW and 600 nW, respectively. One can also find that the PL signals saturates when the laser action starts, which is another important proof of laser action.

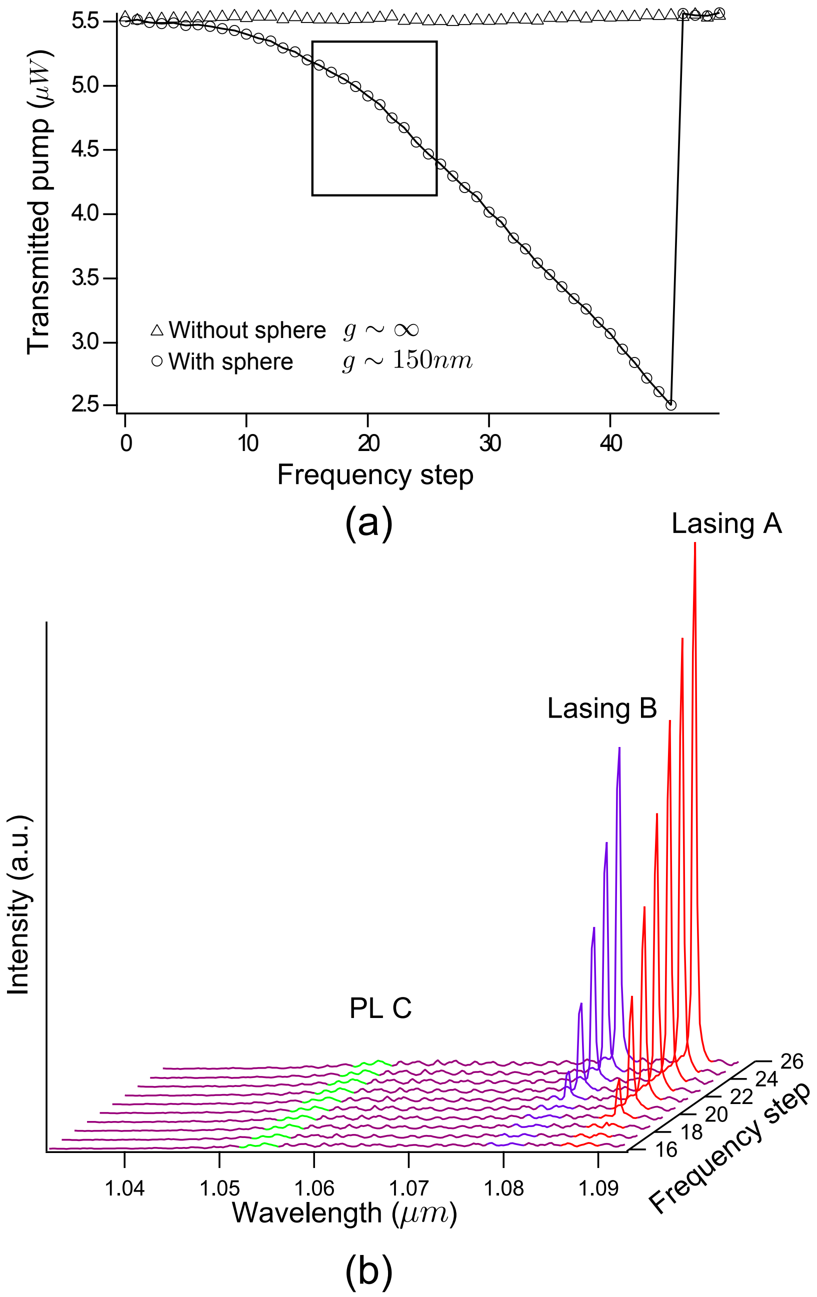

Figure 3.5: (a) Intensity of transmitted pump signal as a function of the frequency steps (PD1). Empty squares and triangles denote the transmitted signal with and without the microsphere, respectively. (b) 3D waterfall plot of the corresponding emission spectra recorded on CCD1. Each spectrum corresponds to a frequency step in the rectangle zone marked in (a).

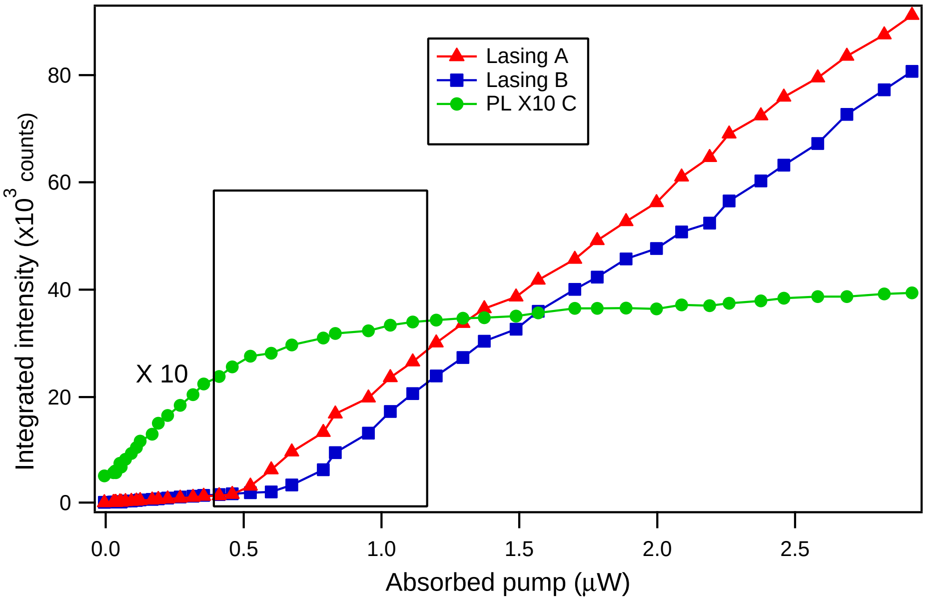

Figure 3.6: Integrated intensity as a function of absorbed pump power. Red denotes the integrated intensity of laser signal A at 1088 nm, blue represents lasing B at 1080 nm and green represents photoluminescence at 1054 nm. The integration range is 4 nm.

3.3.2 Real-time laser characteristic measurement

It has been shown that the use of a WGM resonance dip with nonlinear thermal effect eliminates the need of changing the input pump power, while it still keeps very good results of laser measurement. One expects that the laser measurement can be done very fast by simply scanning the laser frequency at a low repetition rate and simultaneously monitoring its lasing signal, in a method similar to the way industry used in diode laser threshold and slope measurement. Meanwhile, consider the fact that spectrometer A is not able to well resolve the lasing signal and different lasing modes may have different thresholds, spectrometer B is employed to extract lasing A signal to PD2 and CCD2 for further investigations.

Here, a triangle wave at 5 Hz repetition rate is used to scan the pump laser frequency around the WGM resonance over a small frequency range about 637 MHz. This corresponds to a pump frequency scanning speed at 6.37 $\text{GHz} \cdot \text{s}^{-1}$. The simultaneous display of both transmitted pump at PD1 and lasing A at PD2 is shown as the red and blue curves in figure 3.7, respectively. The baseline is also shown by the green curve in this figure. The black curve schematically represents the tuning frequency of the pump laser. A clear threshold behavior can be observed on the

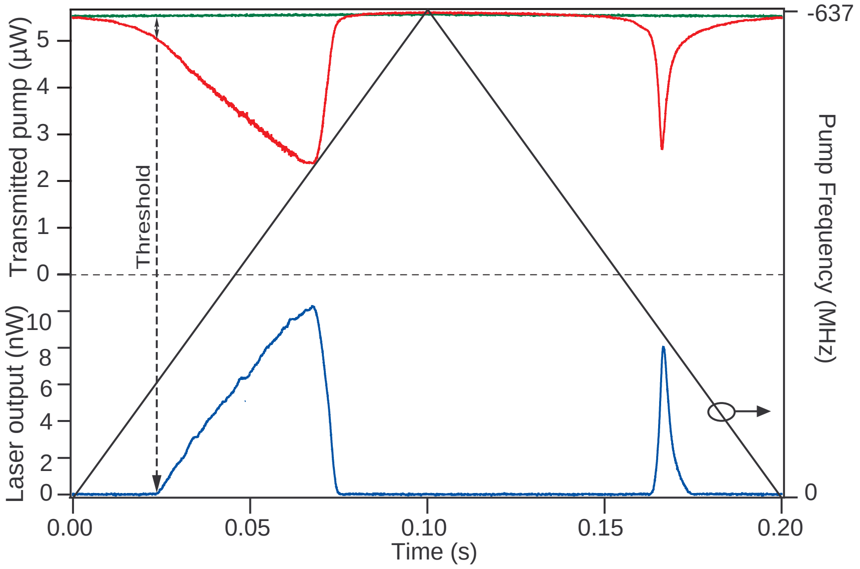

Figure 3.7: Transmitted pump and 1088 nm lasing as a function of time. The upper green curve is the transmitted pump power when the microsphere is far enough, and the lower red curve is the transmitted pump when the gap is about 150 nm. The blue curve is the corresponding laser emission intensity.

emitted signal that is marked with an arrow during the decreasing pump frequency phase.

As discussed in section 3.1, due to the internal heating of the microsphere and the corresponding frequency shift, the rise-time of the coupled pump power is strongly increased, without to broaden the cavity linewidth. This effect is peculiarly interesting in the case of a very narrow linewidth at the pump wavelength. One can then monitor the emitted signal as a function of the absorbed pump power, as it could be done with a XY display on the oscilloscope. We thus obtain in real-time the threshold and slope efficiency of the laser. This enables a fast and efficient optimization.

To further investigate the validity of this method, we also present both the recorded laser signal at PD2 and its spectra in CCD2, using the same technique as previously described. Figure 3.8 (a) gives the recorded transmitted pump power with sphere (black circles), without sphere (black triangles) and the laser signal at PD2 (red triangles). The arrow and rectangle box denote the frequency steps around the threshold. (b) shows the clear laser threshold behavior by plotting the recorded spectra around the threshold pump position. The FWHM of the laser peak

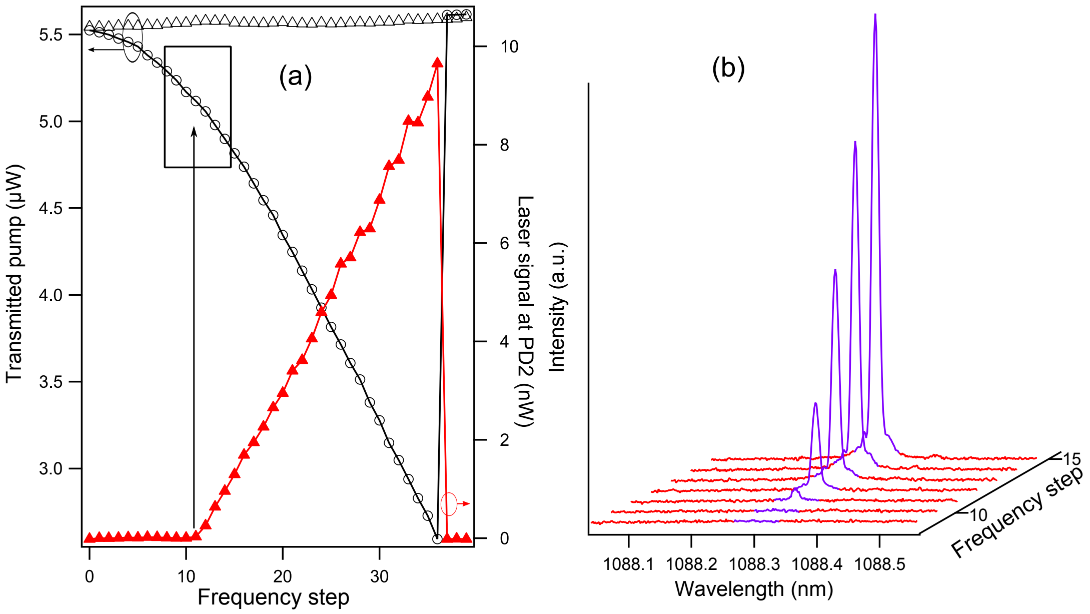

Figure 3.8: (a) The transmitted pump power at PD1 (black) and laser power at PD2 as a function of the frequency steps. (b) a 3D waterfall plot of the emission spectra, corresponding to the frequency steps marked in a rectangle box shown in (a).

is 0.013 nm which is limited by the resolution of spectrometer B.

In addition, the pump laser was also scanned at different rates (1 Hz and 0.5 Hz). In Figure 3.9 we have plotted the laser intensity detected in PD2 as a function of absorbed pump power on PD1, versus the left scale in μW, for the three scanning rates. The almost perfect match of these curves demonstrates that, at these time scales, the “continuous scanning” is quasi-static. It should be mentioned that higher scanning rates provide different results, because of a combined effect of detector bandwidth and of a modified thermal effect dynamics.

In the same figure we have also plotted the two signal obtained by step-by-step scanning, either from PD2 intensity versus left axis, or from integrated spectra from CCD2 versus a conveniently scaled right axis in arbitrary units. The good coincidence of the two step-by-step signals (PD2 and CCD2) strongly supports the validity of this method. His very good consistency with the “continuous scanning” data sets is clearly established by this Figure, and demonstrates the validity of our “real-time” approach.

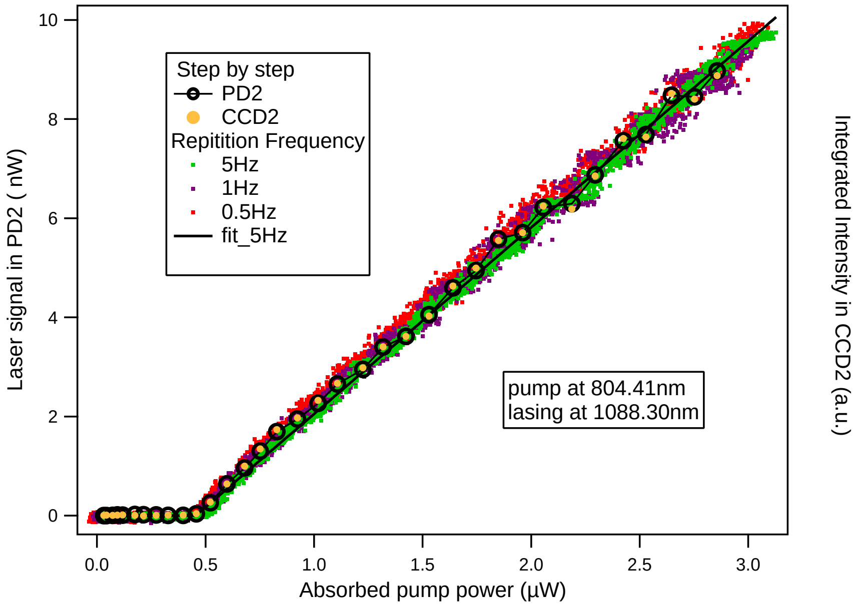

Figure 3.9: Laser signal as a function of absorbed pump power at different repetition rates: 5 Hz (green), 1 Hz (violet) and 0.5 Hz (red). Moreover, the recorded signal from PD2 and CCD2 using step-by-step method are plotted together, shown as black circle and red empty circle, respectively. The linear fit cleanly gives a threshold pump power of 450 nW.

Chapter 4

Nd^{3+}:Gd_2O_3 nanocrystals based silica microsphere lasers

The use of ultra high Q microsphere cavity as a platform to reduce the lasing threshold has been carried out for decades. In 1996, a threshold as low as 200 nW was recorded from a neodymium doped silica microsphere in an inert Argon protective atmosphere [15]. In this chapter, the first laser based on Nd^{3+}:Gd_2O_3 nanocrystals is observed. A detailed study of emission and UV excitation spectra of silica microsphere doped with these nanoemitters gives the proof of neodymium ions in gadolinium oxide matrix. Moreover, we have recorded a laser threshold as low as 40 nW from a 71 μm diameter sphere. To the best of our knowledge, this is the lowest threshold for any rare earth based laser. The slope efficiency is measured as 1%. By increasing the concentration of nanoemitters and using a silica microsphere with a smaller diameter of 41 μm, single mode lasing at 1088 nm is achieved with a threshold pump power of 65 nW and an increased slope efficiency of 7%. The laser performance is then studied using a scanning F-P interferometer. The frequency shift versus absorbed pump power due to thermal effect on the lasing mode is measured, which is about -73 MHz/μW. This well characterized microlaser could have potential applications in biosensor, telecommunication and CQED.

4.1 Photoluminescence in the WGM of a microsphere doped with Nd^{3+}:Gd_2O_3 nanocrystals

With the development of nanotechnology, a wide range of fluorescent nanocrystals exhibiting interesting optical properties have been exploited, mostly as nanoprobes for biolabeling, and for single photon emitters. One consider here their suitability for optical gain and laser materials. Recently, the combination of whispering gallery modes and Nd^{3+}:Gd_2O_3 nanoemitters has provided a convenient way to investigate their optical properties. For example, a first study of photoluminescence from silicon nanocrystals in a microdisk or a microtoroid cavity has been carried out [92, 93]. The coupling of diamond nanocrystals to a silica microsphere has also been investigated [94, 95]. In the case of lanthanide oxide, the gadolinium oxide has a low phonon energy [96, 37], and thus is supposed to have lower non-radiative losses [37]. Moreover, their nanoscale size is of great interest. Since they have a melting point as high as 2420°C, much higher than that of silica which is about 1600°C, one expects that they can be buried just below the surface of silica microspheres by high temperature annealing around the silica melting point. In this section, the WGM photoluminescence from Nd^{3+}:Gd_2O_3 nanocrystals (NCs) is studied.

4.1.1 General properties of Nd^{3+}:Gd_2O_3 nanocrystals

As a popular rare earth material, neodymium ion embedded in laser crystal or glass have been used to produce a wide range of laser products, such as high power 1064 nm lasers for cutting, frequency doubled 532 nm visible lasers. In the past years, neodymium doped gadolinium oxide nanocrystals(Nd^{3+}:Gd_2O_3) have been produced and studied [36]. In our experiments, these nanoemitters are produced by our collaborator, Olivier Tillement and co-workers, at LPCML (Laboratoire de Physico-Chimie des Matériaux Luminescents) in Lyon.

Fabrication

Many techniques have been devoted to prepare rare earth particles at nanometer scale, such as chemical vapor deposition (CVD), laser ablation [97], sol-gel processes [98]. More recently, a polyol method was developed to prepare stable colloids of these nanoparticles[99, 100]. These colloidal nanoparticle suspensions have been mostly used for biolabeling [101]. Besides, they also pave the way to the functionalization of optical devices for sensors, amplifiers and lasers. Here a typical preparation using chlorides as precursors is briefly described. It follows three steps. The first step is dissolution, where the rare-earth chloride $RECL_3 \cdot 6H_2O$ with Nd,Gd is dispersed in diethylene glycol (DEG); The second step is homogenization with the help of a NaOH solution and the last step is vigorous stirring in refluxing diethylene glycol at $180°C$ for 4 hours.

Figure 4.1 gives a typical transmission electron microscopy (TEM) micrograph of Nd^{3+}:Gd_2O_3 nanocrystals, the size of which ranges from 3 to 4 nm. In this work, these nanoemitters in colloidal suspensions are expected to be about 4 nm in diameter and the relative neodymium concentration in Gd_2O_3 is 10%. They are then capped with a 4 nm silica shell grown by so-gel process. To avoid the contamination of other components, pure ethanol is used as the final solvent. The final stable sample has a volume of 1.2 mL, containing 100 micromol 10 % Nd doped Gd_2O_3 nanocrystals, which is rather difficult to concentrate further due to the agglomeration problem.

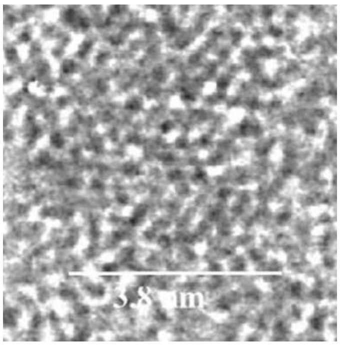

Figure 4.1: Typical TEM micrograph of Nd^{3+}:Gd_2O_3 nanocrystals.

Energy level structure

In Figure 4.2 we recall the energy level diagram of the trivalent neodymium ion, which features a popular four level system. A free running diode laser at ~ 804 nm is used to excite the atoms from its ground state $^4I_{9/2}$ to the upper pump level $^4F_{5/2}$. The atoms then quickly decay into the laser level $^4F_{3/2}$ by a non-radiative process. From this level, there are two radiative transitions ($^4F_{3/2} \longrightarrow {}^4I_{9/2}$ and $^4F_{3/2} \longrightarrow^4 I_{11/2}$). The two resulting emission bands are around 910 nm and 1060 nm, respectively. Consider the fact that the level $^4I_{11/2}$ is quickly depopulated to the ground state by non-radiative transitions, the strongest laser process typically occurs around 1060 nm. It is also expected that the four level system laser features lower threshold pump power.

Sphere doping

Let us first give a brief description of the doping process used in the experiment. Figure 4.3 shows a photograph taken for the coating process. The colloidal suspen-

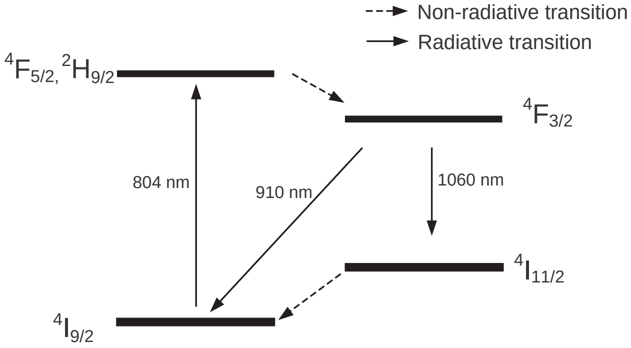

Figure 4.2: Simplified energy level diagram of Nd ions.

sion is stored in a small vessel mounted on a translator. The microscope allows a live view on the dip coating process. First, a silica microsphere is melted at the end of a fiber tip, as marked by an arrow in the figure. Subsequently, the sphere is dipped into the suspension for a few seconds, so that a film about ten nanometers thick is expected to be deposited on the sphere surface. Considering the fact that the depth of a fundamental WGM inside a microsphere is about 1 μm, we remelt the sphere slightly using controlled CO_2 laser irradiation for a few seconds, which helps to anneal the sample and also remove the unwanted solvent and material induced in colloidal suspension production. The laser power is set to a low level so that the sphere is slightly melted without visible reduction of its stem due to over-heating. This can be ensured by looking at the stem of the sphere. One expects that the nanoemitters are therefore buried just below the surface of the silica microsphere, which can result in an optimal coupling between the emitters and a fundamental WGM.

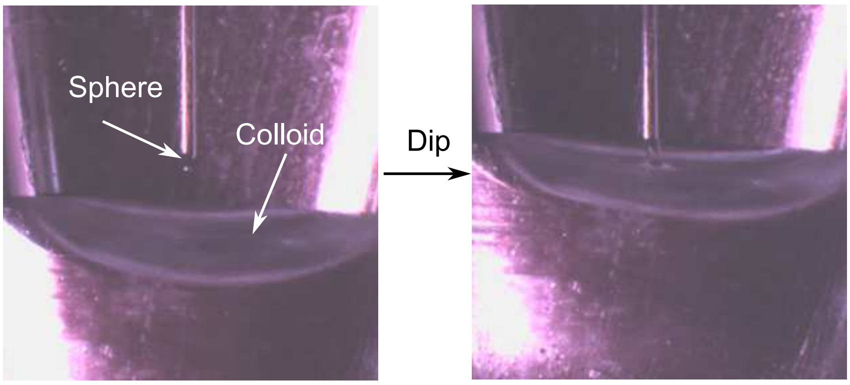

Figure 4.3: Photos of the dip-coating process.

Characterization of a polished sphere

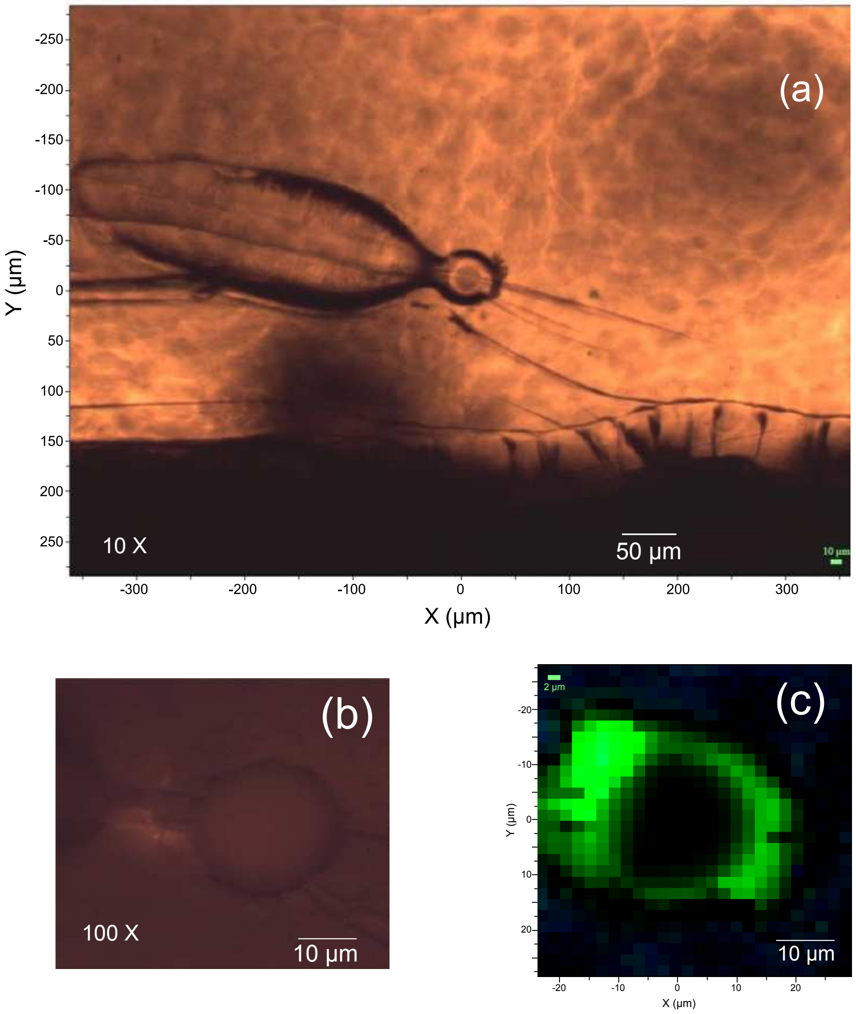

Figure 4.4: Photograph of a side-polished silica microsphere fixed on a resin: (a) X10 objective lens; (b) X100 with focus on the polished face. (c): Photoluminescence mapping image of the Nd ions on the polished face.

To study the distribution of Nd ions in the sphere, we have performed a photoluminescence mapping in the sphere. This process required to eliminate the cavity effect and to have direct access to the ions. For this purpose, our collaborators in Lyon have side-polished several doped microspheres which had been verified to achieve low-threshold lasing. First, a silica microsphere with Nd^{3+}:Gd_2O_3 NCs is fixed in a hard resin. It is then carefully polished so that one side of the sphere is removed, as shown in figure 4.4 (a) and (b). The measured diameter of the sphere and that of the polished region are about 57 μm and 26 μm respectively. Finally, the resulting sample is placed on a Raman microscope (HORIBB Jobin Yvon LabRAM ARAMIS Raman spectrometer). After excitation by 632.5 nm pulse laser source, the luminescence spectra, instead of Raman spectra are recorded. By integrating the emission intensity from the spectra in a range of 800 nm to 1000 nm, a map is computed as shown in figure 4.4 (c), indicating the concentration gradient of neodymium ions upon the sphere surface. Next, the emission and excitation spectra of the sample are studied under continuous excitation by UV irradiation (Xenon lamp), as shown in figure 4.5. The emission spectra recorded with an excitation wavelength of 230 nm and 264 nm give two characteristic emission bands centered at 826 nm and 1084 nm.

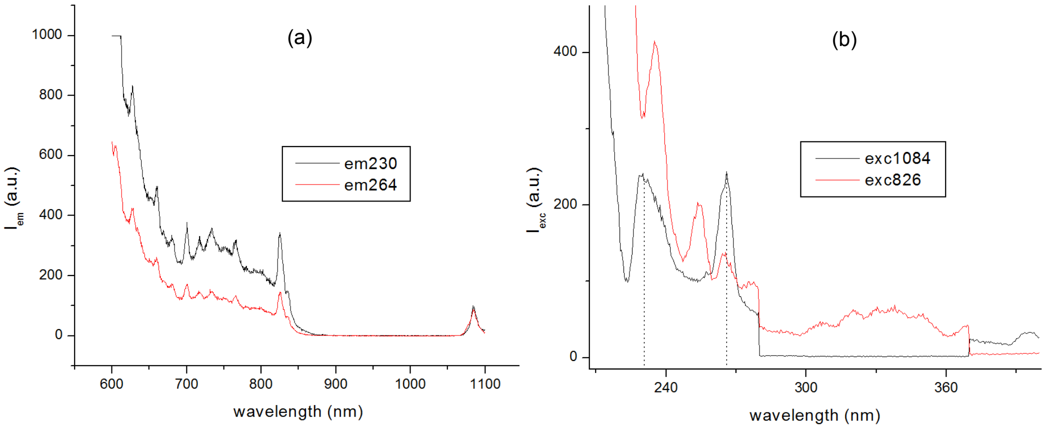

Figure 4.5: (a) Emission spectra under excitation at 230 nm and 264 nm, denoted as black and red respectively. (b): UV Excitation spectra with emission signal detected at constant wavelength $\lambda = 1084$ nm (black curve) and $\lambda = 826$ nm (red curve).

In order to acquire the photoexcitation spectrum in UV region, the detected emission signal is then fixed at $\lambda = 1084$ nm and $\lambda = 826$ nm. Clearly, one finds two excitation peaks centered at 230 nm and 264 nm, which can be attributed to the absorption of gadolinium oxide, because the UV absorption spectrum of neodymium doped silica (also visible on the right part of the spectrum) starts only at about 300 nm[102]. This result confirms that there is some energy transfer from gadolinium to neodymium in this combined oxide. This demonstrates that a significant fraction of the neodymium ions remain in the Gd_2O_3 matrix after the high temperature annealing process. In the low threshold laser measurement, we also find that the single mode lasing wavelength always occurs around 1084 nm, benefitting from

Nd^{3+}:Gd_2O_3 NCs.

Emission spectrum

In the following, we will refer to the two spectrometers alternatively used in this work as spectrometer A (low resolution, wide span, equipped with CCD1) and spectrometer B (high resolution, narrow span, equipped with both PD2 and CCD2), as described in Chapter 3, page 91.

Since ultra-low threshold lasing is achieved from silica microspheres activated by these nanoemitters, it is useful to study first their free space luminescence. To acquire their emission spectra without the influence of WGM resonances, we used a simple setup that is sketched in the inset of figure 4.6. A 5 mW pump laser is sent through the fiber stem on which the sphere has been fused and is still attached. This eliminates the need to manually align the pump laser spot on the microsphere cavity, since the fiber core already strongly confines the light and sends it to the emitters. A two lens setup is then aligned on the side of the sphere to collect the resulting luminescence signal in a multimode fiber. The collected signal after a RG850 long pass filter is sent into spectrometer A. In this experiment, the spectroscopic CCD1 exposure time is set to 40 seconds. The recorded emission spectrum is shown in figure 4.6. The emission bands correspond to the two transitions previously described. It should be noted that the wavelength dependent quantum efficiency of the silicon CCD (CCD QE) has been taken into account for this spectrum.

4.1.2 Photoluminescence in the WGM

The photoluminescence from a microsphere cavity can be collected in the far field by using the two lens system as previously described, or by a taper fiber coupler. In the case of a fiber taper coupler, it plays a role in both ions pumping and emission signal collection. In order to optimize the out coupling of the emitted signal, we chose to use a taper made from Thorlab 980-HP single-mode fiber, with a working wavelength ranging from 980 nm to 1600 nm[1]

---

[1] Of course, this fiber is not single mode for the pump laser, but the higher order modes were likely cut off by the taper.

Broad emission spectrum

First of all, the wide emission spectrum is recorded using spectrometer A [2]. It has been verified that the dichroic mirror with a 99% high reflection for 1080 nm and a high transmission for 808 nm has a non flat reflection curve which affects the detected luminescence envelope around 910 nm. Therefore, only the RG850 long pass filter is used here in order to obtain the correct emission envelope. In our experiment, we once observed that the emission envelope could depend on the sphere-taper coupling gap. This effect can be due to the wavelength-dependent coupling condition that can affect the WGM PL collection efficiency. To minimize this effect, the microsphere is always kept very close to the taper. Moreover, since this overcoupled condition significantly increases the lasing threshold, the PL is collected without any lasing process. The absorption pump power for this PL acquisition is in the sub-microwatt region.

Figure 4.7 shows the PL spectrum of a Nd^{3+}:Gd_2O_3 activated microsphere obtained at room temperature. Two emission bands around 910 nm and 1080 nm represent the main transitions of neodymium ions as already discussed. The emission spectrum features a WGM mode structure of the microsphere, which is characterized by its quasi-periodic structure. As given in the inset, the spacing between two

---

[2] The resolution is 0.1 nm at 435.8 nm for a 1200 g/mm grating.

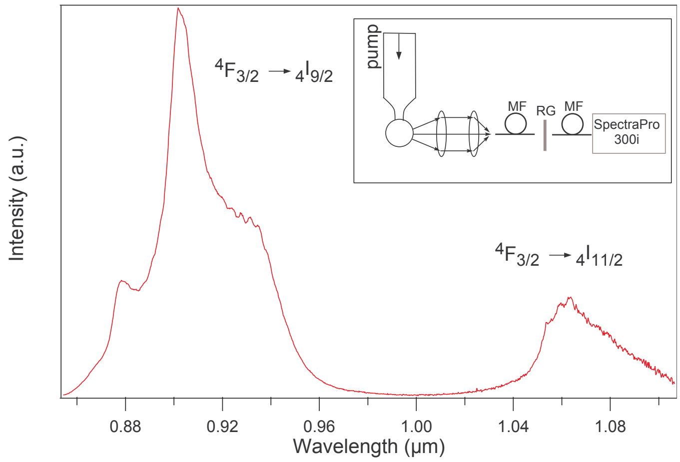

Figure 4.6: Emission spectrum of Nd^{3+}:Gd_2O_3 nanocrystals on a silica microsphere with pump laser coming from its stem (corrected for CCD QE). The two bands around 910 nm and 1060 nm correspond to $^4F_{3/2} \rightarrow^4 I_{9/2}$ and $^4F_{3/2} \rightarrow^4 I_{11/2}$ transitions, respectively . Inset: Schematic of the experimental setup.

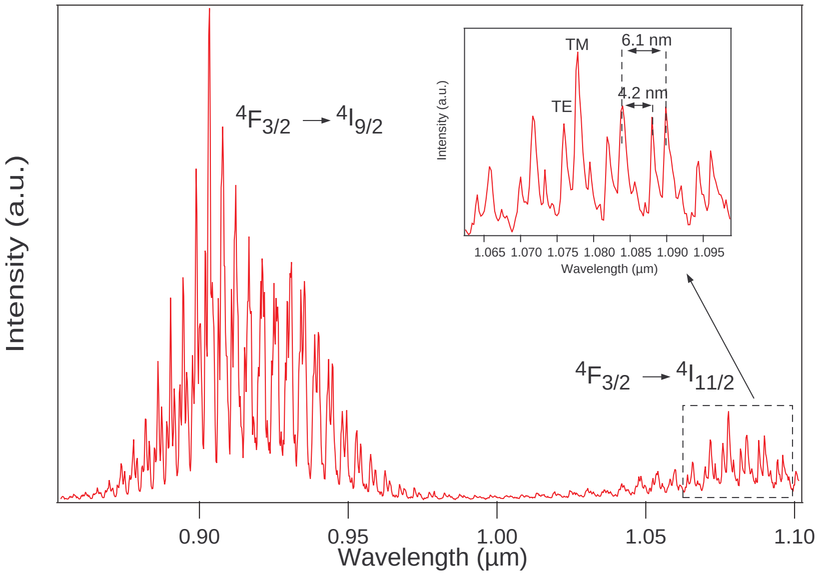

Figure 4.7: Room temperature PL spectrum of Nd^{3+}:Gd_2O_3 nanocrystals from a 41 μm diameter silica microsphere, collected by a fiber taper. The inset shows an expanded region, where the FSR and polarization spacing are indicated.

selected peaks is 6.1 nm. It is in good agreement with the calculated FSR for silica microsphere with diameter of 41 μm at $\lambda \sim 1090$ nm. Meanwhile, one can also observe another small spacing that is about 4.2 nm. It is consistent with the expected spacing between TE and TM polarization which is calculated as 4.3 nm using the formula $\Delta\nu_{TE-TM} \sim 0.7FSR$ given in chapter 1. This agreement ascertains their assigned polarization marked in the figure.

Fine emission spectrum

As described in chapter 2, the fine structure of a WGM family can be studied by probing the cavity with a tunable diode laser. It is also very interesting to investigate this structure in its emission range. Figure 4.8 shows the WGM transmission spectrum of this sphere by scanning the laser around 802 nm over a range of 29 GHz. The q values of two WGMs have been recognized by vertically mapping the cavity. The inter-q splitting (“small FSR”) is measured to be 20.5 GHz, corresponding to an ellipticity of 1.3%.

In the emission range at $\lambda = 1090$ nm, this ellipticity will lead to a splitting of 0.08 nm calculated by multiplying its value with the previously measured FSR.

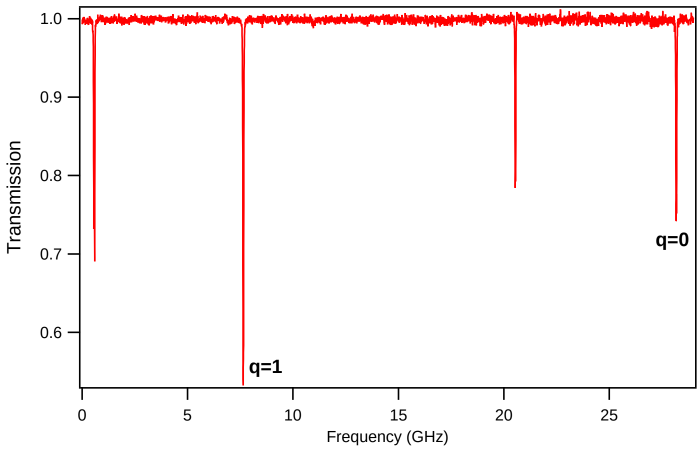

Figure 4.8: Taper transmission spectrum demonstrating the splitting of WGMs due to the small ellipticity f the microsphere.

This splitting cannot be resolved using spectrometer A and we therefore switch to spectrometer B which possesses a 0.015 nm resolution. The corresponding setup has been described in chapter 3. Figure 4.9 gives the emission spectrum recorded around $\lambda = 1090.22$ nm over a range of 0.5 nm. It is obtained from the detected CCD image with 30 s exposure time as shown in the upper part of the figure. The periodicity of these luminescence peaks gives a value consistent with the predicted one. A Lorentzian fit on one of the peaks gives a spectral linewidth of 0.013 nm, which is limited by the spectrometer. The lasing properties of this sphere will be presented in more details in section 4.3.

4.2 Lowest threshold recording

Silica microcavities have been extensively investigated for ultra-low threshold laser. The lowest threshold for continuous rare earth lasers was achieved in our group 14 years ago, with a value of 200 nW. It was based on a silica microsphere, doped in volume with neodymium ions, and excited using the prism coupling technique. In more recent years, fiber taper couplers have been proved to provide a better coupling efficiency to fused silica microspheres or microtoroids [28, 46]. However, the lowest thresholds achieved in these systems are still of the order of a few (tens of) microwatts. In this section, the first laser from Nd^{3+}:Gd_2O_3 nanocrystals is achieved with fused silica microspheres. Moreover, a threshold as low as 40 nW is recorded from a microsphere laser, that is only one fifth of the previous record value.

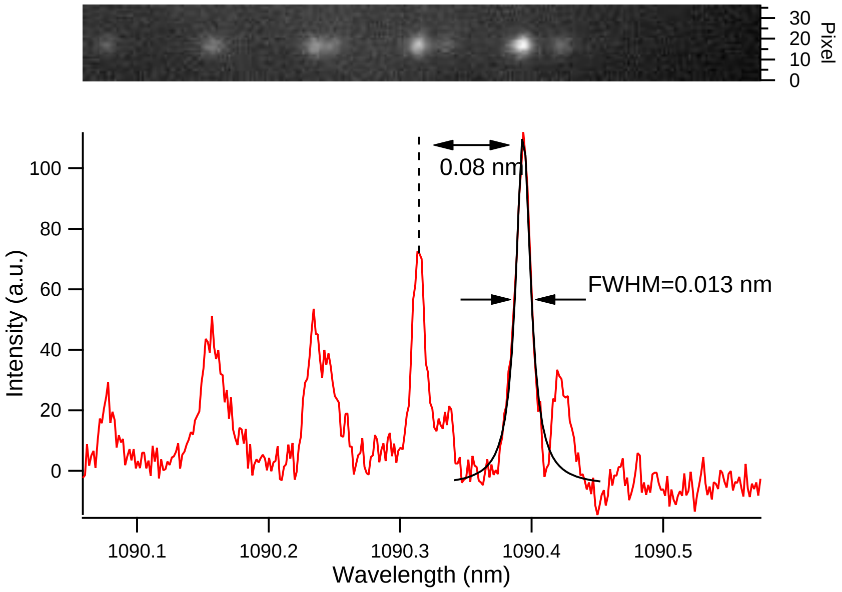

Figure 4.9: The photoluminescence spectrum around $\lambda = 1090$ nm. The black solid curve is a Lorentzian fit. Inset: the detected CCD image.

4.2.1 Q factors

The Q factor of an active microsphere laser must be characterized in two regions: pump wavelength and emission wavelength. Compared to a passive cavity, the former one is also determined by the absorption of the active material (concentration) while the latter one is closer to the passive Q factor, at least for four-level systems like the one considered here. In our experiments, the active microspheres always feature high-Q factors of the order of 10^7 at the pump wavelength ($\lambda \sim 804$ nm) and of 10^8 at the emission wavelength ($\lambda \sim 1083$ nm). The resulting microlasers show very low threshold behavior in the sub-microwatt region. Here, a silica microsphere with a diameter of 71 μm is under study. Its ellipticity is about 0.4% obtained by laser spectroscopy from the WGM splitting spectrum. Using the excitation mapping technology, a fundamental polar mode $q = 0$ is found at 803.29 nm and used to excite the nanoemitters.

Figure 4.10 shows the measured taper transmission spectrum in the undercoupled region for this WGM. The fit of its doublet structure, shown as a solid line, gives a splitting of 5.6 MHz and a linewidth of 3.2 MHz. Surprisingly, unlike the typical Q factor at pump wavelength (of the order of 10^6), the obtained Q factor at pump wavelength is as high as 1.1×10^8. This is likely due to the low concentration of nanoemitters dip-coated on the sphere surface and mostly to the good spherical shape after annealing. Nevertheless, it allows one to investigate the laser performance in the case of such a high build up factor of circulating power in the cavity.

The quality factor at emission wavelength is also studied, as shown in figure 4.11. A DBR diode laser with lasing wavelength at 1083 nm is employed to obtain this spectrum. One may note that this spectrum is much less noisy compared to the one in figure 4.10. Unfortunately, it is because the jitter of the pump laser diode (a conventional F-P laser) is twenty times larger than that of the DBR laser. In this figure, the fit gives a doublet splitting of 6.5 MHz, similar to the one at pump wavelength. The measured linewidth is 1.9 MHz, corresponding to a Q-factor of 1.4×10^8. It should be noted that the DBR laser has a spectral linewidth of about 1.5 MHz, which is nearly equal to the observed resonance width. Therefore, the real Q factor of this cavity is likely higher. Of course, the microlaser linewidth is expected to be much smaller than the cold cavity linewidth at emission wavelength, but we did not measure it.

4.2.2 Power calibration

Here, we introduce the calibration method used in the following experiments. As show in figure 3.2 of the former section, PD1 and PD2 are used for detection of transmitted pump and emitted signal filtered by spectrometer B, respectively. These calibrations are critical in order to be able to specify a threshold value or a slope of the laser characteristics. We chose to define these calibrations as relative to the power which could be measured at the output port of the taper.

For the calibration of the transmitted pump signal at PD1, we first use a power meter to measure the pump power at the taper output, just before the connection of the taper-to-fiber part of the laser measurement setup. The corresponding electrical signal in PD1, after transmission by dichroic mirror (DM) is then calibrated in a way which eliminates the additional losses induced by all the components between the taper and PD1. The “absorbed” pump power is then defined as the product of this power by the dimensionless “dip”. This procedure not only provides a scale but also rules out any possible offset on the origin of this absorbed pump axis. One could suspect that a fraction of the *incoming* pump power which is lost at the output would contribute to pumping. However, this losses are kept below a few percent (2% in the lowest threshold measurement), and they surely occur mostly in the conical part of

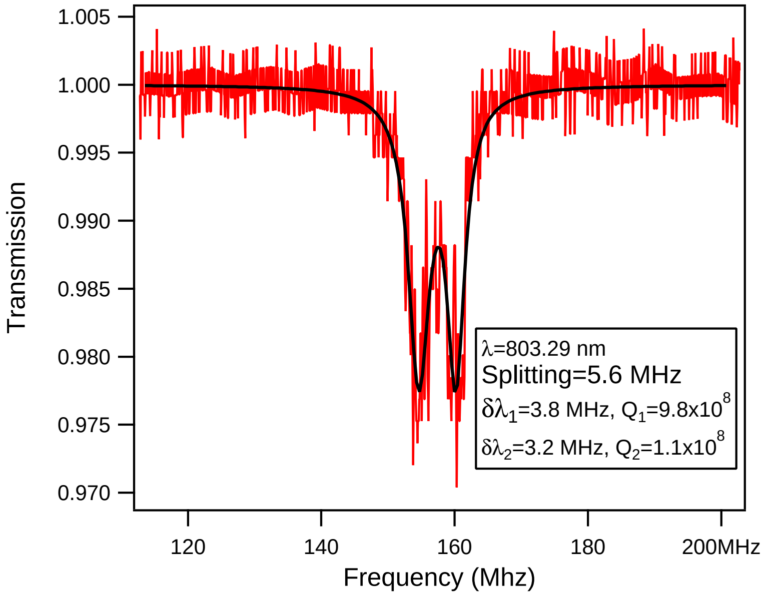

Figure 4.10: Transmission spectrum of the active microsphere around 803.29 nm.

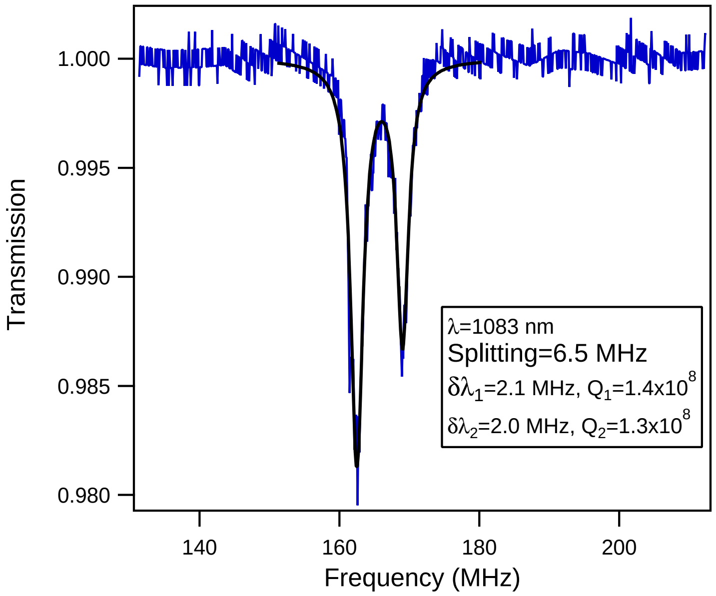

Figure 4.11: Transmission spectrum of the active microsphere around 1083 nm.

the taper, which is far enough to make such a contribution completely negligible. [3]

For the calibration of the emitted signal in PD2, because the coupling efficiency from the taper to the fiber is not reproducible, it must be done at the end of each laser measurement. For this purpose, we first replace the pump laser with the 1083 nm diode laser beam at the taper input port. The electric signal obtained on PD2 is then measured. Subsequently, we remove the taper-to-fiber connection and measure the 1083 nm laser power at taper output. In this way, we calibrate PD2 directly with respect to the taper output port and eliminate all the losses between the taper and PD2, including spectrometer B throughput and PD2 quantum efficiency.

4.2.3 Evidence of lasing

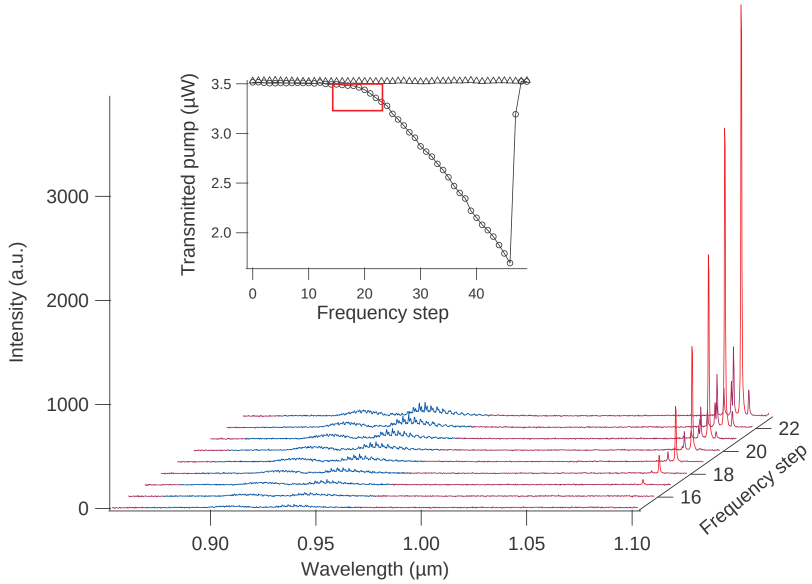

Figure 4.12: 3D waterfall plot of selected emission spectra, demonstrating the onset of laser effect (not corrected for CCD QE). Inset: transmitted pump power recorded with step-by-step scanning of the laser frequency. The upper curve is the baseline measured without sphere.

Based on the experimental setup and laser measurement method described in chapter 3, the onset of sub-microwatt threshold laser action is recorded. During the experiment, the microsphere and taper coupling gap is kept at 200 nm, which

---

[3] Furthermore, if some extra-losses occurred in the coupling zone, this would reduce the *actually* absorbed power, and the measured threshold would be *overestimated*.

corresponds to the undercoupled regime for both the pump and laser signals. Figure 4.12 gives the emission spectra with increasing absorbed pump power, over a range of 240 nm covering the two emission bands of neodymium ions. The inset shows a WGM resonance with thermal nonlinearity recorded step by step. The rectangle zone highlights the region of of the spectra displayed in the 3D waterfall. The absorbed pump power can then be extracted from this figure. A multimode laser action is clearly observed around 1089.5 nm.

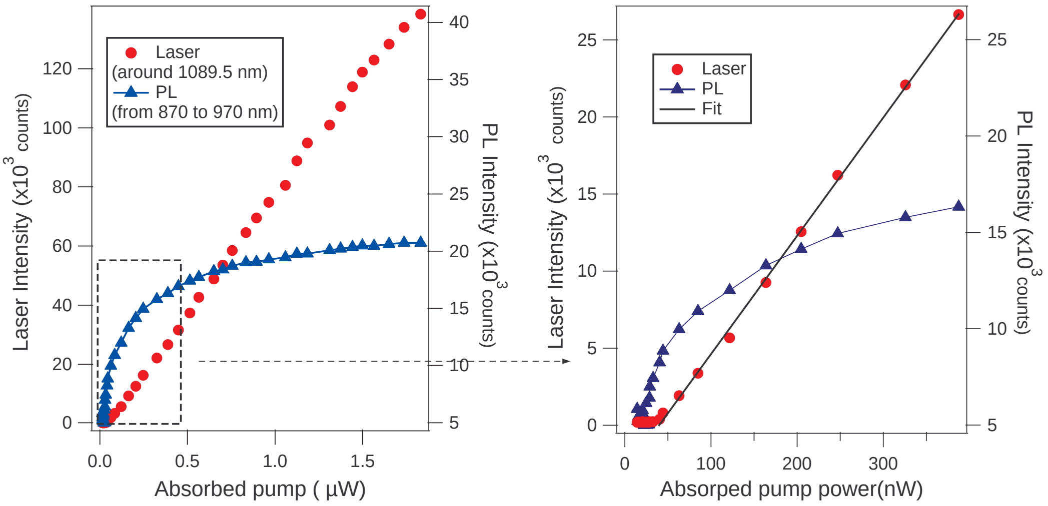

Figure 4.13: Integrated emission intensity of the selected region as a function of the absorbed pump power. The red curve denotes the integrated intensity at laser wavelength $\lambda = 1089.5$ nm, the blue one corresponds to the emission region related to the ${}^4F_{3/2} \longrightarrow {}^4 I_{9/2}$ transition. The figure on the right is an expanded region around the laser threshold highlighted in the left one.

To gain a more quantitative characterization of the laser action, we plotted in figure 4.13 the integrated intensity of both the laser signal and the PL signal detected on CCD2 as a function of absorbed pump power. For the PL, the intensity was integrated over a range from 870 nm to 970 nm, and for the laser signal the integration is performed on a 5 nm-wide range centered at 1089.5 nm. The right-side figure shows an expanded region around the threshold, as highlighted by the rectangle in the left one. As one can see, the luminescence intensity saturates when the laser action starts. All the features corroborate the demonstration of laser action, with a threshold power as low as 40 nW.

4.2.4 Threshold and slope efficiency

In order measure the efficiency of this ultra-low threshold value and to get its slope efficiency, we used the scanning method described in section 3.3.2. The pump laser was scanned across the selected WGM around 803.29 nm with a repetition rate of 5 Hz over a range of 126 MHz, and the transmitted pump power and microlaser output were simultaneously displayed on the oscilloscope. The relevant part, on the decreasing frequency side, is shown in figure 4.14 (a).

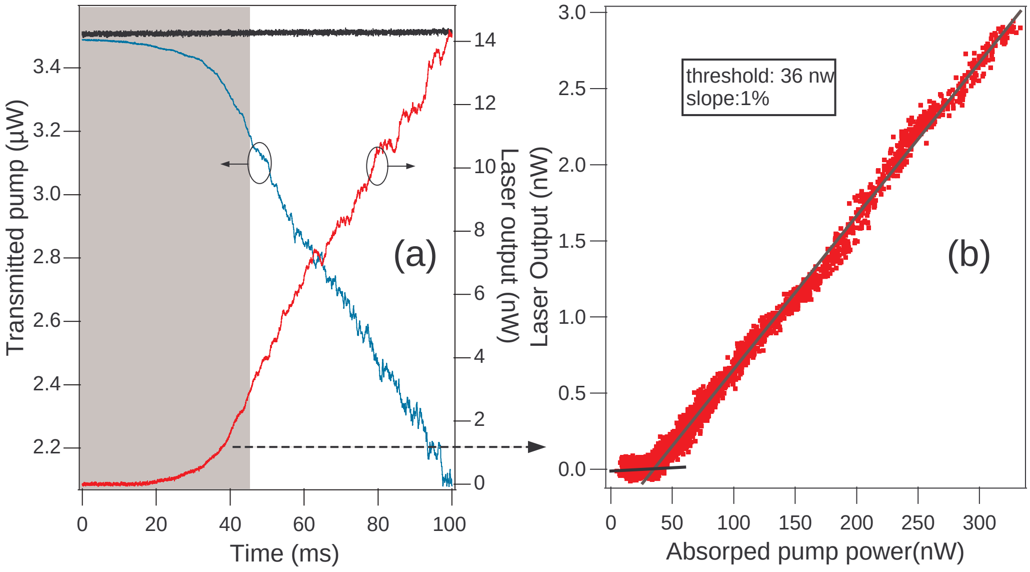

Figure 4.14: (a) The transmitted pump power and lasing signal as a function of time. The upper black curve is the transmitted pump power when the cavity is far enough. The blue one is the part of the resonance dip with nonlinear thermal effect. The red curve is the corresponding laser output signal at 1089 nm; (b)Microlaser output as a function of absorbed pump power in the region highlighted in figure (a). A linear fit denotes a threshold value about 40 nW.

In this figure, the threshold is less visible as compared with the one shown on Figure 3.9 in section 3.3.2. It is because the detected threshold is now one order of magnitude lower than the former one[4]. As the jitter noise in the pump laser limits the accuracy of the measurement, we did not scan on a smaller range to improve the evidence of the threshold. Let us notice that the data plotted here were obtained with averaging function of the oscilloscope enabled.

---

[4] It should be mentioned again that the former microsphere with a threshold about 500 nW was recorded after a few days to achieve a stable condition

Finally, the linear fit of this curve provides a threshold value of $\sim$ 36 nW, which is in satisfactory agreement with the former measurement. The corresponding slope efficiency is about 1%. To the best of our knowledge, this is the lowest threshold ever recorded for any rare earth lasers, and is about one fifth of the former record of 200 nW [15].

4.3 Characterization of a submicro-watt threshold single mode microlaser

In the previous section, we have shown a $Nd^{3+}:Gd_2O_3$ microsphere laser with a threshold as low as 40 nW. The microsphere, having a diameter of 71 μm was still rather "big" and exhibited multimode lasing behavior. Reducing the size of microsphere cavity can result in less dense modes and help to achieve single-mode lasing. In this section, we will present a single-mode laser, with again a submicro-watt threshold, achieved by reducing the diameter of the active microsphere down to 41 μm. The photoluminescence of this sphere has already been analyzed in section 4.1.2. Beside the size reduction, the concentration of nanoemitters was also increased by evaporating the colloidal suspension in the air. This leads to an increased slope efficiency of 7%, with a threshold as low as 65 μW. The detailed characterization of this single-mode microlaser is discussed in the following.

4.3.1 Fundamental polar mode $q = 0$ for pumping

By selectively exciting the fundamental polar modes, one can limit the excited ions to a small volume. By optimizing the fiber-microsphere coupling condition, the competition of possible lasing modes which share these ions would lead to a single mode laser output. As described in section 1.1.2.5, a sphere with a diameter of 18 μm still possesses a Q factor on the order 10^8, which has also been experimentally observed at wavelength $\lambda \sim 770$ nm in our lab. However, due to the limited tunability of the free running pump laser that has a mode hoping every 1 nm and a free mode-hoping tuning range of only 0.2 nm, it was too difficult to find a fundamental mode in such a small sphere that has a large FSR. Fortunately, we have succeeded to locate a fundamental polar mode in a microsphere with a diameter of 41 μm.

Figure 4.15 shows a 2D waterfall plot of taper transmission spectra versus the sphere height. As one can easily observe, two modes that feature only one antinode corresponding to $q = 0$ modes are found in a scanning range of 29 GHz. When exciting these two modes separately, the resulting lasing performances are similar. We then selectively excite the mode located at 801.92 nm to characterize the microsphere laser. This mode features a doublet structure, with a splitting of 20 MHz and a linewidth of 9 MHz corresponding to a Q factor of 4.1×10^7. The decrease of the Q factor compared with the microsphere in section 4.2 is due to the increased concentration of nanoparticle after evaporation.

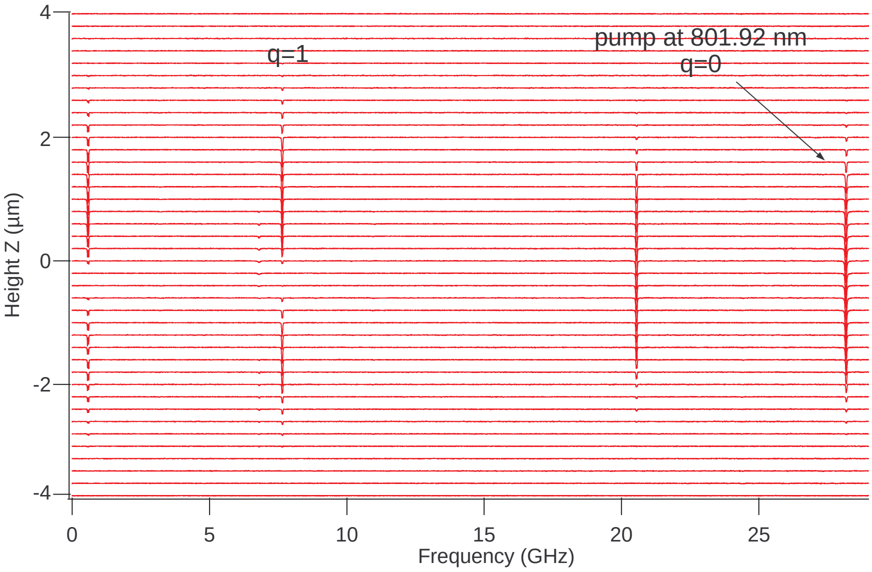

Figure 4.15: 2D waterfall plot of taper transmission spectra for different microsphere relative heights.

4.3.2 Emission spectra and threshold

Figure 4.16 shows a single-mode lasing spectrum of the microsphere functionalized by Nd^{3+}:Gd_2O_3 NCs. The spectrum is measured from spectrometer A covering the two emission bands of neodymium. A single-mode lasing behavior at 1088.2 nm is achieved and evidenced by the red curve. The blue curve is a zoom of this spectrum by a factor of 50. One can clearly see the WGM structure from its PL around 910 nm. The WGM PL below threshold of this sphere has been discussed in section 4.1.2. The inset presents an optical micrograph of the microsphere attached to its fiber stem.

Since the splitting due to a small ellipticity of 1.3% is 0.08 nm for this sphere, the WGMs are not resolved in this spectrum. To further verify its single mode lasing behavior, we used spectrometer B, which has a higher resolution of 0.013 nm. The resulting CCD image is given in the inset (a) of figure 4.17, which shows the the laser spot magnified by a focus lens inserted before the CCD2. For clarity, the PL spectrum below threshold is also presented in the inset (b). The exposure times used for inset (a) and (b) are 0.4 s and 30 s, respectively.

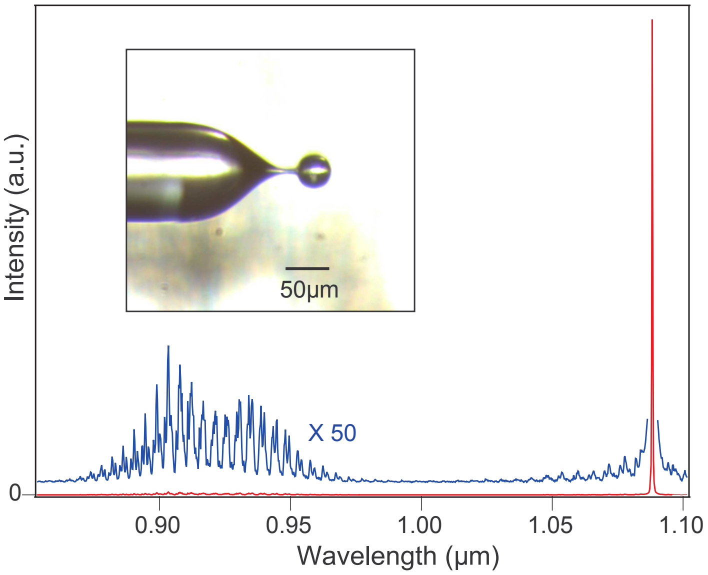

Figure 4.16: Single mode lasing spectrum from Nd^{3+}:Gd_2O_3 NCs functionalized microsphere on CCD1. The upper curve is a zoom on the spectrum, offset for clarity. Inset: optical micrograph of the microsphere

As one can see, due to mode competition, only one mode is lasing. The corresponding lasing spectrum is shown below the insets, which confirms the single-mode lasing action. It should be noted that the lasing wavelength is limited. Therefore the SM lasing wavelength is measured as 1090.3 nm, while it is 1088.2 nm in figure 4.16.

To obtain the lasing characteristic, we use the method of Chapter 3, scanning the pump laser frequency across the selected WGM resonance at 801.92 nm with a repetition rate of 5 Hz over a range of 232 MHz. Figure 4.18 gives the laser output power versus the absorbed pump power obtained from the transmission dip. The taper-sphere gap is here about 200 nm. Above the threshold, the laser output power increases linearly with absorbed pump power. The linear fit shown as a solid line gives a threshold value of 65 nW and a slope efficiency of 7%. A larger slope efficiency compared to the microsphere laser in section 4.2 is expected, resulting from the increased concentration of Nd^{3+}:Gd_2O_3 NCs.

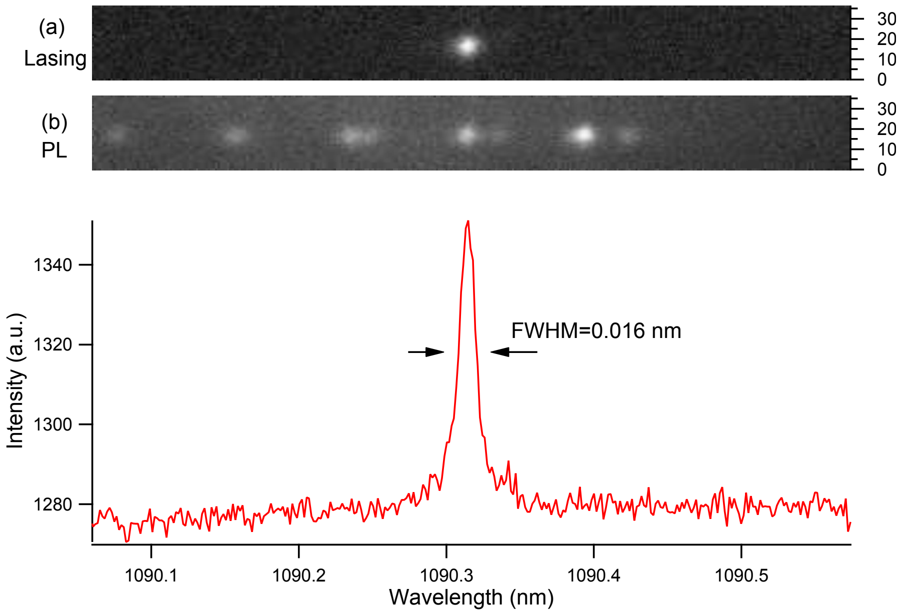

Figure 4.17: Single mode lasing spectrum on CCD2 with finer resolution of 0.013 nm. Inset (a): Emission spectrum above threshold with an exposure time $t = 0.4$ s; Inset (b): Emission spectrum below threshold with an exposure time $t = 30$ s.

The inset of figure 4.18 shows the taper transmission spectrum of the cold microsphere obtained by scanning the probing laser around 1083 nm in the undercoupled regime. The fit on the doublet structure gives a splitting of 6.4 MHz and a spectral linewidth of 1.9 MHz that corresponds to a Q factor of 1.4×10^8. This ultra-high Q factor demonstrates the ultra narrow linewidth of its single mode laser output.

4.3.3 Laser performance vs coupling conditions

The condition to achieve a single mode lasing is critical, depending on several factors such as gain bandwidth, mode density. Literally, it has been mentioned in several papers that changing the coupling condition (taper position relative to the cavity) can lead to a multimode lasing behavior. However, the effect of taper position on the fine lasing spectrum of an active microsphere has not been investigated. Here, such an experiment is carried out to record and analyze this effect.

The pump laser frequency is kept scanning across the selected WGM around 801.92 nm at 5 Hz repetition rate, to excite the nanoemitters. Meanwhile, the piezoelectric stage is controlled to change the height of microsphere step by step. As can be seen in the figure 4.15, a range of 5 μm is selected so that the WGM is always

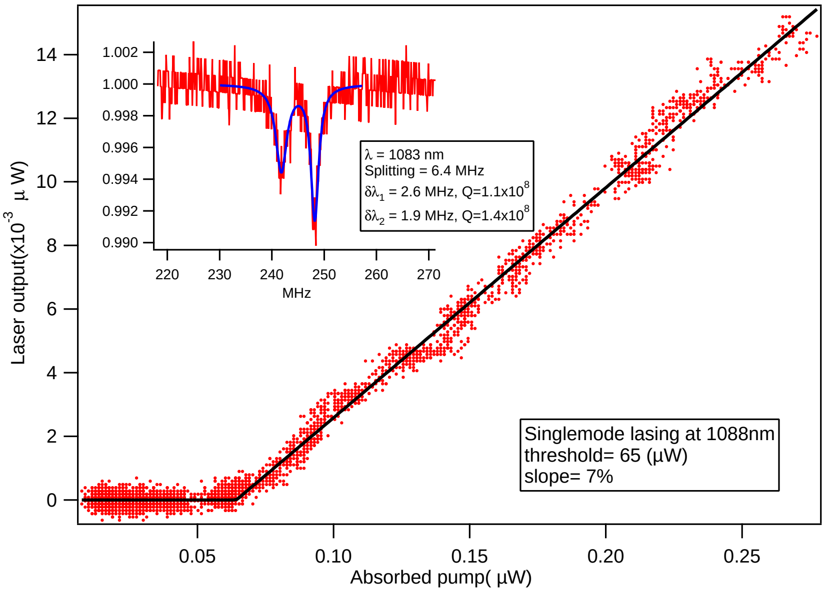

Figure 4.18: Laser output as a function of absorbed pump power in the fiber coupled microsphere system. Inset: Doublet resonance structure of the cold microcavity around 1083 μm.

excited. At each step, the emission spectrum on CCD2 is recorded. Figure 4.19 shows a waterfall plot of the resulting spectra as a function of the relative sphere height. We observe that the lasing modes hop between several different q order modes. This demonstrates that when changing the coupling positions, the mode competition condition is changed. It should be noted that the volume of excited neodymium ions is not changed, since the same WGM at 801.92 nm is excited.

In addition, the performance of fiber coupled microsphere lasers is also very sensitive to the coupling gap. It is found that the lasing modes change when the coupling gap is varied. In the overcoupled region, the laser threshold is increased when the coupling gap is decreased.

As previously mentioned, the selected mode for pumping features a doublet structure. It is interesting to investigate the lasing performance when exciting the neodymium ions in the two symmetric and asymmetric resonances. For this purpose, the coupling gap is increased so that the two resonant peaks do not merge together. Figure 4.20 shows the display of transmitted pump signal and lasing signal on the oscilloscope, when the pump laser is scanned across the resonance over a range of 603 MHz at 5 Hz repetition rate. One can see that the resulting lasing signal is

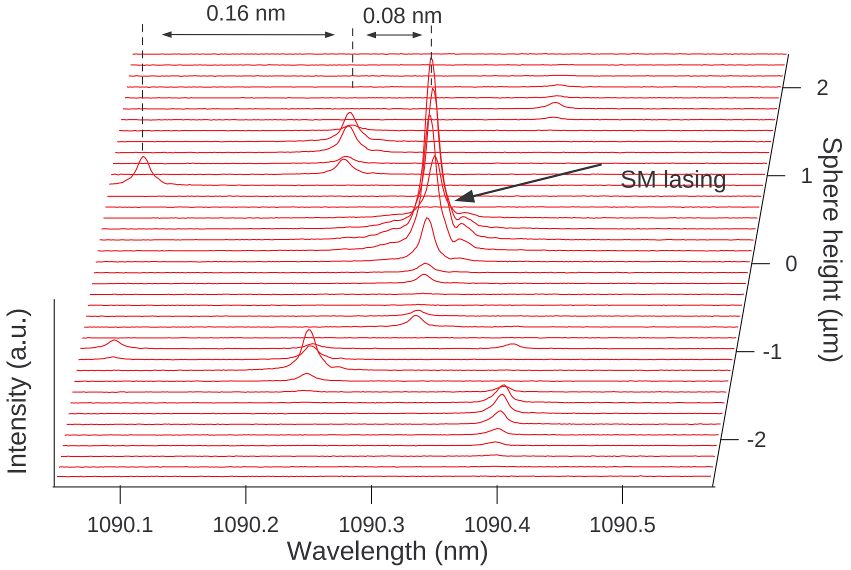

Figure 4.19: A 3D waterfall plot of emission spectra for different relative sphere height. The spacing of 0.08 nm corresponds to adjacent q order modes.

similar when these two modes are excited.

4.3.4 Microlaser characterization using scanning Fabry-Perot interferometer

The laser performance analysis of a ultra-high-Q laser using a grating based spectrometer is limited by its resolution. This limited resolution can be overcome by using a scanning Fabry-Perot interferometer (FP). This technique will namely allow to investigate the red shift of the laser induced by the thermal effect, which otherwise could be seen only with a much higher pump power [103].

The experimental setup is sketched in figure 4.21. The taper output signal is split by a dichroic mirror, so that the transmitted pump signal can be monitored by the silicon photodetector PD1. The reflected microlaser signal is sent into a FP, equipped with an InGaAs photodetector PD3 (sililar to PD2) used to detect the FP transmission spectrum.

A reference laser of wavelength $\lambda = 1083$ nm is first used to align and to test this setup. A high voltage triangle modulation signal is applied to the PZT of the FP, with an amplitude adjusted to cover at least one FP FSR.

Figure 4.22 shows the corresponding transmission spectra of the FP : in figure

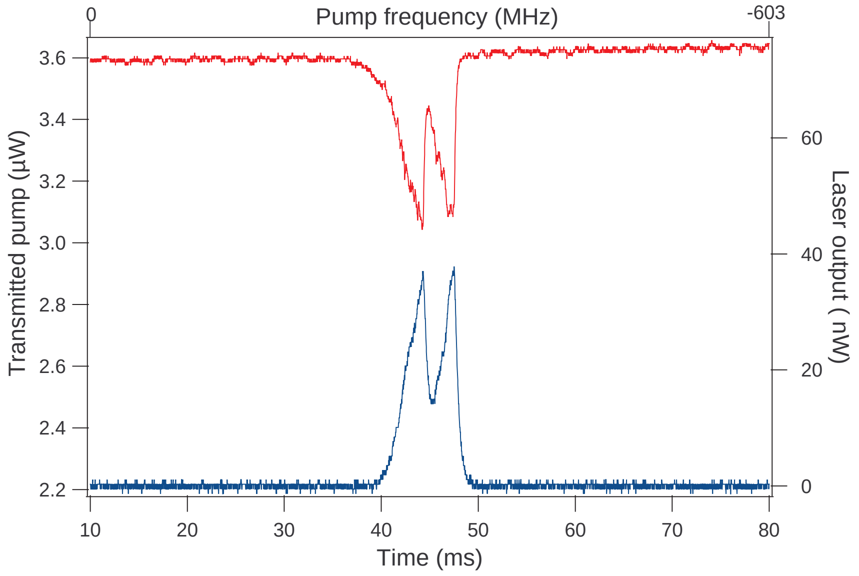

Figure 4.20: Absorbed pump power (PD1, top curve) and emitted signal (PD2, bottom curve) for a resolved doublet pump mode in the undercoupled regime. The splitting is about 18 MHz.

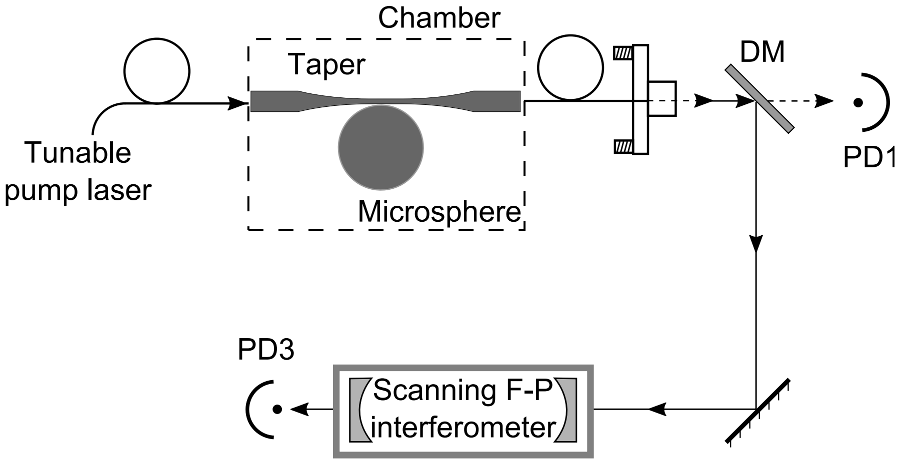

Figure 4.21: Schematic of experimental setup using scanning F-P interferometer.

4.22 (a) is shown a typical multimode lasing spectrum, where several laser peaks appear in one FP FSR of 750 MHz. In this figure, the upper curve is obtained with a higher absorbed pump power than the lower one. In particular, one observe two adjacent peaks, with a constant separation, sharing the same threshold, slope efficiency, and roughly the same power. This suggests that it is a “doublet laser”, which is supported by the order of magnitude of their splitting of about 20 Mhz.

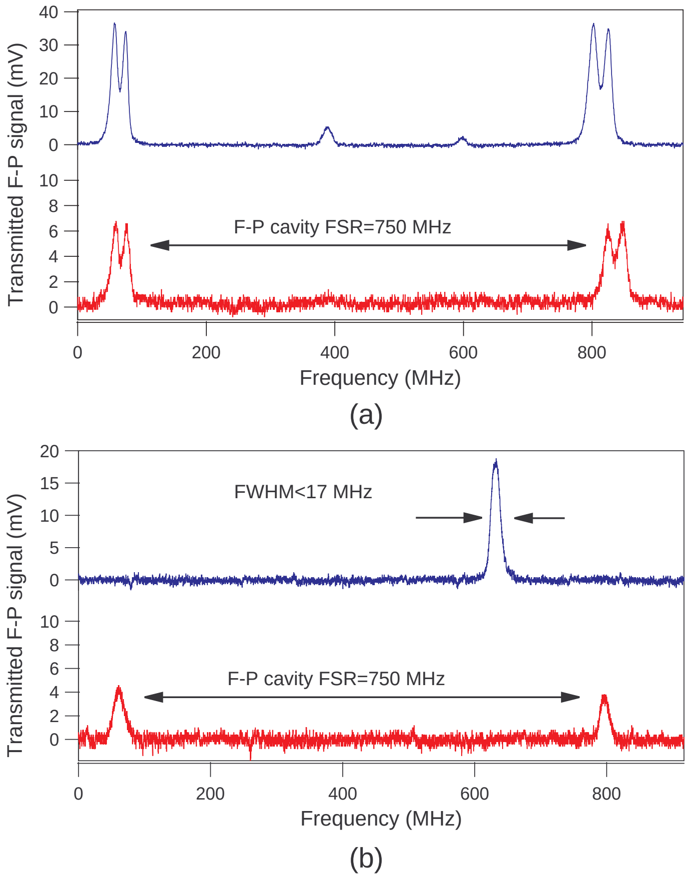

Figure 4.22: Transmission spectra of scanning F-P interferometer. (a): multimode lasing; (b) single mode lasing. For both (a) and (b), the upper curve was recorded with a larger absorbed pump power.

Single mode lasing is restored by a suitable adjustment of the coupling gap and of the taper height, as demonstrated in figure 4.22 (b). The spectral linewidth of this laser peak is about 16 MHz, similar to the width of the FP modes, as determined by using the DBR reference laser, the width of which is about 1.5 MHz. Finally, one also observes on (b) a shift of the microlaser peak when increasing the absorbed pump power: this shift will be analysed in the next paragraph.

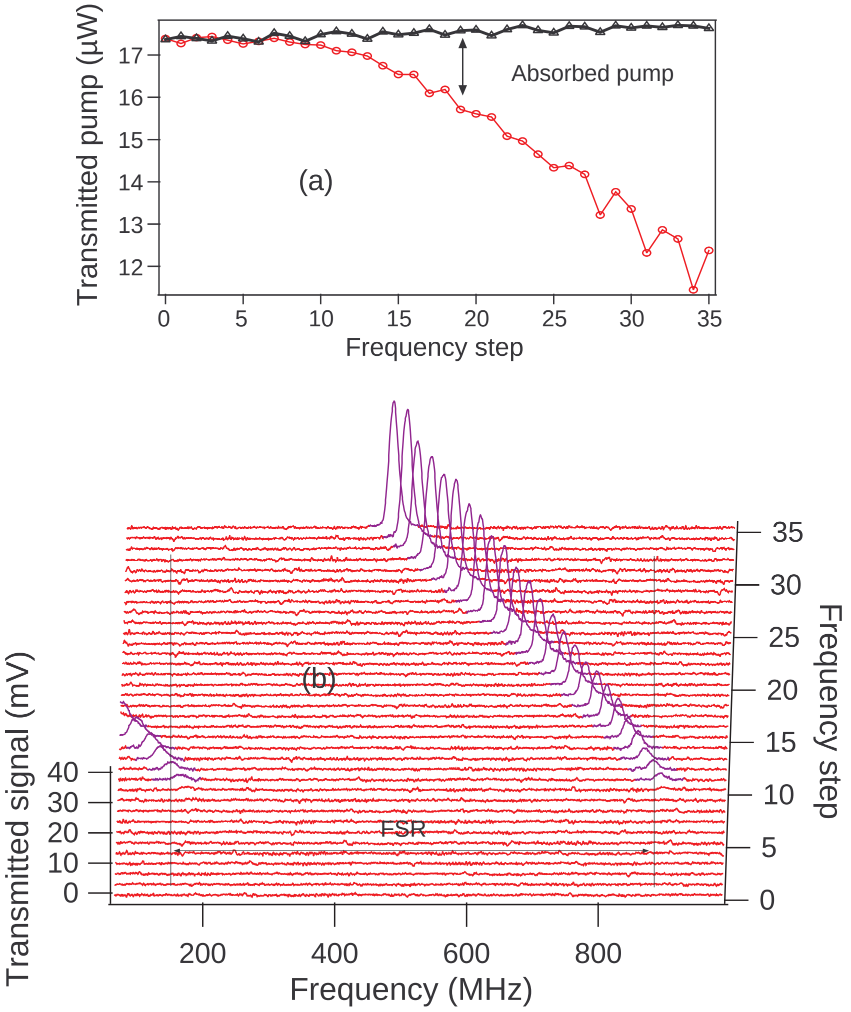

Figure 4.23: (a) The transmitted pump power as a function of the frequency step (PD1). The black curve: $g \sim \infty$; The red curve: $g \sim 200$ nm. (b) The transmission spectra of scanning F-P interferometer for different absorbed pump powers.

Red-shift of microlaser

The red shift phenomenon results from the thermal effect on the laser frequency. As described in chapter 3, the absorbed pump power heats the microsphere and changes its temperature. The higher the absorbed pump power, the higher the temperature, and the higher the refractive index of the sphere. This results into shifting the WGM modes toward longer wavelengths (or lower frequencies) as already explained in Chapter 3 for the pump resonance. But we are here interested in the cross effect between the pump and the emitted laser signals.

To investigate this phenomenon, we used step-by-step scanning and recorded the corresponding transmission spectra of the FP plotted in Figure 4.23. In the first ten frequency steps, the pump is still out of resonance and does not enter into the cavity : hence there is no laser signal. From the eleventh and following frequency steps, when increasing the coupled pump power, one observes the increasing laser peak height and its simultaneous shift towards lower frequency.

From figure 4.23 (b), we extract the position of lasing peaks highlighted in blue and plot it as a function of the absorbed pump power as shown in figure 4.24. One observes that the shift of the lasing mode is proportional to the absorbed pump power. A linear fit gives a slope of -73 MHz/μW, which means that one micro watt increase of absorbed pump power will lead to 73 MHz of laser shift toward lower frequency (red-shift). On the other hand, the dependence of a WGM shift on its temperature change K as previously given in equation (3.2) is $K \approx$ 2.4 GHz/K. Therefore, the slope of temperature change versus absorbed pump power is about 0.03 K/μW, which could be used to improve the analysis of thermal losses in Chapter 3.

The moderate value of this slope is an important point to complete the validation of the "continuous scanning" method exposed in Chapter 3. Indeed, when scanning the injected pump power, we modulate the WGM resonance frequencies, which could have two effects: a chirp of the laser output, and a shift of the resonance frequency out of the gain curve. The latter is not to be considered in our room temperature experiment because the homogenous linewidth of neodymium is very large, in the range of 1 500 GHz in silica [38]. It would obviously be different at low temperatures, especially if the crystalline structure of the Gd_2O_3 host matrix allows to reduce the inhomogeneous linewidth of the $^4F_{3/2} \longrightarrow {}^4I_{11/2}$.

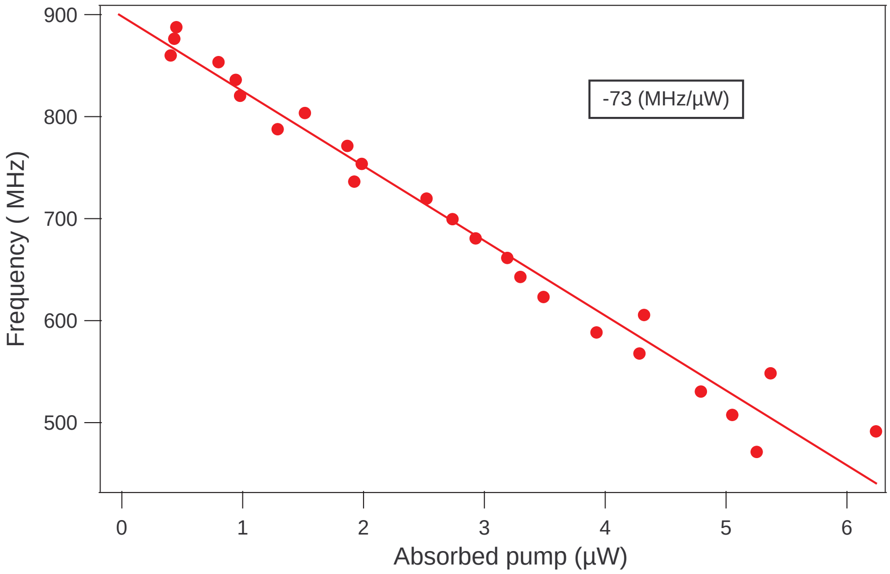

Figure 4.24: Microlaser frequency shift as a function of absorbed pump power.

Chapter 5

Other results in microlasers

In the previous chapter, we have reported a silica microsphere laser functionalized by Nd^{3+}:Gd_2O_3 NCs with a threshold as low as 40 nW, which is the lowest threshold ever recorded for any optical pump rare earth laser. In this chapter, the microlasers based on different active materials or different WGM microcavities have been achieved and studied. First, a silica microsphere microlaser with diameter of 73 μm activated by Yb^{3+}:Gd_2O_3 NCs is realized even by pumping at the low absorption region $\lambda = 802.01$ nm. The measured threshold is 1.3 μW which is the lowest threshold for any Yb lasers. Secondly, we have realized the fabrication of a neodymium implanted on-chip rolled-down microtoroid from a silica microdisk with a large wedge. It solves the problem resulting from a typical rolled-up microtoroid, where the active layer is buried inside the cavity. In our case, the active layer is kept on the periphery of microtoroid enabling better coupling of fundamental WGMs and emitters. The Q factors of this cavity are measured as 4.2×10^7 at 776.01 nm and 2.2×10^7 at pump wavelength 803.41 nm. A single mode lasing at 909 nm is obtained with a measured absorbed threshold pump power of about 210 nm, which is believed to be lowest threshold for any quasi-three-level laser.

5.1 Microsphere lasers using Yb^{3+}:Gd_2O_3 nanocrystals

As another popular lanthanide material, the trivalent ion Yb^{3+} has also been widely used for solid state lasers. Similar to neodymium, this rare earth can be embedded in various host materials and is used to build high power lasers for cutting and defense. Considering the potential application of low power microlasers for sensing applications, there is also a need to investigate low threshold and high-Q Yb^{3+}

microlasers. The fused WGM mode microcavities therefore are ideal laser cavities for it. In recent years, Ostby *et al* measured a 1.8 μW absorbed pump power for Yb^{3+} doped silica microtroid laser fabricated by sol-gel process [104]. They also demonstrated the laser performance of such microlasers in water for its potential application as a biosensor [105].

On the other hand, the colloidal Yb^{3+}:Gd_2O_3 NCs have been prepared using the polyol method as described in section 4.1.1 and attracting interest in biolabelling field. However, the laser performance based on these nanoemitters has not yet investigated. Since Nd^{3+}:Gd_2O_3 NCs based microsphere lasers have been realized and possess ultra low threshold performance in sub-microwatt region, as described in previous chapter, an investigation of a microsphere activated by Yb^{3+}:Gd_2O_3 NCs would also be interesting. However, due to the lack of a tunable laser source at the proper pump wavelength around 970 nm, the free running laser around 804 nm previously used for Nd is chosen to excite Yb^{3+} ions. In fact, the absorption efficiency of Yb^{3+} at this wavelength is very low so that the required threshold to achieve lasing is expected to be much higher. Nevertheless, we have achieved a low threshold microsphere laser based on these nanoemitters by pumping at 802.01 nm. The measured threshold is as low as 1.3 μW which is even lower to the previous mentioned lowest Yb threshold. One can thus expect a lower threshold by pumping at the proper wavelength around 970 nm.

5.1.1 General properties of Yb^{3+} ions

The trivalent ytterbium ion is characterized by a very simple electronic energy level structure as shown in Figure 5.1, where the next higher energy level is only accessible with near UV pump. Its simple structure is comprised of only two energy states : the ground state ($^2F_{5/2}$) and one excitation state ($^2F_{7/2}$), which makes it possible to avoid the losses that exist in other energy structures due to up-conversion and excited-state absorption. In general, each state has several stark sublevels induced by the electric field of its host material. This makes the laser action in Yb^{3+} ions a quasi-three-level system, which is supposed to have higher lasing threshold compared to a four-level system like Nd^{3+}. Moreover, it also has smaller quantum defect[1] leading to less heat loss compared with neodymium. Figure 5.1 shows the typical transitions excited at the pump wavelength around 970 nm. The scheme of transitions when pumping at 802 nm is shown in (b).

---

[1] Quantum defect: Energy lost in the non-radiative transitions.

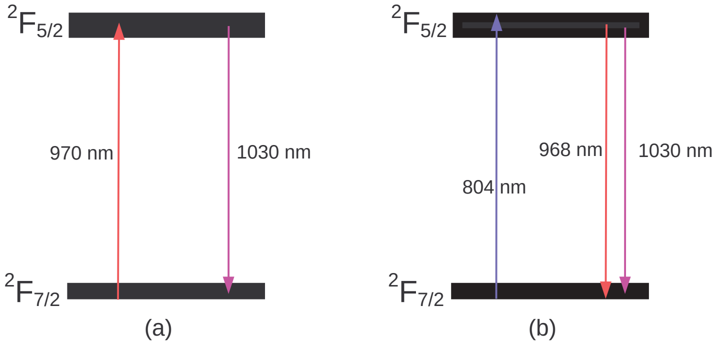

Figure 5.1: Energy level schemes of Yb^{3+}: (a) by pumping 970 nm; (b) by pumping at 804 nm.

Because the absorption efficiency of Yb^{3+}:Gd_2O_3 NCs at 802 nm is rather low, we failed to obtain its emission spectrum by simply pumping into a Yb^{3+}:Gd_2O_3 NCs activated silica microsphere from free space, which has been described in section 4.1.1. Nevertheless, their photoluminescence can be investigated when it is coupled with the ultra high Q WGMs by a fiber taper coupler.

5.1.2 Q factors of the active microsphere

First, a silica microsphere with diameter of 73 μm is fabricated at the end of a tapered fiber tip, as described in chapter 1. It is then dipped coated by the prepared Yb^{3+}:Gd_2O_3 colloidal suspensions for a few seconds. The resulting coating film is expected to be a few tens of nanometer thick. Since the fundamental mode of the microsphere locates in the depth of about 1 μm below the surface and these nanoemitters should be activated by an annealing process, we control the CO_2 laser radiation with low power to slightly melt again the sphere for a few seconds. This results in both annealing and embedding the nanoemitters close below the surface for better coupling to the cavity WGMs. A single mode fiber taper produced for 1083 nm is then selected in this study. The measurement of the quality factors of the microsphere in both pump wavelength and emission wavelength are presented in the following.

Q factor at pump wavelength

Compared with a passive microsphere, the Q factor at pump wavelength in an active microsphere is also determined by the absorption of rare earth ions. In general, this absorption is mainly decided by the ion concentration and the absorption cross section at the pump wavelength. In the case of Yb^{3+}:Gd_2O_3 NCs, the absorption cross section of Yb^{3+} is expected to be close to what is in silica which is well known around 970 nm. However, this cross section at 802 nm is seldom provided because it is already less than 1% of the peak value. Thus we can confidently expect to have high Q factor at 802 nm for the functionalized microsphere.

To verify this, the spectral linewidth of selected WGM resonances at 802.01 nm is measured. Figure 5.2 shows the transmission spectrum of this resonance, which is recorded in the undercoupled region and with low power probing, to avoid resonance shape distortion due to the thermal effect. A theoretical fit is also performed shown by a solid line. The fit parameter gives a splitting of 3.3 MHz and a FWHM of 1.2 MHz corresponding to Q factor of 3.0×10^8. The ultra high Q factor at pump wavelength just confirms the previous assumption of the weak absorption of Yb^{3+} at 802 nm.

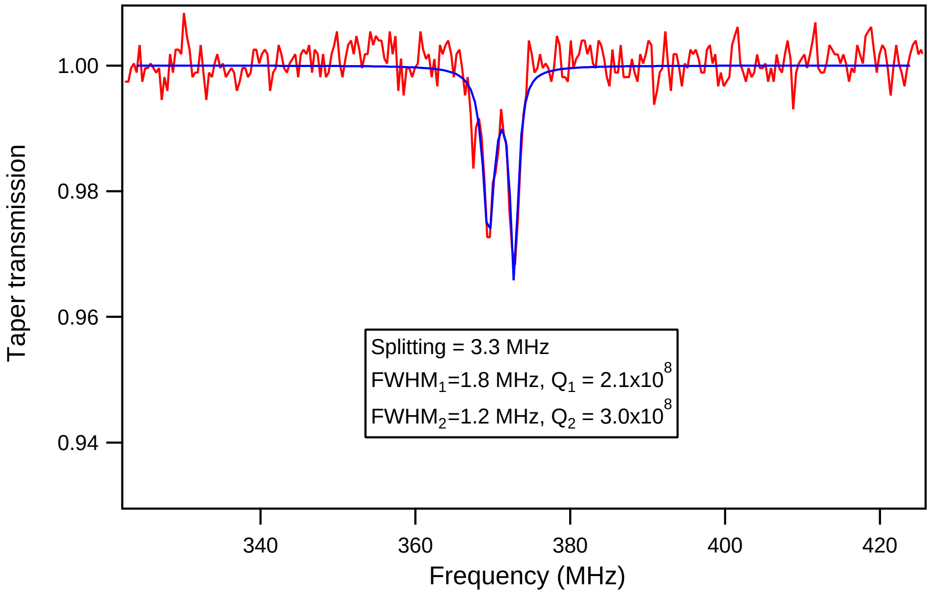

Figure 5.2: Transmission spectrum of the selected WGM at $\lambda = 802.01$ nm, showing a doublet structure with Q factor as high as 3×10^8.

Q factor at emission wavelength

The Q factor of the active microsphere at pump wavelength allows one to have an idea of the quality of such a cavity. Since Yb^{3+} ions have rather low absorption at

1083 nm, the measured Q factor of a good active microsphere would have ultra high Q factors at emission wavelength as well as a passive microcavity. Moreover, it can also be used to estimate the linewidth of microlaser signal using Shawlow-Townes equation. The DBR laser diode as mentioned in former chapters is used to probe the spectra linewidth of the cavity at 1083 nm. It should be mentioned again that the spectral linewidth of this tunable laser is supposed to be about 1.5 MHz, which sets a lower limit to the measured linewidth. As shown in Figure 5.3, the transmission spectrum of this cavity at 1083 nm shows two WGMs that both possess doublet structure with different coupling efficiency. A fit is then performed in the second resonance mode, which gives a splitting value of 11 MHz and a small FWHM of 1.7 MHz corresponding to Q factor of 1.6×10^8. As a result, we assume that the actual linewidth is much less than 0.2 MHz, which corresponds to a Q factor in the range of 10^9. In fact, we are able to easily produce such active microspheres with ultra high Q factors above 10^8.

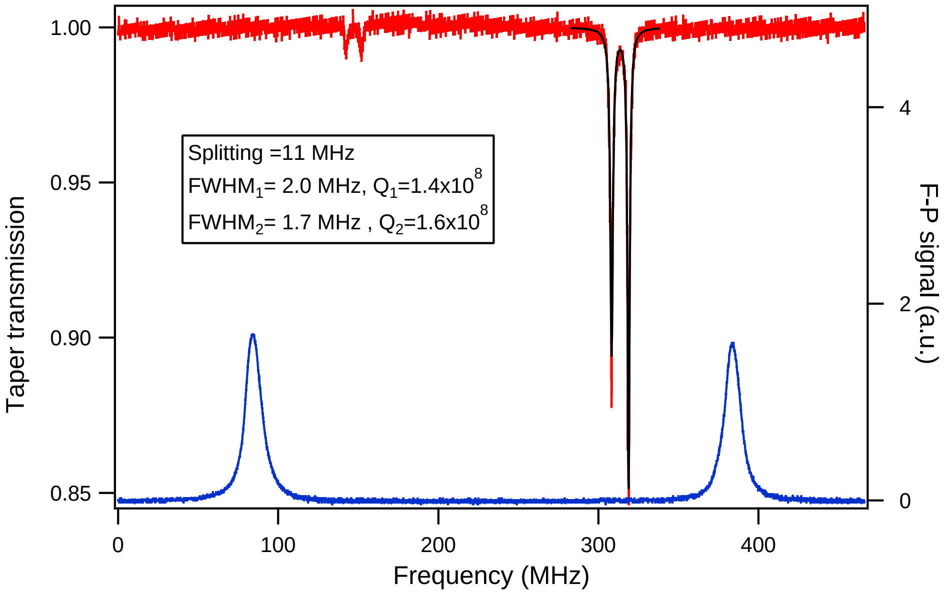

Figure 5.3: Transmission spectrum of a WGM resonance at $\lambda = 1083$ nm, showing a doublet structure with Q factor as high as 1.4×10^8.

5.1.3 Laser results

In fact, few experiments have been carried out to excite Ytterbium ions at the wavelength around 800 nm, and thus no laser action was reported by pumping at this wavelength. Nevertheless, we succeed to realize and investigate the laser performance of Yb^{3+}:Gd_2O_3 NCs by pumping at this wavelength as will be described in the following.

The single mode sub-wavelength fiber taper used here is produced by drawing from a standard single mode fiber using a butane/air flame as described in chapter 2. The corresponding experimental setup is previously presented in chapter 3. By scanning the pump frequency across the selected resonance at 802.01 nm, the pump signal of 21 μW is coupled into cavity through the fiber taper. The internal thermal heating due to absorption of circulating pump power distorts the resonance shape, resulting in a slow slope in frequency decreasing side. Taking this advantage, one can therefore investigate the emission properties by simply utilizing the resonance dip, as already discussed in chapter 3.

Figure 5.4 shows its emission spectra with increasing absorbed pump power. The exposure time for CCD is set as 0.4 s. The envelope of photoluminescence spectrum below threshold provides the information of energy transitions in Yb^{3+} ions, which shows two emission bands around $\lambda = 968$ nm and $\lambda = 1030$ nm corresponding to the transitions from $^2F_{5/2}$ to $^2F_{7/2}$ manifold. Because the emission cross section overlaps with its absorption cross section at the former emission band, laser action normally occurs in the latter emission region. The inset gives a magnified view of a highlighted region marked by a black rectangle. The spacing between two peaks marked as black arrow corresponds to the cavity FSR. It is measured as 3.2 nm around 1050 nm which is in a good agreement with the calculated value of 3.3 nm for a 73 μm diameter microsphere. The red arrow denotes a small spacing of 2.2 nm which is 70 percent of its FSR. This corresponds to the polarization splitting as mentioned in section 4.1.2. Moreover, one can easily observe two lasing modes with different thresholds in this Figure, which possess the same TM polarization.

To further characterize the lasing properties, we plot the recorded spectra in a 3D waterfall plot as shown in Figure 5.5, where the absorbed pump power is varied at each frequency step. One can easily observe the two lasing modes at 1052 nm and 1063 nm which have much higher intensity in contrast to other emission peaks. For clarity, they are labeled as Lasing A and B in red and blue, respectively. Meanwhile, a PL peak at 1031.4 nm is also marked as PL C in green.

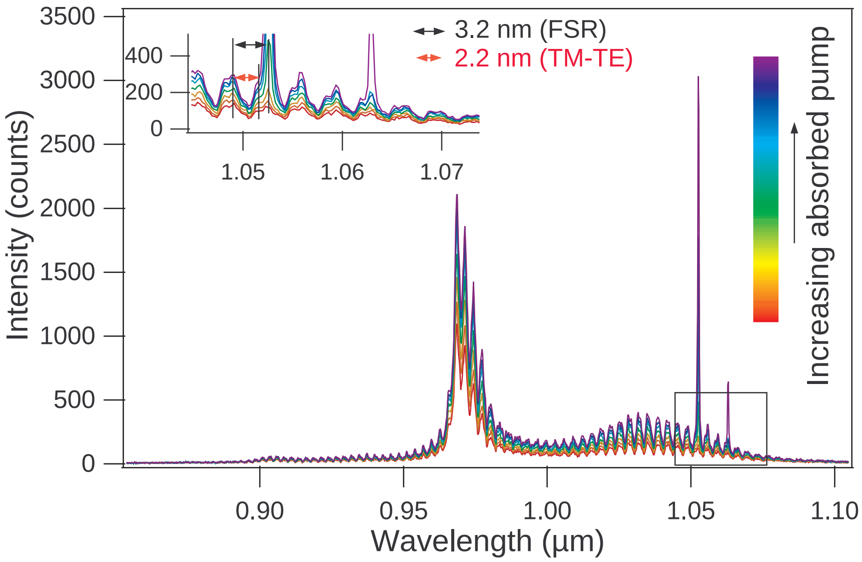

Figure 5.4: The emission spectra for increasing absorbed pump powers (not corrected for CCD QE). Inset denotes a magnified view of the highlighted region, demonstrating the onset of two lasing modes at 1053 nm and 1063 nm. The black arrow denotes its FSR at 1031 nm and the red arrow denotes the spacing between TM and TE polarization.

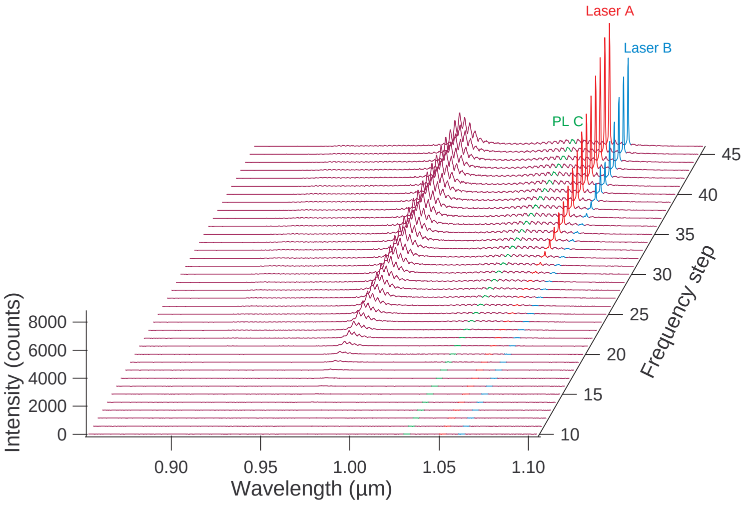

Figure 5.5: Waterfall plot of the emission spectra with increasing absorbed pump power (not corrected for CCD QE).

The corresponding transmitted pump signal at each frequency step is plotted in Figure 5.6 (a). The empty triangles denote the transmitted signal without microsphere (gap is large enough) and the empty circles present the transmitted signal with a WGM resonance dip. On the other hand, the intensity of two lasing signal A,B and the selected PL signal C is extracted from CCD spectra as shown in Figure 5.5 by integration over a range of 16 pixels (or 3.7 nm). They are then plotted in the same Figure as solid circles, triangles and squares respectively. It is found that the averaging transmitted pump signal from the oscilloscope is not large enough to eliminate the noise, which is mainly due to the jitter noise in pump laser signal especially for such a high Q resonance at pump wavelength. The absorbed pump power can thus be decided by the dip depth, where the base line is a linear fit on the transmitted signal without microsphere.

The selected emission signals extracted from CCD are then plotted as a function of the absorbed pump power, as shown in Figure 5.6 (b). For clarity, the PL C signal is magnified by a factor of 3. The laser threshold is then found to be about 1.3 μW for laser A and 1.6 μW of laser B. It should be noticed that the PL peak value saturates immediately after laser action occurs, which is another evidence of the laser action.

To the best of our knowledge, this threshold is the lowest threshold ever recorded for any Yb lasers, even it is not pumped at the proper wavelength. One can thus expect that a lower threshold can be achieved if it is pumped at 970 nm at which ytterbium ions have much larger absorption cross section.

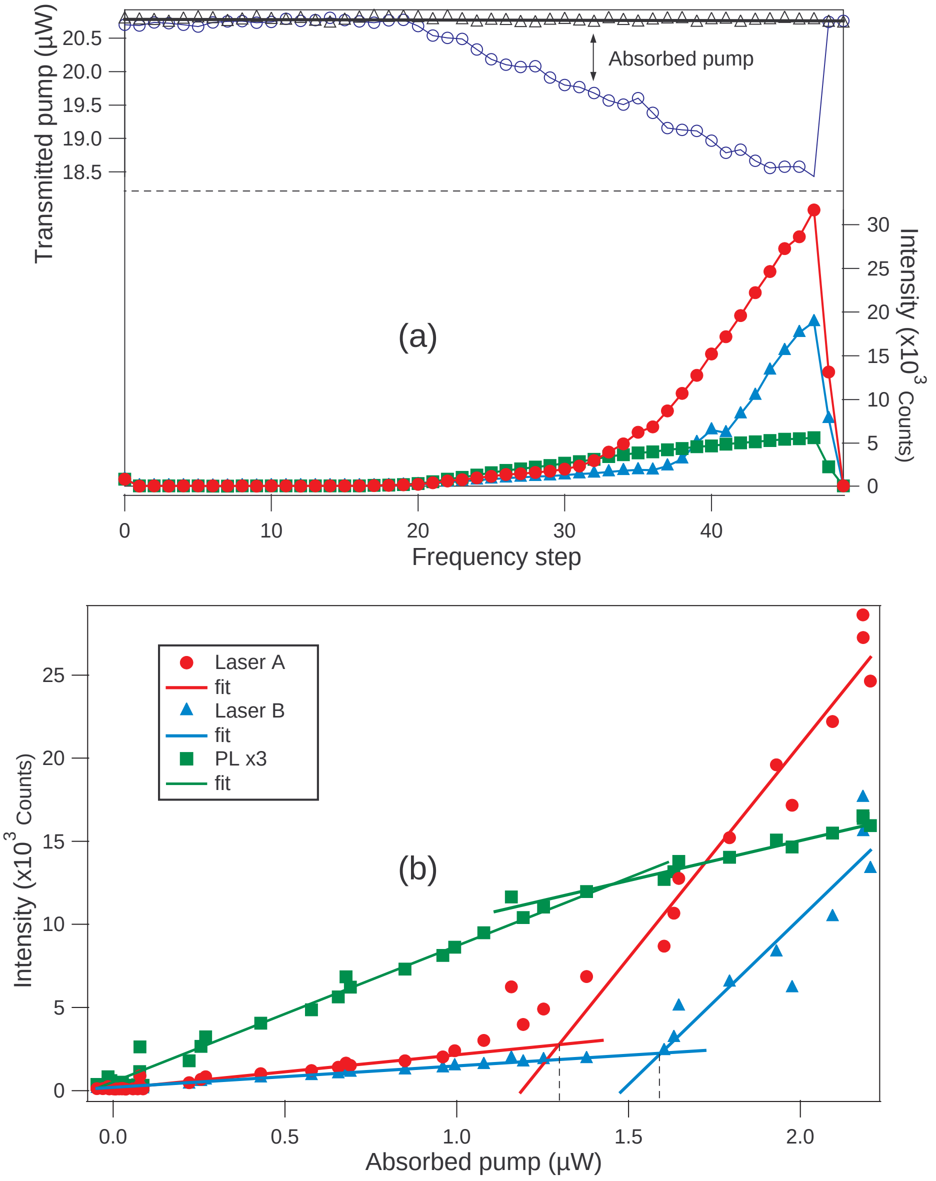

Figure 5.6: (a) Upper curves: Transmitted pump signal with and without sphere. Lower curves: Integrated intensity of laser A, laser B and PL C on CCD. (b) Integrated intensity of laser A, laser B and PL C x3 as a function of absorbed pump power. PL C ×3 represents a zoom view on PL C signal by a factor of 3.

5.2 Neodymium implanted silica microtoroid lasers

On-chip optical toroidal microcavities were first introduced in 2003 [16]. These cavities combine the advantage of silicon microfabrication technology and melting processes using CO_2 laser irradiation. Like the fused silica microspheres, they possess ultra-high Q WGM resonances resulting from successive Total Internal Reflections (TIR) on their very smooth circular borders induced by surface tension. Moreover, they have smaller mode volumes and thus cleaner mode structures. These fabrication processes also allow better control on their sizes compared to microspheres. Another key advantage of these on-chip microtoroids is that they permit the integration of other microfabrication techniques in the production processes, such as realization of an electrical based thermal optical tuning system [106]. As a result, such microcavities have been attracting large of interest in the recent years. Many works have been carried out ranging from fundamental research like cavity quantum electrodynamic [107] and cavity optomechanics [108] to more practical applications like sensors [76], rare earth based lasers [32, 109], quantum dot lasers [110] and more recently the phonon lasers [111].

The approach to obtain an active silica microtoroid is one main concern for realization of ultra low threshold microlasers. The first rare earth doped silica microtoroid laser was achieved by sol-gel coating [32]. However, this process has limited control on the density of rare earth ions and its depth distributions. Therefore, the ion implantation that is easily integrated into the processes of microtoroid fabrication was employed and an erbium implanted microtoroid laser was thus demonstrated in 2004 [32]. On the other hand, in order to achieve the best coupling condition of the ions and fundamental WGMs, the ions should be engineered into the location of these modes which locate at about 1 μm depth under the surface. But it turns out that the production of a toroid typically results from *rolled-up* structure of the microdisk preform[33], which has the effect to bury the active layer inside the toroid and thus increases the difficulty of active region control.

In this work, a neodymium implanted microdisk with an etched edge is fabricated. By controlled CO_2 laser irradiation, a microtoroid with outer diameter of 30.2 μm is achieved by *rolling down* the edge of a microdisk. The measured quality factor is as high as 4.2×10^7 at the wavelength $\lambda = 776.01$ nm, which is expected to be higher at emission wavelength where neodymium has weak absorption. Moreover, a single mode laser action at 909 nm is achieved when pumping at the wavelength $\lambda = 803.41$ nm. The measured threshold pump power is as low as 210 nW. To the best of our knowledge, this is the lowest threshold record for any quasi-three-level continuous laser.

5.2.1 Fabrication of a rolled-down microtoroid

The preparation of such a rolled-down microtoroid laser consists of two steps, involving successively silicon microelectronic processes and CO_2 laser fusion of silica. The first step is the fabrication of raised silica microdisks. A 2.7 μm thick layer of silica is grown on the wafer by thermal oxidization of silicon. It is then bombarded with 600 keV Nd3+ ions with fluency of about 10^{14} ions $\cdot$ cm^{-2}. The depth distribution of Nd^{3+} ions in matrix calculated using SRIM software yields a gaussian distribution profile with the peak at the depth of 200 nm. After ion implantation, the photolithography, wet etching and reactive ion etching processes as described in section 1.3.1 are employed. It should be mentioned that the silica layer becomes porus after ion implantation and the resin can not be bonded well on its surface. As a result, the etching process results in a wedge structure [2] of the microdisk as can be easily observed in Figure 5.7, which shows the angle view and top view SEM graphs of a final microdisk sample. The measured diameter of disk and its silicon pedestal is 69 μm and 14 μm, respectively. The neodymium implanted layer is reserved in a center region with diameter of 36 μm. In fact, this wedge plays an important role for the production of abnormal rolled-down structure in the second step, as will be discussed in the following.

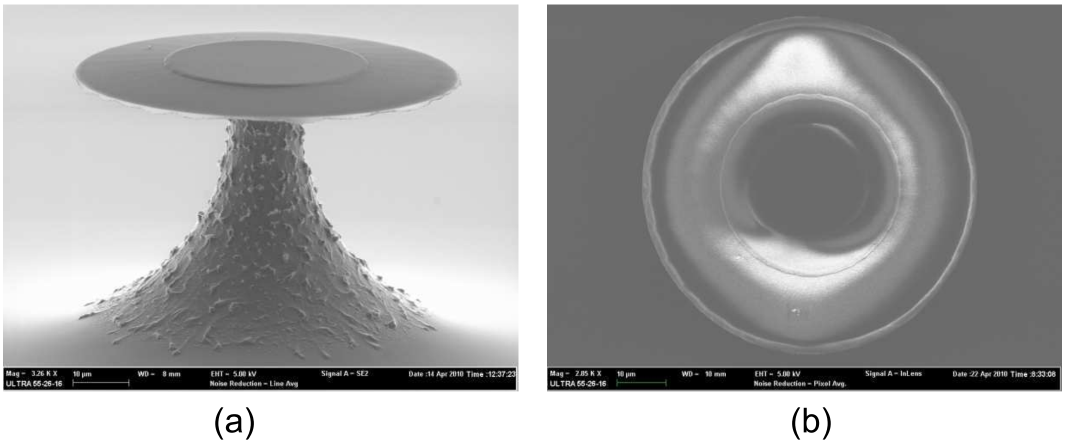

Figure 5.7: SEM graphs of a produced neodymium implanted microdisk. (a) 76° angle view; (b) 90° top view.

---

[2] See the drawing of the cross section in figure 5.8(b).

In the second step, a CO_2 laser is employed to fuse the silica. Here we choose to focus the CO_2 laser beam at a 110 μm waist spot and fuse a single disk. To better understand the melting process, a schematic of melting processes for both rolled-up and rolled-down toroid is given in Figure 5.8.

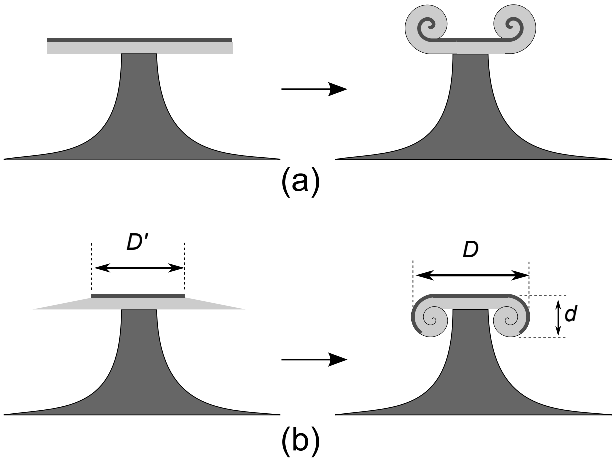

Figure 5.8: Schematics of the rolling process of microdisk under CO_2 irradiation. (a) Rolling up; (b) Rolling down. The gray layer denotes the ion implanted region.

Figure 5.8 (a) presents the schematic of the melting process of a typical ion implanted silica microdisk without large wedge. Under the radiation of a CO_2 laser, the silica is heated up, while the silicon pedestal quickly transfers the heat down its wafer. As a result, only the edge of the disk can easily reach its melting temperature. The surface tension force then rolls up the melted edge and results in a toroidal shape structure on the disk as sketched in Figure 5.8 (a). This structure had been verified by Kalkman *et al.* [33].

Figure 5.8 (b) describes a fabrication process of an abnormal rolled-down microtoroid. A possible mechanism is that the surface tension of fused silica first rolls down its wedge shape edge. As a result, the rolled-down part is less efficient cooled down the the main disk body and the following melting keeps rolls down the edge. In particular, to have the active layer cover the periphery of the toroid, the final diameter of the toroid should be small enough. Assuming a circular toroid, this condition can be written as follows:

$$D - d + \pi d/2 \leq D' \tag{5.1}$$

where D is the diameter of the active layer of the microdisk, D and d are the outer diameter and minor diameter of the toroid, as also shown in Figure 5.8 (b).

Here, the CO_2 laser irradiation time is set to be 150 ms by external pulse trigger. The silica microdisk is then positioned at the focus of CO_2 laser beam. We heat the sample for several times with increased power to 1.5 W, where the microdisk begins to be melted through the observation of reduced diameter from a microscope. Then, we increase the laser power to 2 W to further reduce the size of produced microtoroid.

Figure 5.9 shows the SEM graphs of the resulting microtoroid with a magnification of ×8860 taken at an angle of 64°. In this figure, the outer diameter of the microtoroid is measured as 30.2 μm and its thickness is 9.6 μm, matching equation (5.1). It can be easily observed that the microtoroid has a smooth surface on its side, but the deposition of silica nanoparticles is also found on the top, which is believed to come from the evaporation of silica in the melting process. Nevertheless, it doesn't affect the fundamental WGM mode of this cavity but helps to add losses to its higher order modes.

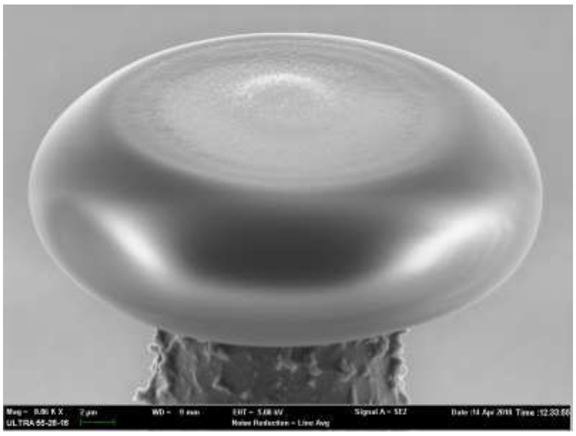

Figure 5.9: SEM graph of resulting microtoroid with a magnification of ×8860.

To further confirm this structure, two SEM graph taken at the same angle of 76° are put together with the same scale factor and the top one is set as partial transparent, as shown in Figure 5.10. Obviously, the top of silica layer above the pedestal remains unchanged, which directly proves the fact that the edge of microdisk rolls down during the melting process under the irradiation CO_2 laser beam. To confirm this, we also melt an adjacent microdisk and stopped the diameter reduction at 43.7 μm. Its SEM graph shows no rolled-up structure. Therefore, one expects the production of a microtoroid results from rolling down of a microdisk as schematically shown in Figure 5.8 (b). The advantage is that it can easily produce an active toroid with the active region on its periphery, enabling best coupling condition for

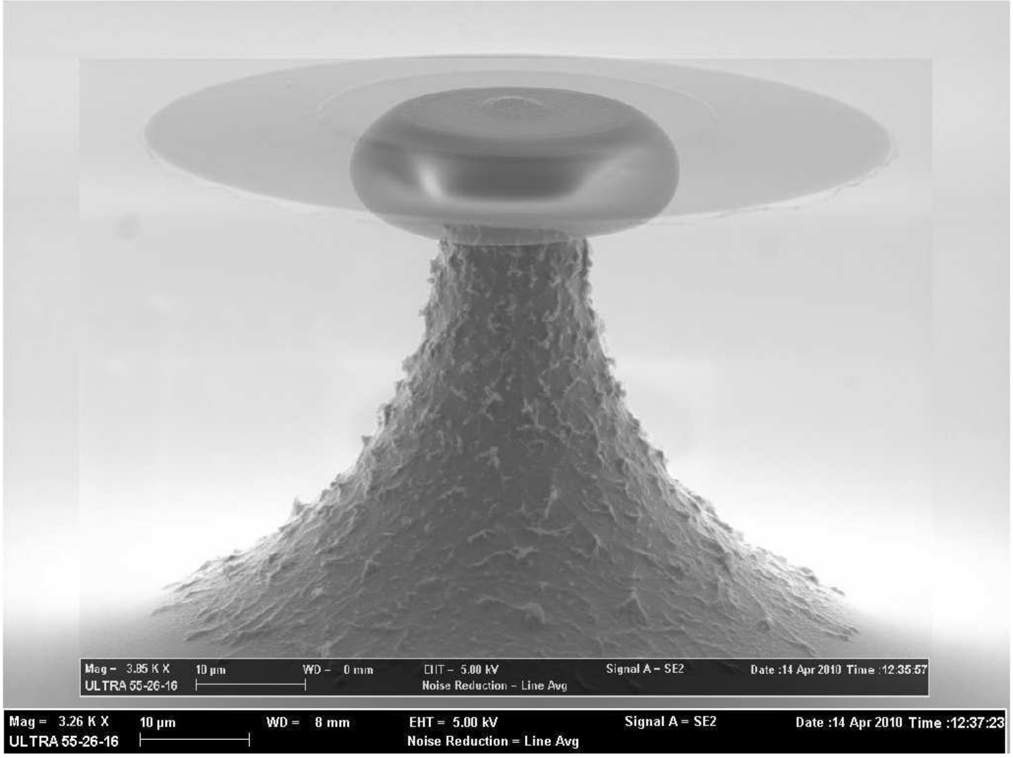

Figure 5.10: Overlap of the SEM graphs of a silica microdisk and a microtoroid, demonstrating the rolled-down structure of the microtoroid.

ultra high Q WGM to the emitters and so that single mode laser action can be easily achieved.

5.2.2 Q factors

A subwavelength fiber taper is fabricated by drawing a single mode fiber (Thorlab 980-HP) with the coating stripped part heated by a butane/air flame [65]. The transmission of this taper is as high as 98% with single mode operation at 1083 nm. It is then used to evanescently excite the WGMs of this toroid. According to 30.2 μm outer diameter of this toroid, the calculated FSR at 1083 nm is 8.2 nm. Unfortunately, our DBR laser diode with lasing wavelength at 1083 nm has a small tunable range which is much less than one FSR of this toroid, and we were not able to acquire its Q factor at emission wavelength. Therefore, a external cavity tunable laser (Newfocus TLB 6300) with a 15 nm tunable range is used here. The intrinsic Q factor can be calculated by $Q = \lambda/\delta\lambda$, where the intrinsic linewidth $\delta\lambda$ is measured in the undercoupled region with low laser power to avoid a thermal effect. Figure 5.11

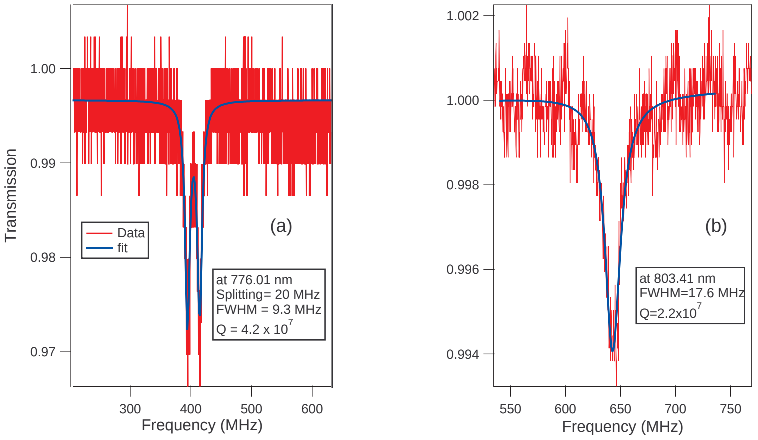

Figure 5.11: (a) Transmission spectrum of a WGM at 776.01 nm with a doublet structure. (b) Transmission spectrum of the WGM for pumping locating at 803.41 nm.

(a) shows the transmission spectrum of a WGM found at 776.01 nm, which gives a doublet structure. A fit of this curve gives a splitting of 20 MHz and a resonance linewidth of 9.3 MHz corresponding to Q factor of 4.2×10^7. It should be mentioned that photoluminescence is also observed when pumping at this wavelength. Therefore, we believe that the Q factor measured at emission wavelength would be higher.

Fortunately, we locate a WGM resonance at the pump wavelength of 803.41 nm using the free running laser diode. Figure 5.11 (b) gives the corresponding transmission spectrum recorded in undercoupled region. A fit gives a linewidth of 17.6 MHz, which corresponds to a Q factor of 2.2×10^7.

5.2.3 Emission spectra

We then pump the Nd^{3+} ions by exciting the WGM resonance mode around 803.41 nm. The transmitted signal is either filtered by long pass filter RG850 or by a dichroic mirror to detect the transmitted pump signal. A $f = 0.3$ m spectrometer is used to record the emission spectra.

Figure 5.12 gives three different emission spectra of this toroid. In (a), we didn't use a dichroic mirror in order to preserve the PL envelope. However, the dichroic mirror allows one to measure the transmitted pump signal and is used in the following laser measurement. In undercoupled region, an ultra-low threshold laser action is observed as shown in (c). To obtain its photoluminescence spectrum bellow thresh-

$n = 1,\ q = 0$	$\mathrm{TM}_{m=141}$	$\mathrm{TE}_{m=141}$	$\mathrm{TM}_{m=140}$	$\mathrm{TE}_{m=140}$	$\mathrm{TM}_{m=139}$	$\mathrm{TE}_{m=139}$	$\mathrm{TM}_{m=138}$	$\mathrm{TE}_{m=138}$	$\mathrm{TM}_{m=137}$	$\mathrm{TE}_{m=137}$	$\mathrm{TM}_{m=136}$	$\mathrm{TE}_{m=136}$
FEM (nm)	909.19 nm	913.36 nm	915.39 nm	919.61 nm	921.68 nm	925.96 nm	928.05 nm	932.39 nm	934.52 nm	938.92 nm	941.07 nm	945.53 nm
Spectra (nm)	909.0 nm	912.9 nm	915.4 nm	919.3 nm	921.5 nm	925.2 nm	927.6 nm	931.5 nm	934.0 nm	937.9 nm	940.3 nm	944.5 nm

Table 5.1: Comparison between the FEM simulated and measured WGM positions.

old, we reduce the gap between taper and microtoroid bellow 50 nm, so that the laser threshold is clearly increased due to the increased losses induced by the taper. The CCD exposure time set to be 10 s is then enough to obtain PL spectrum as shown in (a). The spectrum shows clear emission peaks which corresponds to the cavity's resonance modes. The measured spacing of 8.5 nm around $\lambda \sim 1080$ nm is in good agreement with the expected value. Let us recall that the silicon CCD has low quantum efficiency close to the wavelength of 1 μm. In this Figure, the quantum efficiency of CCD is taken into account. Figure (b) shows the PL spectrum with the presence of a dichroic mirror, which is obviously affected by the dichroic mirror.

Figure (c) shows a single mode lasing spectrum recorded with exposure time of 0.4 s. For the laser recording, the gap is set to be about 250 nm. The laser mode appears at the wavelength of 909 nm, which is the maximum position of the envelope of Figure (b). When we adjust the position of the taper, we only observe the same lasing mode. While in the case of a Nd^{3+}:$\mathrm{Gd_2O_3}$ NCs based silica microsphere laser whose diameter is about 41 μm, we have experienced that lasing condition is sensitive with respect to the position of taper. This demonstrate the advantage of such a microtoroid as the platform for single mode laser operation, where the competition of few WGMs leads to a stable single mode lasing.

We then apply the FEM modeling to study its mode positions. The cross section boundary of this cavity is obtained from a SEM image at the side view, as show in Figure 5.13 (a). The edge follows a 15° tilted ellipse with a major diameter of 9.1 μm and a minor diameter of 7.7 μm. Consider the fact that the fundamental modes locates at the equatorial edge, the ellipse structure is enough for the modeling. Also shown in Figure 5.13 (b) is the simulated electric field intensity $|E|^2$ distribution for a mode around the lasing position $\lambda \sim 909$ nm, which is found to be $\mathrm{TM}_{n=1,m=141,q=0}$ mode. The refractive index used in the simulation is 1.445, so that it can match the resonance positions. The estimated mode volume of this mode is 117 $\mu\mathrm{m}^3$.

Table 5.1 gives the comparison of resonance positions around 910 nm from the

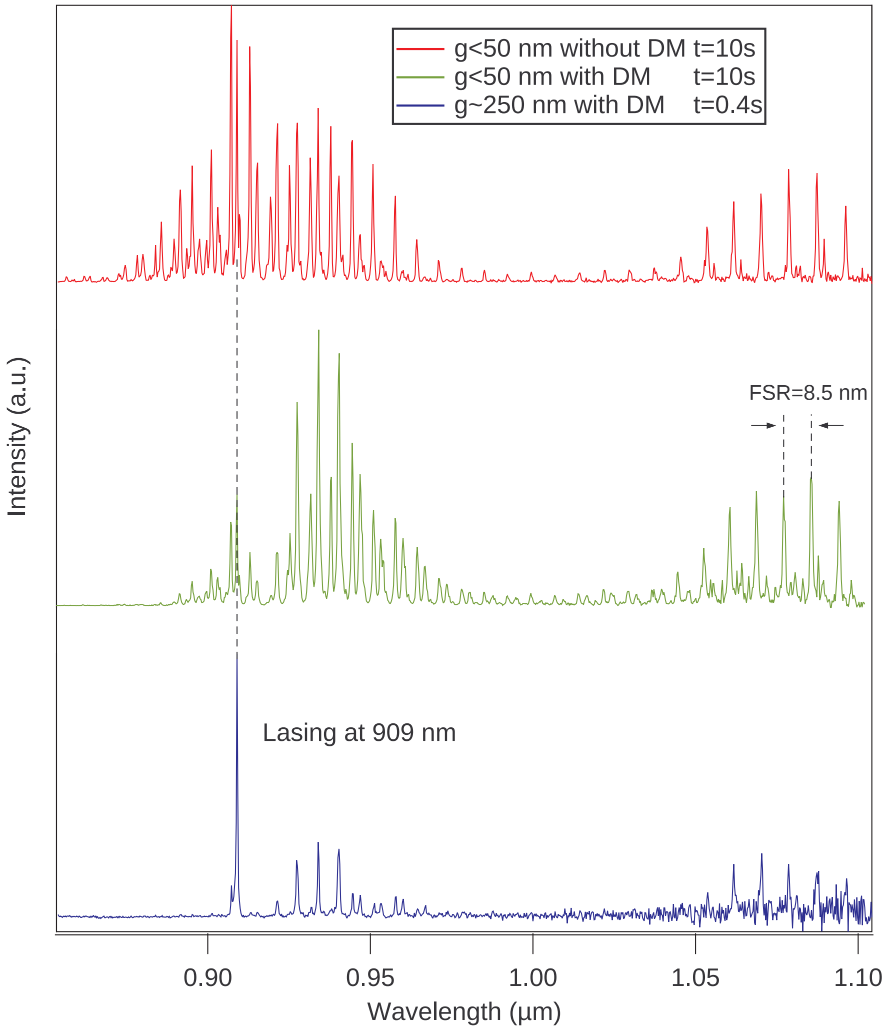

Figure 5.12: Emission spectra of the Nd^{3+} implanted microtoroid for different conditions. (a) Without a dichroic mirror (DM), in overcoupled regime; (b) With a dichroic mirror, in overcoupled regime; (c) With the dichroic mirror, in undercoupled regime. (Corrected by CCD QE)

photoluminescence spectrum and FEM simulations. The simulated fundamental mode positions well match with the experimental results, allowing to access the polarization and azimuthal mode numbers of the PL peaks.

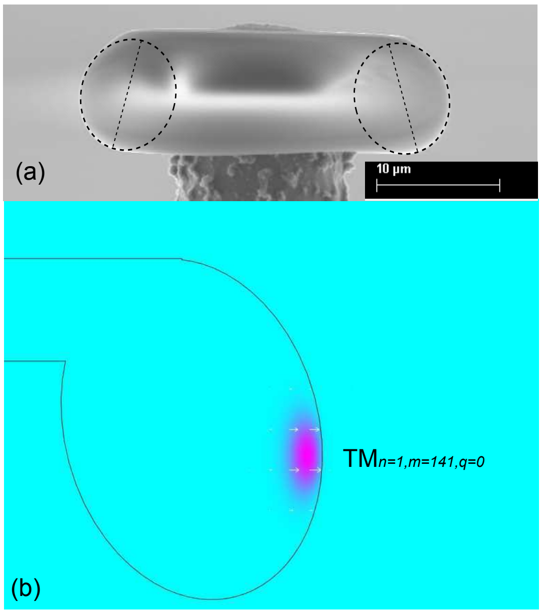

Figure 5.13: (a) SEM image of the toroid; (b) Electric field intensity distribution of TM$_{n=1,m=141,q=0}$ mode at 909.2 nm. The arrows indicate the electric magnitude and direction.

5.2.4 Single mode lasing threshold

To further characterize this single mode laser, we keep the gap at 250 nm and decrease the pump laser frequency across the WGM resonance around 803.41 nm by using the step by step procedure. At each step, the CCD is set to obtain the emission spectrum at 0.4 s exposure time and the corresponding transmitted pump power is also acquired by averaging from the oscilloscope. Figure 5.14 gives the emission spectra with increasing absorbed pump power at each frequency step. The fiber taper transmitted pump power with the microtoroid far enough is also recorded as a baseline marked by empty triangles in the inset. The absorbed pump power can then be easily derived from the dip depth of the transmitted pump signal (empty circles) compared to its baseline. The deformed resonance shape shown in the inset results from the internal heating of pump laser. In the spectra, one can easily observe the single-mode laser action at 909 nm, highlighted as red laser A. The weak emission signal at 1080 nm is invisible due to the bad quantum efficiency of CCD. Nevertheless, a corrected emission spectrum is previously shown in Figure 5.12 (c), where no lasing at this wavelength is observed.

The integrated intensities are obtained for 909 nm microlaser (Laser A) and a

WGM luminescence peak (PL B) at 927 nm, which is highlighted in Figure 5.14. They are then plotted as a function of absorbed pump power as shown in Figure 5.15. For clarity, a zoom on PL B with a factor of 50 applied. Above a threshold in absorbed pump power, laser A signal increases linearly with the absorbed pump power, while PL B is saturated. This confirms the laser action from this microtoroid. By fitting the data with a linear function, the absorbed pump threshold value of about 210 nW is obtained, which is believed to be the lowest threshold ever recorded for any quasi-three-level laser.

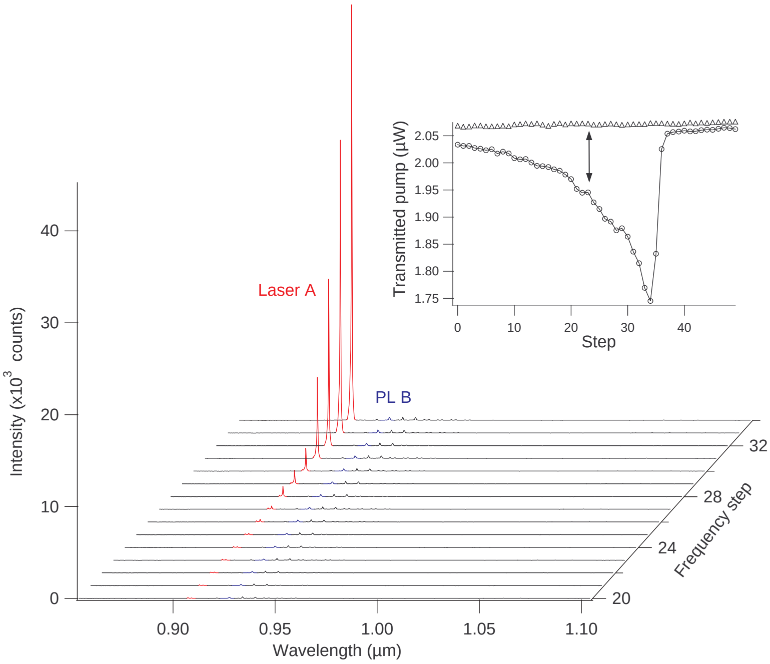

Figure 5.14: Emission spectra of the Nd^{3+} implanted microtoroid for different frequency steps (not corrected for CCD QE). Single mode laser action at 909 nm is observed. Inset: Fiber taper transmitted pump power with and without microtoroid at each frequency step, empty circles and empty triangles respectively. The dip corresponds to the absorbed pump power.

In conclusion, we have realized the fabrication of a neodymium implanted rolled-down microtoroid, by utilizing the wedge structure of silica microdisk. This permits a better control of active layer on the cavity's periphery, where the ultra-high Q fundamental modes locate. The quality factor of this cavity is measured as high as 4.2×10^7 at the wavelength of 776.01 nm. By exciting a WGM resonance at 803.41 nm that has a Q factor of 2.2×10^7, the emission properties of neodymium

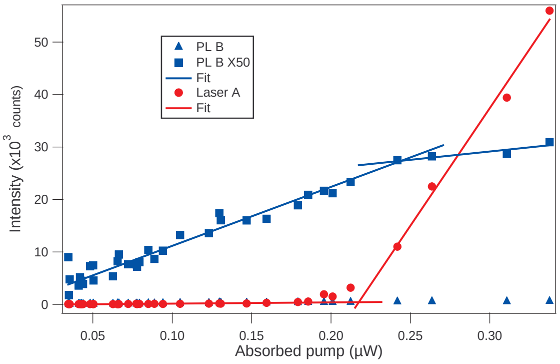

Figure 5.15: Integrated emission intensity around 909 nm and 927 nm, marked as red filled circles and blue triangles respectively. For clarity, a zoom of the PL signal with a factor of 50 is also presented by blue rectangles.

implanted microtoroid has been investigated. A single mode lasing at 909 nm is observed with an absorbed pump threshold of about 210 nW. This ultra-low threshold single-mode laser has potential applications in sensor applications and telecommunications (for erbium implanted micorotoids). One would like to improve this experiment and especially elucidate the origin of the unexpected poor emission at 1080 nm which is usually the preferred lasing wavelength.

Conclusion

In this thesis, surface tension induced whispering gallery mode microcavities, namely silica microspheres and on-chip microtoroids, have been investigated as platforms for rare earth based microlasers. They have been functionalized by using gadolinium oxide nanocrystals (Gd_2O_3), in which a significant fraction of gadolinium ions Gd^{3+} are substituted by optically active neodymium ions Nd^{3+}. The first evidence of lasing of this new material is our main result, all the greater because a new record value of the threshold power has been achieved.

The silica microspheres are produced by using CO_2 laser melting, an improved method, where bulk material is a regular optical fiber which is preliminarily elongated into a “microfiber”. Microspheres with a diameter ranging from 20 μm to 100 μm and Q-factors of 100 million are easily produced. For on-chip silica microtoroids, they are also obtained by CO_2 laser melting, but we use a preform which is a silica microdisk on silicon pedestal, produced in Grenoble by silicon microtechnology. This melting process, and the resulting toroid, are strongly dependant on the “undercut” (the difference in radii of the disk and the pedestal), the thickness of the disk and its shape. Therefore a very good control of the CO_2 beam waist and irradiation time is mandatory. Beside the normal rolled-up structure, a wedge-shaped preform leads to a rolled-down microtoroid. This structure presents a significant advantage to obtain a microlaser when the gain layer is on the top of the microdisk. These microcavities are efficiently excited by using home-made sub-wavelength tapered fibers.

WGMs of small mode volume have a decisive advantage for reducing the threshold of microlasers. In order to selectively excite these low order modes, we have developed a novel method to map the electromagnetic-field distributions directly using the taper-coupler as a near-field probe. This method relies on the very sensitive dependance of the coupling efficiency with respect to the taper location (height and distance). Then, the oscillations of the coupling efficiency when moving the taper provide a quick and easy way to ascertain the q orders and find the angular fundamental mode that possesses only one antinode close to the equator. This method has been successively applied to both silica microspheres and microtoroids. When starting from a microdisk with a diameter $D_0 \approx 80$ μm and thickness $e = 2.7$ μm, the obtained microtoroids have a diameter $D \sim 40$ nm and a minor diameter $d \sim 6$ μm. This large value of d does not lead to transversal single-mode cavities. However, by using our mapping method combined with an extensive laser spectroscopy, we have proven that a slight asymmetry of the microtoroid can help to reduce its density of modes without to significantly spoil the quality factor.

The functionalization of pure silica microspheres with Nd^{3+}:Gd_2O_3 nanocrystals consists of two steps : dip-coating at room temperature and annealing. The microsphere is first immersed for a few seconds in a colloidal suspension of nanocrystals in alcohol, which has been produced in Lyon. It is then slightly remelted by CO_2 laser for both annealing and embedding of the nanoemitters just below the sphere surface. It has been verified that the nanocrystals are not dissolved in silica. By this way the nanocrystals are buried in a place where they have maximal coupling with the low order WGMs of the microcavity. And these WGMs, at both the pump wavelength around 805 nm and emission wavelength around 1080 nm, keep their ultra-high Q-factor in the range of 10^8. This allows to use a very efficient "intracavity" pumping.

The above mentioned sensitivity to the coupling conditions makes the laser optimization rather difficult. We have therefore developed a method allowing a real-time measurement of the laser characteristic, hence an efficient optimization of its threshold and slope efficiency. This new method is based on the thermal bistability at the pump wavelength, which is very large thanks to the unprecedented Q-factor achieved for the pump. Its incoming power is kept constant, and its frequency is swept, either step-by-step, or by using an original "continuous scanning" at low frequency (up to 10 Hz). This frequency sweep changes the pump power injected in the cavity, which in turn changes the resonance frequency, thanks to the well known thermal bistability resulting from self heating. This mechanism provides a smooth and slow control of the injected power, allowing to monitor simultaneously the laser emission and the absorbed power on a digital oscilloscope. The validity of this method is demonstrated by comparing its results, for different scanning speeds, with those provided by the step-by-step technique.

When applied to microtoroids, the dip-coating method was not as successful as expected. Nevertheless, neodymium can be ion-implanted in the silica layer before its first processing. Starting from such a sample, where the neodymium ions were located at an average depths of 200 nm below the top of the 2.7 μm microdisk, a high-Q rolled-down microtoroid has been produced, on which we succeeded to observe $Nd^{3+}:SiO_2$ lasing at 903 nm, with a sub-microwatt threshold.

Finally, beside two new and useful experimental methods, three different low-threshold microlasers are demonstrated:

$Nd^{3+}:Gd_2O_3$ NCs based microsphere laser

The first laser based on lanthanide oxide nanocrystals is realized by pumping at $\lambda \sim 805$ nm. Moreover, a laser threshold as low as 40 nW is recorded from a 71 μm diameter sphere functionalized by $Nd^{3+}:Gd_2O_3$ NCs. To the best of our knowledge, this is the lowest threshold record for any rare earth based laser. By reducing the sphere diameter and increasing the nanoemitter concentration, single mode lasing at 1088 nm is also achieved from a 40 μm diameter sphere. The slope efficiency and threshold are measured as 7% and 65 nW. A thermal shift of the microlaser frequency due to absorbed pump power of -73 MHz/μW is measured by using a scanning F-P interferometer technique.

$Yb^{3+}:Gd_2O_3$ NCs based microsphere laser

The lasing on $Yb^{3+}:Gd_2O_3$ NCs is also achieved from a spherical cavity. Despite a pumping wavelength $\lambda \sim 800$ nm lying out of the high absorption band of Yb^{3+} ions, a threshold as low as 1.3 μW is observed; this value is believed to be the lowest value for any Yb based laser.

Nd implanted on-chip microtoroid laser

A rolled-down on-chip microtoroid is reported for the first time. On a neodymium ion-implanted microdisk, this structure enables to transfer the active layer to the microtoroid periphery, resulting in a better coupling to low order WGMs. This leads to a single-mode laser behavior at 909 nm with a threshold value of about 210 nW, that is also a lowest record for any quasi-three-level laser system.

The most promising feature of the reported microlaser is certainly the very low losses induced by the embedding of the nanocrystals, which validates the suitability of this doping method. With the ability to monitor which modes are involved in pumping and lasing, we achieve an unprecedented level of control. This opens the way for new results on further reduced thresholds, may be down to a still expected demonstration of thresholdless laser operation. The influence of the crystalline surrounding for the active ions requires also some deeper investigations which could be performed with core-shell lanthanide oxide nanocrystals, if they can be produced. In this context, an observable reduction of the inhomogeneous broadening of the emission lines would be very interesting for potential applications. Another attracting perspective would be to extend this work to other nanocrystalline emitters, like silicon nanocrystals which presently draw a strong interest in the solid state optics community.

Bibliography

[1] T. Maiman, “Stimulated optical radiation in ruby,” Nature **187**, 493– 494 (1960).

[2] R. N. Hall, G. E. Fenner, J. D. Kingsley, T. J. Soltys, and R. O. Carlson, “Coherent Light Emission From GaAs Junctions,” Phys. Rev. Lett. **9**(9), 366–368 (1962). URL `http://link.aps.org/doi/10.1103/PhysRevLett.9.366`.

[3] I. Protsenko, P. Domokos, V. Lefèvre-Seguin, J. Hare, J.-M. Raimond, and L. Davidovich, “Quantum Theory of a Thresholdless Laser,” Phys. Rev. A **59**, 1667–1682 (1999).

[4] A. Schawlow and C. Townes, “Infrared and optical masers,” Phys. Rev. **112**(6), 1940–1949 (1958).

[5] L. Rayleigh, *The Theory of Sound* (Dover (reprinted in 1945), 1877-1878).

[6] L. Rayleigh, “The Problem of the Whispering Gallery,” Phil. Mag. **20**, 1001 (1910).

[7] L. Lorenz, *Lysbevægelsen i og uden for en af plane Lysbølger belyst Kugle* (Luno, 1890).

[8] G. Mie, “Beitrage zur Optik trüber Medien, speziell kolloïdaler Metallosungen,” Ann. Phys. (Leipzig) **25**, 337–445 (1908).

[9] P. Debye, “Der lichtdruck auf kugeln von beliebigem material,” Annalen der physik **335**(11), 57–136 (1909).

[10] C. G. B. Garrett, W. Kaiser, and W. L. Bond, “Stimulated Emission Into Optical Whispering Modes of Spheres,” Phys. Rev. **124**, 1807–1809 (1961).

[11] A. Ashkin and J. M. Dziedzic, “Observation of optical resonances of dielectric spheres by light scattering,” Appl. Opt. **20**, 1803–1814 (1981).

[12] H.-M. Tzeng, K. F. Wall, M. B. Long, and R. K. Chang, “Laser emission from individual droplets at wavelength corresponding to morphology dependent resonances,” Opt. Lett. **9**, 499–501 (1984).

[13] V. B. Braginsky, M. L. Gorodetsky, and V. S. Ilchenko, “Quality-factor and non-linear properties of optical whispering-gallery modes,” Phys. Lett. A **137**, 393–397 (1989). URL `http://dx.doi.org/10.1016/0375-9601(89)90912-2`.

[14] L. Collot, V. Lefèvre-Seguin, M. Brune, J. M. Raimond, and S. Haroche, “Very High-Q Whispering-Gallery Mode Resonances Observed on Fused Silica Microspheres,” Europhys. Lett. **23**(5), 327–334 (1993). URL `http://stacks.iop.org/0295-5075/23/327`.

[15] V. Sandoghdar, F. Treussart, J. Hare, V. Lefèvre-Seguin, J.-M. Raimond, and S. Haroche, “Very low threshold whispering-gallery mode microsphere laser,” Phys. Rev. A **54**, R1777 (1996). URL `http://link.aps.org/abstract/PRA/v54/pR1777`.

[16] D. K. Armani, T. J. Kippenberg, S. M. Spillane, and K. J. Vahala, “Ultra-High-Q Toroid Microcavity on a Chip,” Nature **421**, 925–928 (2003). URL `http://dx.doi.org/10.1038/nature01371`.

[17] P. K. Tien, R. Ulrich, and R. J. Martin, “Modes of propagating light waves in thin deposited semiconductor films,” Appl. Phys. Lett. **14**(9), 291–294 (1969). URL `http://link.aip.org/link/?APL/14/291/1`.

[18] S. Schiller and R. L. Byer, “High-resolution spectroscopy of whispering gallery modes in large dielectric spheres,” Opt. Lett. **16**, 1138–1140 (1991).

[19] S. Steiner, J. Hare, V. Lefèvre-Seguin, and J.-M. Gérard, “Room Temperature Lasing of InAs/GaAs Quantum Dots in the Whispering Gallery Modes of a Silica Microsphere,” Opt. Express **15**, 10,053–10,060 (2007). URL `http://www.opticsinfobase.org/abstract.cfm?URI=oe-15-16-10052`.

[20] M. L. Gorodetsky and V. S. Ilchenko, “Optical Microsphere Resonators: Optimal Coupling to High-Q Whispering-Gallery Modes,” J. Opt.Soc. Am. B **16**, 147–154 (1999). URL `http://www.opticsinfobase.org/abstract.cfm?URI=josab-16-1-147`.

[21] V. V. Vassiliev, V. L. Velichansky, V. S. Ilchenk, M. Gorodetsky, L. Hollberg, and A. V. Yarovitsky, “Narrow-Line-Width Diode Laser with a High-Q Microsphere Resonator,” Opt. Commun. **158**, 305–312 (1998).

[22] J.-P. Laine, B. E. Little, D. R. Lim, H. C. Tapalian, L. C. Kimerling, and H. A. Haus, “Planar Integrated Wavelength-Drop Device Based on Pedestal Antiresonant Reflecting Waveguides and High-Q Silica Microspheres,” Opt. Lett. **25**, 1636 (2000).

[23] N. Dubreuil, J. C. Knight, D. K. Leventhal, V. Sandoghdar, J. Hare, and V. Lefèvre, “Eroded monomode optical fiber for excitation in fused-silica microspheres,” Opt. Lett. **20**, 813 (1995).

[24] G. A. Serpengüzel, S. Arnold, and G. Griffel, “Excitation of Resonances of Microspheres on an Optical Fiber,” Opt. Lett. **20**, 654 (1995).

[25] G. Griffel, S. Arnold, D. Taskent, A. Serpenguzel, J. Connolly, and N. Morris, “Morphology-Dependent Resonances of a Microsphere-Optical Fiber System,” Opt. Lett. **21**, 695 (1996).

[26] V. S. Ilchenko, X. S. Yao, and L. Maleki, “Pigtailing the High-Q Microsphere Cavity: A Simple Fiber Coupler for Optical Whispering-Gallery Modes,” Opt. Lett. **24**, 723 (1999).

[27] J. C. Knight, G. Cheung, F. Jacques, and T. A. Birks, “Phase-matched excitation of whispering-gallery-mode resonances by a fiber taper,” Opt. Lett. **22**(15), 1129–1131 (1997). URL `http://www.opticsinfobase.org/abstract.cfm?&uri=ol-22-15-1129`.

[28] M. Cai, O. Painter, K. J. Vahala, and P. C. Sercel, “Fiber-Coupled Microsphere Laser,” Opt. Lett. **25**, 1430 (2000).

[29] S. M. Spillane, T. J. Kippenberg, O. J. Painter, and K. J. Vahala, “Ideality in a fiber-taper-coupled microresonator system for application to cavity quantum electrodynamics,” Phys. Rev. Lett. **91**(4), 043,902 (2003).

[30] S. Shopova, G. Farca, A. Rosenberger, W. Wickramanayake, and N. Kotov, “Microsphere whispering-gallery-mode laser using HgTe quantum dots,” Appl. Phys. Lett. **85**, 6101 (2004).

[31] W. von Klitzing, E. Jahier, R. Long, F. Lissillour, V. Lefèvre-Seguin, J. Hare, J.-M. Raimond, and S. Haroche, "Very Low Threshold Lasing in Er^{3+} Doped ZBLAN Microsphere," Electron. Lett. **35**(20), 1745–1746 (1999).

[32] B. Min, T. J. Kippenberg, L. Yang, K. J. Vahala, J. Kalkman, and A. Polman, "Erbium-implanted high- Q silica toroidal microcavity laser on a silicon chip," Phys. Rev. A **70**(3), 033,803 (2004). URL `http://link.aps.org/abstract/PRA/v70/e033803`.

[33] J. Kalkman, A. Tchebotareva, A. Polman, T. J. Kippenberg, B. Min, and K. J. Vahala, "Fabrication and characterization of erbium-doped toroidal microcavity lasers," J. Appl. Phys. **99**(8), 083103 (pages 9) (2006). URL `http://link.aip.org/link/?JAP/99/083103/1`.

[34] F. Orucevic, J. Hare, and V. Lefèvre-Seguin, "Neodymium photoluminescence in whispering gallery modes of toroidal microcavities," Proc SPIE, Optoelectronic Devices: Physics, Fabrication, and Application III. Edited by Piprek, Joachim; Wang, Jian Jim. (2006).

[35] L. Yang and K. Vahala, "Gain functionalization of silica microresonators," Opt. Lett. **28**(8), 592–594 (2003).

[36] R. Bazzi, A. Brenier, P. Perriat, and O. Tillement, "Optical properties of neodymium oxides at the nanometer scale," J. Lumin. **113**(1-2), 161–167 (2005).

[37] A. Brenier and G. Boulon, "Laser heated pedestal growth and spectroscopic investigations of Nd^{3+}-doped Gd_2O_3 single crystal fibres," J. Lumin. **82**(4), 285–289 (1999).

[38] F.-M. Treussart, "Étude expérimentale de l'effet Laser dans des microsphères de silice dopées avec des ions néodyme," Ph.D. thesis, Université Pierre et Marie Curie – Paris VI (1997).

[39] C. C. Lam, P. T. Leung, and K. Young, "Explicit asymptotic formulas for the positions, widths, and strengths of resonances in Mie scattering," J. Opt.Soc. Am. B **9**, 1585–1592 (1992).

[40] H. M. Lai, P. T. Leung, K. Young, P. W. Barber, and S. C. Hill, "Time independant perturbation for leaking electromagnetic modes in open systems

with application to resonances in microdroplets," Phys. Rev. A **41**, 5187–5198 (1990).

[41] H. Nussenzveig, *Diffraction Effects in Semiclassical Scattering* (Cambridge University Press, 1992).

[42] J. Laine, C. Tapalian, B. Little, and H. Haus, "Acceleration sensor based on high-Q optical microsphere resonator and pedestal antiresonant reflecting waveguide coupler," Sens. Actuators, A **93**(1), 1–7 (2001).

[43] N. Hanumegowda, C. Stica, B. Patel, I. White, and X. Fan, "Refractometric sensors based on microsphere resonators," Appl. Phys. Lett. **87**, 201,107 (2005).

[44] F. Vollmer, D. Braun, A. Libchaber, M. Khoshsima, I. Teraoka, and S. Arnold, "Protein Detection by Optical Shift of a Resonant Microcavity," Appl. Phys. Lett. **80**, 4057–4059 (2002).

[45] F. Vollmer and S. Arnold, "Whispering-gallery-mode biosensing: label-free detection down to single molecules," Nat. Methods **5**(7), 591–596 (2008).

[46] F. Lissillour, D. Messager, G. Stéphan, and P. Féron, "Whispering-Gallery-Mode Laser at 1.56μm Excited by a Fiber Taper," Opt. Lett. **26**, 1051–1053 (2001).

[47] X. Peng, F. Song, S. Jiang, N. Peyghambarian, M. Kuwata-Gonokami, and L. Xu, "Fiber-taper-coupled L-band Er-doped tellurite glass microsphere laser," Appl. Phys. Lett. **82**, 1497 (2003).

[48] D. S. Weiss, V. Sandoghdar, J. Hare, V. Lefévre-Seguin, J.-M. Raimond, and S. Haroche, "Splitting of High-Q Mie Modes Induced by Light Backscattering in Silica Microspheres," Opt. Lett. **20**, 1835–1837 (1995).

[49] M. L. Gorodetsky, A. D. Pryamikov, and V. S. Ilchenko, "Rayleigh Scattering in High-Q Microspheres," J. Opt.Soc. Am. B **17**, 1051–1057 (2000).

[50] S. Steiner, "Microsphères de silice et Boîtes quantiques InAs/GaAs: réalisation d'un microlaser à faible seuil," Ph.D. thesis, Université Pierre et Marie Curie – Paris VI (2003).

[51] M. L. Gorodetsky, A. A. Savchenkov, and V. S. Ilchenko, "Ultimate Q of optical microsphere resonators," Opt. Lett. **21**, 453–455 (1996).

[52] A. Taflove, S. Hagness, *et al.*, *Computational electrodynamics: the finite-difference time-domain method* (Artech House Norwood, MA, 1995).

[53] F. Assous, P. Degond, E. Heintze, P. Raviart, and J. Segre, “On a finite-element method for solving the three-dimensional Maxwell equations,” J. Comput. Phys. **109**(2), 222–237 (1993).

[54] T. J. Kippenberg, S. M. Spillane, and K. J. Vahala, “Demonstration of Ultra-High-Q Small Mode Volume Toroid Microcavities on a Chip,” Appl. Phys. Lett. **85**, 6113–6115 (2004).

[55] M. Oxborrow, “Traceable 2-D finite-element simulation of the whispering-gallery modes of axisymmetric electromagnetic resonators,” IEEE Trans. Microwave Theory Tech. **55**(6), 1209 (2007).

[56] J. Laine, B. Little, and H. Haus, “Etch-eroded fiber coupler for whispering-gallery-mode excitation in high-Q silica microspheres,” IEEE Photon. Technol. Lett. **11**(11), 1429–1430 (1999).

[57] S. Self, “Focusing of spherical Gaussian beams,” Appl. Opt. **22**(5), 658–661 (1983).

[58] A. D. McLachlan and F. P. Meyer, “Temperature dependence of the extinction coefficient of fused silica for CO_2 laser wavelengths,” Appl. Opt. **26**(9), 1728–1731 (1987). URL `http/ao.osa.org/abstract.cfm?URI=ao-26-9-1728`.

[59] K. Srinivasan, M. Borselli, O. Painter, A. Stintz, and S. Krishna, “Cavity Q, mode volume, and lasing threshold in small diameter AlGaAs microdisks with embedded quantum dots,” Phys. Rev. Lett. **86**, 1502–1505 (2001).

[60] P. Barclay, K. Srinivasan, and O. Painter, “Nonlinear response of silicon photonic crystal microresonators excited via an integrated waveguide and fiber taper,” Phys. Rev. E **68**, 046,606 (2003).

[61] Z. Hale, F. Payne, R. Marks, C. Lowe, and M. Levine, “The single mode tapered optical fibre loop immunosensor,” Biosens. Bioelectron. **11**(1-2), 137–148 (1996). URL `http://linkinghub.elsevier.com/retrieve/pii/0956566396837213`.

[62] T. A. Birks, W. J. Wadsworth, and P. S. Russell, “Supercontinuum generation in tapered fibers,” Opt. Lett. **25**, 1415–1417 (2000).

[63] G. Brambilla, G. Murugan, J. Wilkinson, and D. Richardson, “Optical manipulation of microspheres along a subwavelength optical wire,” Opt. Lett. **32**(20), 3041–3043 (2007).

[64] F. Le Kien, V. Balykin, and K. Hakuta, “Atom trap and waveguide using a two-color evanescent light field around a subwavelength-diameter optical fiber,” Phys. Rev. A **70**(6), 63,403 (2004).

[65] F. Orucevic, V. Lefèvre-Seguin, and J. Hare, “Transmittance and Near-Field Characterization of Sub-Wavelength Tapered Optical Fibers,” Opt. Express **15**, 13,624–13,629 (2007). URL `http://www.opticsinfobase.org/abstract.cfm?URI=oe-15-21-13624`.

[66] F. Bayle and J. P. Meunier, “Efficient fabrication of fused-fiber biconical taper structures by a scanned CO_2 laser beam technique,” Appl. Opt. **44**, 6402–6411 (2005).

[67] Y. Takeuchi, M. Hirayama, S. Sumida, and O. Kobayashi, “Characteristics of ceramic microheater for fiber coupler fabrication,” Jpn. J. Appl. Phys. **37**, 3665–3668 (1998).

[68] L. Ding, C. Belacel, S. Ducci, G. Leo, and I. Favero, “Ultra-low loss single-mode silica tapers manufactured by a microheater,” Arxiv preprint arXiv:1001.3076 (2010).

[69] T. A. Birks and Y. W. Li, “The Shape of Fiber Tapers,” J. Lightwave Technol. **10**, 432–438 (1992).

[70] R. Altes, “Detection, estimation, and classification with spectrograms,” The Journal of the Acoustical Society of America **67**, 1232 (1980).

[71] D. R. Rowland and J. Love, “Evanescent Wave Coupling of Whispering Gallery Modes of a Dielectric Cylinder,” IEE Proceedings-J **140**, 177–188 (1993).

[72] S. Schiller, I. I. Yu, M. M. Fejer, and R. L. Byer, “Fused-silica monolithic total-internal-reflection resonator,” Opt. Lett. **17**, 378–380 (1992).

[73] M. Cai and K. J. Vahala, “Highly Efficient Optical Power Transfer to Whispering-Gallery Modes by Use of a Symmetrical Dual-Coupling Configuration,” Opt. Lett. **25**, 260 (2000).

[74] T. Kippenberg, S. Spillane, and K. Vahala, “Modal coupling in traveling-wave resonators,” Opt. Lett. **27**(19), 1669–1671 (2002). URL `http://www.opticsinfobase.org/abstract.cfm?URI=ol-27-19-1669`.

[75] A. Mazzei, S. Götzinger, L. de S. Menezes, G. Zumofen, O. Benson, and V. Sandoghdar, “Controlled coupling of counterpropagating whispering-gallery modes by a single Rayleigh scatterer: a classical problem in a quantum optical light,” Phys. Rev. Lett. **99**(17), 173,603 (2007).

[76] J. Zhu, S. Ozdemir, Y. Xiao, L. Li, L. He, D. Chen, and L. Yang, “On-chip single nanoparticle detection and sizing by mode splitting in an ultrahigh-Q microresonator,” Nat. Photonics **4**(1), 46–49 (2009).

[77] M. L. Gorodetsky and V. S. Ilchenko, “High-Q optical whispering-gallery microresonators: precession approach for spherical mode analysis and emission patterns with prisms couplers,” Opt. Commun. **113**, 133–143 (1994).

[78] J. Knight, N. Dubreuil, V. Sandoghdar, V. Lefèvre-Seguin, J.-M. Raimond, and S. Haroche, “Coupleur optique à bande étroite utilisant l’excitation des modes de galerie d’un élément résonateur diélectrique de forme de révolution,” Tech. Rep. n 95 11624, Brevet de France-Télécom (1995).

[79] S. Götzinger, S. Demmerer, O. Benson, and V. Sandoghdar, “Mapping and manipulating whispering gallery modes of a microsphere resonator with a near-field probe,” J. Microsc. **202**(1), 117 (2001).

[80] C. Dong, Y. Xiao, Y. Yang, Z. Han, G. Guo, and L. Yang, “Directly mapping whispering gallery modes in a microsphere through modal coupling and directional emission,” Chin. Opt. Lett. **6**(4), 300–302 (2008).

[81] A. Savchenkov, A. Matsko, D. Strekalov, V. Ilchenko, and L. Maleki, “Mode filtering in optical whispering gallery resonators,” Electron. Lett. **41**(8), 495–497 (2005). URL `http://horology.jpl.nasa.gov/quantum/pub/Mode_damper.pdf`.

[82] F. Orucevic, F. Guattari, J. Hare, V. Lefèvre-Seguin, J. Verbert, E. Hadji, and J.-M. Gérard, “Neodymium photoluminescence in Whispering Gallery Modes of toroidal microcavities,” J. Phys. IV France **135**, 245–246 (2006).

[83] S. L. McCall, A. F. J. Levi, R. E. Slusher, S. J. Pearton, , and R. A. Logan, "Whispering-Gallery Mode Microdisk Lasers," Appl. Phys. Lett. **60**, 289–291 (1992).

[84] P. Michler, A. Kiraz, L. Zhang, C. Becher, E. Hu, and A. Imamoglu, "Laser emission from quantum dots in microdisk structures," Appl. Phys. Lett. **77**, 184 (2000).

[85] L. Liu, R. Kumar, K. Huybrechts, T. Spuesens, G. Roelkens, E. Geluk, T. De Vries, P. Regreny, D. Van Thourhout, R. Baets, *et al.*, "An ultra-small, low-power, all-optical flip-flop memory on a silicon chip," Nat. Photonics **4**(3), 182–187 (2010).

[86] T. Kippenberg, J. Kalkman, A. Polman, and K. Vahala, "Demonstration of an erbium-doped microdisk laser on a silicon chip," Phys. Rev. A **74**(5), 51,802 (2006).

[87] I. Grudinin, N. Yu, and L. Maleki, "Generation of optical frequency combs with a CaF_2 resonator," Opt. Lett. **34**(7), 878–880 (2009).

[88] F. Treussart, V. S. Ilchenko, J-F.Roch, J. Hare, V. Lefèvre-Seguin, J.-M. Raimond, and S. Haroche, "Evidence for Intrinsic Kerr Bistability of High-Q Microsphere Resonators in Superfluid Helium," Eur. Phys. J. D **1**, 235–238 (1998).

[89] V. S. Ilchenko and M. L. Gorodetsky, "Thermal nonlinear effects in optical whispering gallery microresonators," Laser Phys. **2**, 1004–1009 (1992).

[90] T. Carmon, L. Yang, and K. Vahala, "Dynamical thermal behavior and thermal self-stability of microcavities," Opt. Express **12**(20), 4742–4750 (2004).

[91] H. Rokhsari, S. Spillane, and K. Vahala, "Loss characterization in microcavities using the thermal bistability effect," Appl. Phys. Lett. **85**, 3029 (2004).

[92] R. Zhang, S. Seo, A. Milenin, M. Zacharias, and U. G
"osele, "Visible range whispering-gallery mode in microdisk array based on size-controlled Si nanocrystals," Appl. Phys. Lett. **88**, 153,120 (2006).

[93] J. Verbert, F. Mazen, T. Charvolin, E. Picard, V. Calvo, P. Noé, J. Gérard, E. Hadji, F. Orucevic, J. Hare, and V. Lefèvre-Seguin, "Room Temperature Emission from Er-Doped Silicon-Rich Oxide Microtorus," Eur. Phys.J. Appl. Phys **34**, 81–84 (2006). URL `http://dx.doi.org/10.1051/epjap:2006048`.

[94] X. Fan, P. Palinginis, S. Lacey, H. Wang, and M. Lonergan, "Coupling semiconductor nanocrystals to a fused-silica microsphere: a quantum-dot microcavity with extremely high Q factors," Opt. Lett. **25**(21), 1600–1602 (2000).

[95] Y. Park, A. Cook, and H. Wang, "Cavity QED with diamond nanocrystals and silica microspheres," Nano Lett. **6**(9), 2075–2079 (2006).

[96] G. West and N. Clements, "A comparison of the Eu3+ temperature dependent emission lifetimes in Sc2O3, Y2O3 and Gd2O3 host crystals," J. Lumin. **54**(4), 245–248 (1992).

[97] W. Zhang, Y. Zhang, J. Tang, Y. Zhang, L. Wang, and Q. Ling, "Study on preparation and optic properties of nano europium oxide–ethanol sol by pulsed laser ablation," Thin Solid Films **417**(1-2), 43–46 (2002).

[98] E. Goldburt, B. Kulkarni, R. Bhargava, J. Taylor, and M. Libera, "Size dependent efficiency in Tb doped Y2O3 nanocrystalline phosphor," J. Lumin. **72**, 190–192 (1997).

[99] R. Bazzi, M. Flores-Gonzalez, C. Louis, K. Lebbou, C. Dujardin, A. Brenier, W. Zhang, O. Tillement, E. Bernstein, and P. Perriat, "Synthesis and luminescent properties of sub-5-nm lanthanide oxides nanoparticles," J. Lumin. **102**, 445–450 (2003).

[100] R. Bazzi, M. Flores, C. Louis, K. Lebbou, W. Zhang, C. Dujardin, S. Roux, B. Mercier, G. Ledoux, E. Bernstein, *et al.*, "Synthesis and properties of europium-based phosphors on the nanometer scale: Eu2O3, Gd2O3: Eu, and Y2O3: Eu," J. Colloid Interface Sci. **273**(1), 191–197 (2004).

[101] M. Nichkova, D. Dosev, S. Gee, B. Hammock, and I. Kennedy, "Microarray immunoassay for phenoxybenzoic acid using polymer encapsulated Eu: Gd_2O_3 nanoparticles as fluorescent labels," Anal. Chem **77**(21), 6864–6873 (2005). URL `http://pubs.acs.org/doi/abs/10.1021/ac050826p`.

[102] S. Wang, Y. Zhou, Y. Lam, C. Kam, Y. Chan, and X. Yao, "Fabrication and characterisation of neodymium-doped silica glass by sol-gel process," Mater. Res. Innovations **1**(2), 92–96 (1997).

[103] Z. Cai, H. Xu, G. Stéphan, P. Féron, and M. Mortier, "Red-shift in Er: ZBLALiP whispering gallery mode laser," Opt. Commun. **229**(1-6), 311–315 (2004).

[104] E. Ostby, L. Yang, and K. Vahala, “Ultralow-threshold Ybˆ 3+: SiO_2 glass laser fabricated by the solgel process,” Opt. Lett. **32**(18), 2650–2652 (2007).

[105] E. Ostby and K. Vahala, “Yb-doped glass microcavity laser operation in water,” Opt. Lett. **34**(8), 1153–1155 (2009).

[106] D. Armani, B. Min, A. Martin, and K. Vahala, “Electrical thermo-optic tuning of ultrahigh-Q microtoroid resonators,” Appl. Phys. Lett. **85**, 5439 (2004).

[107] T. Aoki, B. Dayan, E. Wilcut, W. P. Bowen, A. S. Parkins, T. J. Kippenberg, K. J. Vahala, and H. J. Kimble, “Observation of strong coupling between one atom and a monolithic microresonator,” Nature **443**(7112), 671–674 (2006). URL `http://www.nature.com/nature/journal/v443/n7112/abs/nature05147.html`.

[108] T. Kippenberg and K. Vahala, “Cavity optomechanics: back-action at the mesoscale,” Science **321**(5893), 1172 (2008).

[109] L. Yang, D. K. Armani, and K. J. Vahala, “Fiber-Coupled Erbium Microlasers on a Chip,” Appl. Phys. Lett. **83**, 825–827 (2003).

[110] B. Min, S. Kim, K. Okamoto, L. Yang, A. Scherer, H. Atwater, and K. Vahala, “Ultralow threshold on-chip microcavity nanocrystal quantum dot lasers,” Appl. Phys. Lett. **89**, 191,124 (2006).

[111] I. S. Grudinin, H. Lee, O. Painter, and K. J. Vahala, “Phonon Laser Action in a Tunable Two-Level System,” Phys. Rev. Lett. **104**(8), 083,901 (2010).

Fabrication et caractérisation de microcavités fonctionnalisées par des nanocristaux d'oxydes de terres rares : réalisation d'un microlaser monomode à très bas seuil

Les cavités de silice, comme les microsphères ou les microtores intégrés sur puce, définissent des modes de galerie, de facteur de qualité extrêmement élevé et de faible volume modal. Elles ont suscité un fort intérêt depuis deux décennies et trouvent des applications pour la QED en cavité, les microlasers, ou les senseurs de biomolécules. Cette thèse décrit la réalisation d'un microlaser à seuil ultra-bas fondé sur des nanocristaux de Nd^{3+}:Gd_2O_3 (NCs), qui sont incorporés à la surface de la cavité. Nous démontrons une nouvelle méthode de cartographie de la distribution du champ électromagnétique, fondée sur le coupleur à fibre étirée (taper) utilisé pour l'excitation en onde évanescente. Cela fournit un moyen commode pour localiser et exciter sélectivement des modes de faible volume. De plus, nous démontrons une technique de mesure en temps réel de la caractéristique laser, qui utilise la bistabilité thermique des microcavités et permet une optimisation rapide et efficace des conditions de couplage taper-cavité.

Un fonctionnement laser monomode à 1088 nm est obtenu pour une microsphere de 40 μm de diamètre, comprenant des Nd^{3+}:Gd_2O_3 NCs pompés à 802 nm, avec un seuil de 65 nW. Le plus bas seuil observé, de 40 nW, est à notre connaissance le seuil le plus faible jamais obtenu pour des terres rares. Le facteur de qualité de ces cavités actives atteint 10^8 à la longueur d'onde d'émission, favorisant l'obtention un microlaser dont le spectre est extrêmement fin. Enfin, sur un microtore formé de silice dopée par implantation ionique, nous avons obtenu un laser monomode à 909 nm avec un seuil de 210 nW.

Mots clés : modes de galerie ; nanocristaux ; microcavité; laser; néodyme; champ proche ; fibre optique

Fabrication and characterization of optical microcavities functionalized by rare-earth oxide nanocrystals: realization of a single-mode ultra low threshold laser

Fused silica microspheres and on-chip silica microtoroids support ultra-high quality factor and small volume whispering-gallery-modes (WGMs). They have attracted great interest for several decades and have had various applications like cavity-QED, microlasers, and biosensing. This thesis focuses on the realization of ultra-low threshold microlaser based on Nd^{3+}:Gd_2O_3 nanocrystals (NCs), which are embedded close to the cavity surface. In particular, we demonstrate a novel method for the mapping of the electromagnetic-field distribution of WGMs using the fiber taper coupler used for evanescent-wave coupling. This provides an efficient way to locate and selectively excite the small volume modes.

Moreover, we demonstrate a real time measurement technique of the laser characteristic, which uses thermal bistability of such microcavities, and enables quick and efficient optimization of the taper-cavity coupling conditions.

Finally, single mode lasing at 1088 nm is achieved from a 40 μm diameter microsphere with Nd^{3+}:Gd_2O_3 NCs, optically pumped at 802 nm, with a threshold of 65 nW. The lowest measured threshold is 40 nW, which is believed to be the lowest threshold record for any rare earth lasers. The Q factor of these active cavities at emission wavelength is as high as 10^8, favourable for ultra narrow linewidth spectrum. In addition, for an on-chip silica microtoroid made from Nd ion-implanted silica, we have achieved single-mode lasing at 909 nm and a threshold of 210 nW.

Keywords: whispering gallery; nanocrystals; microcavity; laser; neodymium; near field; optical fiber.